2D EXPERIMENTAL AND NUMERICAL INVESTIGATION ON THE EFFECT OF A FOWLER FLAP GAP AND OVERLAP SIZE ON THE FLOW FIELD

INVESTIGATION EXPÉRIMENTALE ET NUMÉRIQUE EN 2D SUR L'EFFET DE LA TAILLE DE BÂILLEMENT ET DE RECOUVREMENT D'UN VOLET "FOWLER" SUR L'ÉCOULEMENT

A Thesis Submitted

to the Division of Graduate Studies of the Royal Military College of Canada

by

David Demel, B.Eng.
2Lt

In Partial Fulfillment of the Requirements for the Degree of

Master of Applied Science in Aeronautical Engineering - Aerodynamics

April, 2014

To my wife Maria Fe and my son Ethan, without their endless support, patience and self-sacrifice this work would not have been possible.

Acknowledgments

The present work was possible thanks to a multitude of people. First and foremost, the author would like to acknowledge the patient support, guidance and tutelage of Dr. Mohsen Ferchichi and Dr. Maj. Sylvain Graveline of the Royal Military College of Canada (RMCC), who acted as thesis co-supervisors.

Next, the author would also like to recognize Dr. Hachimi Fellouah and Dr. Martin Brouillette of Université de Sherbrooke for their generosity in providing access to the Sherbrooke University wind tunnel and the 2D PIV system, Dr. Callum Gray of LaVision for his time and instruction in the art of PIV experimental methods, Dr. Asad Asghar of RMCC for his assistance with the Scanivalve, the RMCC Department of Mechanical and Aerospace Engineering machine shop for their superior craftsmanship and expertise, and Mr. Marouen Dghim of RMCC for his dedication and assistance with both experimental campaigns.

Finally, the author would like to thank Capt. Greg Givogue of the Directorate of Technical Airworthiness and Engineering Support and Mr. Chris Bowers of the CP140/A Weapons System Manager for their financial support of this project.

Abstract

Demel, David. M.A.Sc. Royal Military College of Canada, April, 2014. *2D Experimental and Numerical Investigation on the Effect of a Fowler Flap Gap and Overlap Size on the Flow Field.* Supervised by Dr. Mohsen Ferchichi and Dr Sylvain Graveline.

The CP-140 Aurora aircraft was purchased by the Royal Canadian Air Force in the early 1980s as a maritime patrol and anti-submarine warfare platform. Over the years, the flaps of these aircraft have been found misaligned beyond the manufacturer specified limits. With little information available detailing the reasons for the current limits, a project was initiated to evaluate the aerodynamic implications of this flap misalignment. Determining the performance of high lift devices is an essential part of aircraft design and maintenance. In spite of decades of research, a comprehensive understanding of this complex flow field continues to elude the aeronautical community. In an effort to improve the understanding of the aerodynamic performance of high lift devices, the following work details an experimental and numerical investigation of a two dimensional flow over a wing equipped with a Fowler flap. A cross section of the CP-140 Aurora wing was investigated at various angles of attack in the clean configuration (flap stowed), landing configuration (flap deployed and deflected to 40°), and the effect of the variation of the flap gap and overlap was studied. This research included both experimental work using a Particle Image Velocimetry (PIV) system, and numerical simulations using Reynolds Averaged Navier Stokes (RANS) method.

The flow over the flap was found to be massively separated for all the landing configurations investigated. The focus of the investigation was on the boundary layer (BL) on the wing trailing edge (TE) immediately upstream of the flap slot. It was found that while an increase in flap gap benefited the BL on the wing TE by affecting a fuller velocity profile, a corresponding increase in flap overlap had a detrimental effect on the wing TE BL, that eventually induced a separation bubble.

The accuracy of the separation location prediction of the clean configuration simulations was within 5% of the experimental findings at angles of attack below 10°. However, the accuracy of the simulations quickly dwindled as the region of flow separation grew with larger angles of attack. The simulation of the landing configurations without 'a priori' knowledge was not accurately resolved by the CFD in spite of the application of best practices cited in literature. The major failure of the landing configuration simulations was in the prediction of the velocity magnitude of the flow emanating from the flap slot; the velocity magnitude was overestimated by a factor of two. Employing the 'a priori' knowledge obtained from the wind tunnel data, the landing configuration simulations were then adjusted to correct the slot flow. Consequently, the flow development depicted in the 'a priori' simulations was in agreement with the experiment.

Keywords: Fowler flap, high lift devices, boundary layer, Computational Fluid Dynamics, RANS, Wind tunnel test, PIV, Fluid Dynamics, Aerospace Engineering

Résumé

Demel, David. M.Sc.A. Collège militaire royal du Canada, Avril, 2014. *Investigation expérimentale et numérique en 2D sur l'effet de la taille de bâillement et de recouvrement d'un volet "Fowler" sur l'écoulement.* Thèse dirigée par M. Mohsen Ferchichi, Ph.D. and M. Sylvain Graveline, Ph.D.

Le CP-140 Aurora acquis par l'aviation royale canadienne au début des années 1980 est utilise pour des patrouilles maritimes et des tâches de guerre anti-sous-marine. Au fil des ans, les volets de ces avions ont été trouvés mal alignés et au-delà des limites spécifiées par le fabricant. En l'absence d'information disponible détaillant les raisons des limites actuelles, un projet a été mis entamé afin d'évaluer les conséquences aérodynamiques de cette condition. Les performances des dispositifs hypersustentateurs sont essentielles pour la conception et l'entretien des aéronefs. En dépit de décennies de recherche, une compréhension complète de ce cas complexe continue à échapper à la communauté aéronautique. Cette thèse détaille une étude expérimentale et numérique d'un écoulement bi-dimensionnel sur une aile de CP-140 Aurora équipée d'un volet "Fowler". Cette section transversale de l'aile a été étudiée à différents angles d'incidence dans la configuration lisse (sous volet rétracté), configuration d'atterrissage (volet déployé et ajusté à 40°), et l'effet de plusieurs bailles de bâillement et de recouvrement. Cette étude comprend une partie expérimental, utilisant un système de Vélocimétrie par Images de Particules (PIV), et une partie numérique, utilisant des simulations employant des méthodes de "RANS".

L'écoulement sur le volet a était massivement séparé pour toutes les cas avec volet déployé. Cette recherche met l'accent sur la couche limite au bord de fuite d'aile, immédiatement en amont du bâillement du volet. Il fut constaté qu'une augmentation du bâillement bénéficie la couche limite sur le bord de fuite d'aile qui présente un profil de vitesse moins écarté du mur. Une augmentation correspondante du recouvrement d'un volet a eu un effet néfaste sur la couche limite, et a finalement provoqué une séparation.

La validité d'estimation de décollement de l'écoulement des simulations en configuration lisse fut estimé à 5% pour des incidences en dessous de 10°. La validité des simulations a diminué rapidement quand l'incidence augmente au delà de cette valeur, probablement à cause de l'influence grandissante de la région de séparation en couru. Les simulations des configurations d'atterrissage 'a priori' n'ont pas été résolues avec précision par la CFD, et ce, malgré l'utilisation de meilleures pratiques disponibles. La source principale d'erreur des simulations en configuration d'atterrissage provient des lacunes aux environs du bâillement. La magnitude de la vitesse a été surestimée par un facteur de deux. Après les essais en soufflerie, les simulations de configuration d'atterrissage ont ensuite été ajustées pour ajuster l'écoulement issu du bâillement du volet, résultant ainsi à une meilleur accord entre les simulations et les essais en soufflerie.

Mots clés : volet "Fowler", hypersustentateur, couche limite, modélisation numérique et dynamique des fluides, moyenne de Reynolds, essai en soufflerie, PIV, dynamique des fluides, aérospatiale

Table of Contents

List of Tables

List of Figures

Nomenclature

α	Angle of attack	deg
$\delta\overline{V}$	$V_{jetmax} - V_{merger}$	m/s
δ	Boundary layer thickness	m
δ^*	Boundary layer displacement thickness	m
δ_{flap}	Flap deflection angle	deg
κ	von Kármán constant $\kappa = 0.41$	-
λ	Wing taper ratio	-
ω	Mean spanwise vorticity	$1/s$
$\overline{uu}$	Streamwise Reynolds stress	m^2/s^2
$\overline{vv}$	Transverse Reynolds stress	m^2/s^2
$\overline{V}$	Velocity vector	m/s
$\overline{ww}$	Lateral Reynolds stress	m^2/s^2
ρ	Density	kg/m^3
θ	Boundary layer momentum thickness	m
Θ_{max}	Angle of $\overline{V}_{jetmax}$ with respect to X-axis	deg
C_d	2D Drag coefficient	-
C_f	Friction coefficient	-
C_L	3D Lift coefficient	-

C_l	2D Lift coefficient	-
C_m	2D Moment coefficient (defined positive down)	-
C_p	Coefficient of pressure	-
c_w	Wing chord	m
c_{flap}	Flap chord	m
C_{Lmax}	3D Maximum lift coefficient	-
C_{lmax}	2D Maximum lift coefficient	-
C_{pt}	Coefficient of total pressure	-
H	Boundary layer shape parameter	-
Ma	Mach number	-
P	Pressure	Pa
Re	Reynolds number	-
t	Maximum wing thickness	m
t/c	Wing thickness to chord ratio	-
TKE	Turbulent kinetic energy	m^2/s^2
Tu	Turbulence intensity	-
U	Velocity in the local x-direction	m
u^+	Law of the wall velocity	-
U_∞	Streamwise Freestream velocity	m/s
U_e	Streamwise External velocity	m/s
u_{rms}	Root-mean-square of the velocity fluctuation	m/s

V	Velocity in the local y-direction	m/s
V_∞	Transverse Freestream velocity	m/s
V_{jetmax}	Maximum velocity of local jet velocity profile	m/s
V_{merger}	Velocity at the point of confluence between jet and BL	m/s
V_{stall}	Aircraft stall speed	m/s
W_{TOmax}	Aircraft maximum take-off weight	N
x	Distance in the local x-direction (adjusted for surface inclination)	m
x/c_w	Horizontal position as percentage of wing chord	-
x_{tr}	Horizontal distance to transition from laminar to turbulent	m
y	Distance in local y-direction (adjusted for surface inclination)	m
y/δ	Normalized distance in local y-direction with local BL thickness	-
y^+	Law of the wall distance	-
y_{max}	Distance of V_{jetmax} in global coordinate system	m
X	Distance in the global x-direction	m
Y	Distance in the global y-direction	m

Chapter 1

Introduction

The engineering of aircraft can be characterized as a gargantuan effort against gravity, where for decades engineers have attempted to maximize the lift force generated, while incurring the least amount of weight penalty. But, as one wing configuration results in optimal aerodynamic conditions for cruise, the longest portion of most flight regimes, the aircraft must invariably negotiate a takeoff and landing. For this reason, engineers and scientists have developed high-lift devices such as flaps, slats, slots, leading edge root extensions, as well as other boundary layer control mechanisms.

Most high-lift devices were engineered during the first half of the 20^{th} century based on empirical evidence, and while these devices are very effective, the high-lift flow conditions involved are extremely complex and difficult to quantify. The importance of these devices cannot be overstated. Meredith [51], a senior specialist engineer from Boeing, used the following three examples to illustrate the importance of high lift devices on a generic large twin engine transport aircraft:

- a 0.10 increase in lift coefficient at a constant angle of attack is equivalent to reducing the approach attitude by about one degree. For a given aft body-to-ground clearance angle, the landing gear may be shortened resulting in a weight savings of $1400lbf$,
- a 1.5% increase in maximum lift coefficient is equivalent to $6600lbf$ increase in payload at a fixed approach speed, and
- a 1% increase in take-off Lift to Drag ratio is equivalent to a $2800lbf$ increase in payload, or a $150NM$ increase in range.

As important as these devices are, scientists and engineers have struggled for many decades to fully understand the flow conditions over a wing with deployed high-lift devices.

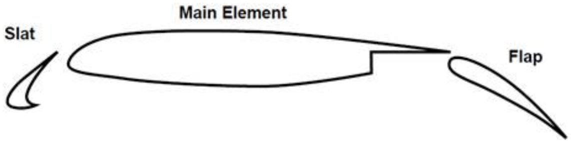

Figure 1.1: Three-element wing, University of Kansas [62]

Beginning at the leading edge of a typical three element wing shown in Figure 1.1, the complex flow may include [51] [71] [85]:

- laminar separation bubbles,
- shock-boundary layer interactions,
- attachment line transition from laminar to turbulent flow,
- transition of boundary layers from laminar to turbulent,
- relaminarization of a turbulent boundary layer,
- confluent wake and boundary layer interaction, and
- boundary layer separation.

As will be discussed in the literature survey, researchers have attempted to isolate some of these flow features and study them experimentally using various techniques including: hot film and hot wire anemometry, pressure sensors, Preston tubes, Planar Doppler Velocimetry (PDV), Particle Image Velocimetry (PIV), etc. The main difficulty however, is that in actual flight conditions, all these factors affect each other, and the resulting complexity is overwhelming. The experimental objective of this project was to investigate the two-dimensional flow over a wing with a deployed Fowler flap. The focus was to be on the confluence of the wing turbulent wake with the flap boundary layer, and investigate the effect of the variation of the flap gap and overlap on the wake-boundary layer confluence.

With the advent of rapid and affordable computational resources, scientists and engineers increasingly seek to capitalize on the benefits of Computational Fluid Dynamics (CFD). Where an experimental wind tunnel campaign may take months at a considerable overhead cost yielding only pre-determined flow characteristics, a CFD analysis of the same problem may only take days or weeks with significantly fewer expenses, while providing users with a complete set of flow data [46]. However, while CFD seems to be the answer, it is not without fault. By far the biggest obstacle is the validity of the calculated solution, because even with an inaccurate problem formulation, the CFD will converge to a solution. Obtaining a valid and correct solution is the true challenge of CFD, and naturally the more complex the flow field, the more difficult it is to obtain the sought-after accurate solution.

There are several CFD methods available to researchers; Direct Numerical Simulation (DNS) does not employ any modelling, and aims to completely resolve all scales of motion. This level of detail however, comes at a staggering computational cost. The grid resolution required for wall bounded flows is approximately $Re^{3.6}$, which renders this method too costly for all aerodynamic applications, as the flight Reynolds number, Re, based on the average wing chord is usually higher than 10^6.

An alternative method is Large Eddy Simulation (LES). LES is based on the premise that flow properties can be decomposed into large scales and subgrid scales. In theory, the behaviour of a fluid at the microscopic (subgrid) level is universal, and therefore independent of the large flow features. These subgrid scales are then modelled, while the large scales are computed and resolved. The difficulty is in establishing the scales of the flow prior to computing the solution, and then deciding on what is the smallest scale resolved, or what is the largest scale modelled. The computational cost of wall-bounded flows is not quite as staggering for LES as it is for DNS, but it is still considerable. With a combined inner and outer layer cost of $Re^{2.4}$, LES is currently out of reach for most aerodynamic applications, although further simplification can be made for high Reynolds number flows by not resolving the inner layer at all. The computational cost is thus reduced to $Re^{0.6}$ at the expense of the solution.

The third CFD method available is the Reynolds Averaged Navier-Stokes (RANS) method. This approach computes either time-averaged or phase-averaged flow properties. The principal difficulty with this approach is referred to as the closure problem. While the governing equations can be re-derived in terms of mean flow properties and their respective fluctuations, second order turbulent terms appear in the averaged momentum equation. These second order flux terms, or Reynolds stresses, must be resolved in order to obtain a solution. Unfortunately, the transport equations for the Reynolds stress terms yield third order flux terms, the transport equation for the third order flux terms contain fourth order flux terms, and so forth; hence the need for turbulence modelling in RANS. With multiple turbulence models available such as the Spalart-Allmaras model, the k-ϵ model, the k-ω model, Menter's Shear Stress model, etc., the computed solution using RANS is turbulence model dependent, because each turbulence model was based on a set of different flows and cannot be universal.

The last of the available CFD methods is Detached Eddy Simulation (DES). DES is a hybrid approach that combines RANS and LES. Since the computational cost for LES is greatest in the inner layer of wall-bounded flows, the inner layer is solved using RANS, while the outer layer employs LES. This methodology is the newest form of CFD, and is consequently not as developed as the three preceding methods. DES becomes problematic at the interface between the RANS and LES grids. At this junction, while the values in one cell are computed using time averaged properties (RANS), the adjoining cell contains time dependent flow variables (LES). Thus, as the LES cell computes the velocity fluctuation and passes that information to the RANS cell, the RANS cell cannot relay the same information travelling in the opposite direction, and yet the flow must be continuous across both cells. Research to resolve theses concern is ongoing [91].

As can be seen, a considerable level of vigilance is required to ensure that a CFD computed solution is accurate as all CFD methods have their short comings. The CFD objective of this study was to investigate the effect of the variation of a flap gap and overlap of a deployed Fowler flap in landing configuration on the principal aerodynamic loads (C_l, C_d, C_m) as well as the wake-boundary layer confluence. CFD solutions were computed using RANS (Fluent) with a supporting experimental campaign carried out using hot wire anemometry and PIV measurements in order to ascertain the level of accuracy of the CFD simulations.

1.1 Motivation

As will be discussed in a comprehensive literature survey, the use of CFD has already gained a permanent foothold in the field of fluid and aerodynamic research using proprietary codes such as TAU and FLOWer employed at DLR (*Deutsches Zentrum für Luft und Raumfahrt*) [75] and OVERFLOW (OVERset grid FLOW solver) used at and developed by the National Aeronautics and Space Administration (NASA). The question then becomes, how do commercially available CFD software packages compare with the high end proprietary codes, when applied to the complex flow conditions involving high lift devices.

With the momentary decline of the world economy in the first decade of the 21^{st} century, aircraft maintenance became an even greater priority for civilian and military fleets as new procurement budgets were slashed. With an ageing fleet of CP-140 Aurora aircraft in its inventory and a growing maintenance cost, the Canadian Forces (CF) requested an analysis of the aerodynamic implication of the growth of the flap gap and overlap beyond the manufacturer specified limits. Employing an experimental as well as CFD investigation, this was recognized as the perfect opportunity to validate the computational solutions generated by a commercially available CFD code (Fluent) with experimental data collected using a Particle Image Velocimetry (PIV). While CFD was used to model the various flap gap and overlap configurations calculating the changes in the principal aerodynamic forces, the validity of these simulations was evaluated based on the accuracy of the wake-boundary layer confluence over the Fowler flap.

1.2 Objectives

The objective of this investigation was to explore the flow interactions involving a Fowler flap deployed to 40° deflection during landing configuration. The approach was to conduct a quantitative parametric study focusing on the effect of the flap gap and overlap growth on the aerodynamic forces of the wing. In order to ensure the validity and accuracy of both the experimental and numerical efforts, the following interim objectives were set out.

Experiment

As detailed in Chapter 2, a considerable amount of work has been done on Fowler flaps in the past. While Wentz et al [106] focused on the pressure changes with a variation in the flap gap, they did not detail the flow behaviour with a variation in overlap. In this investigation, a 2D PIV was employed to study the flow changes with a variation of flap gap and overlap.

Due to the considerable difference between the flight Reynolds number (24×10^6) and the Reynolds number achievable in the wind tunnel, the first objective was to establish flow similarity between the flight condition and the experimental wind tunnel conditions. The objective of the ensuing wind tunnel experiment was to first collect flow data using a PIV system over the wing-flap assembly in a clean configuration (flap stowed). Once the test equipment and data collection apparatus were calibrated and two dimensional flow was confirmed, the next objective was to systematically vary the position of the Fowler flap with respect to the main wing.

The CFD validation was to be based entirely on the comparison of velocity profiles, turbulent kinetic energy (TKE) profiles and boundary layer characteristics to the wind tunnel experiment at key locations.

CFD

The objective of the CFD analysis was to compute the 2D flow over the CP-140 wing in clean (flap stowed) and landing (flap deployed and deflected to 40°) configuration.

In order to ascertain the accuracy of current CFD software packages, all the experimental configurations were solved numerically. In addition, a systematic variation of the flap gap, overlap as well as the angle of attack was also conducted using RANS (Fluent). The goal was to employ three turbulence models (Spalart-Allmaras model (SA), Shear Stress Transport model (SST), and Reynolds Stress Transport model (RSM)) in order to quantify the effect of the turbulence model on the solution, as well as to assess the accuracy of the computed solutions.

1.3 Organization

The organization of this thesis closely follows the chronological development of the work conducted. Following a comprehensive Literature survey in Chapter 2, Chapter 3 details the development of the model geometry. Although the scaling differed from the experiment to the CFD, the same model geometry was used in both campaigns. Chapter 4 outlines the methodology and development of the CFD models, while Chapter 5 summarizes the experimental model design as well as the experimental campaign. Finally, Chapter 6 presents the results obtained from both the experimental and CFD investigations, while Chapter 7 presents the findings and interpretation of the flow field within the flap slot. Both Chapters 6 and 7 contain the results, analysis and discussion.

Chapter 2

Literature survey

2.1 Experimental Research

Harlan D. Fowler [104] introduced the *Fowler Variable Area Wing* in 1931, and using this new configuration, he was able to achieve a dramatic increase in the lift coefficient. While the plain wing consisting of a Clark Y airfoil profile generated a C_{Lmax} of 1.27, the extended Fowler flap deflected to 40° produced a remarkable C_{Lmax} of 3.17. Fowler [104] outlined the motivations behind this new high lift device as:

- Increasing the area by means of an extended surface,
- Increasing the effective camber by means of the flap, and
- Providing a slot to maintain "unburbled" flow at high angles of attack.

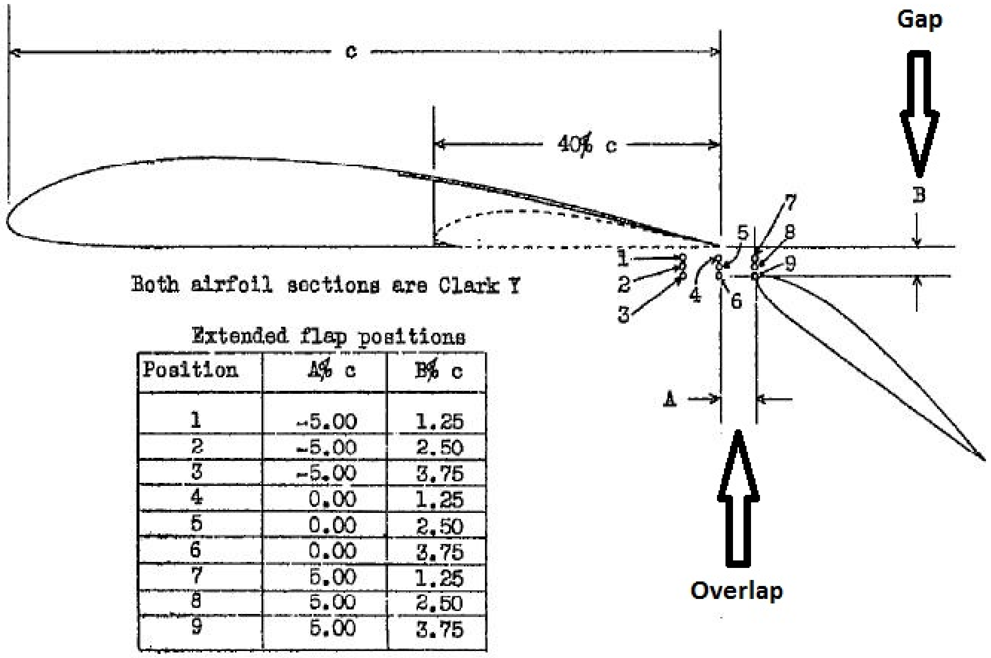

Extended flap positions

Position	A% c	B% c
1	-5.00	1.25
2	-5.00	2.50
3	-5.00	3.75
4	0.00	1.25
5	0.00	2.50
6	0.00	3.75
7	5.00	1.25
8	5.00	2.50
9	5.00	3.75

Figure 2.1: The Fowler Wing [105]

From the beginning, Fowler understood the importance of the relative position of the extended flap with respect to the main wing. Through an experimental investigation, he ascertained that the maximum lift was achieved with a gap of $0.025c_w$ and an overlap of $0.0c_w$. Weick and Platt [104] confirmed Fowler's initial findings by investigating the 9 different flap positions outlined in Figure 2.1, and while the optimum flap gap and overlap were readily identified, the reason behind this particular spacing eluded aerodynamicists due to the complexity in high lift flows.

With a war looming, the Fowler flap was quickly evaluated by NACA via successive investigations and evaluations. First, the benefits of a Fowler flap with a leading edge variable slot were investigated by Weick and Platt [105], which was then followed by Platt's [69] investigation of the potential benefits of various combinations of wing and flap airfoil profiles. In the same year, Platt [68] also completed a parametric study of the optimal flap chord and associated flap loads, which was then succeeded by a documentation of the effect of the flap chord on flap pressure distributions by Wenzinger and Anderson [110]. Finally, in 1939, a detailed study was conducted of the slot shape and location in various flap configurations including Fowler flaps by Wenzinger and Harris [111]. Although the report was not published until 1951, in 1942 Young [116] was the first to attempt to quantify the effect of the size of the flap cut-out as well as the chord extension of a Fowler flap on induced drag using the lifting line theory, while many others delved into investigations of leading edge stall, trailing edge stall and separation bubbles [30] [64] [15] [35], in 1953 the Aeronautical Research Council [117] published a comprehensive report summarizing the aerodynamic characteristics of flaps. From the amassed body of empirical data, it was found that:

- the combination of a leading edge slat with a trailing edge Fowler flap does not result in any more benefit than the sum of the two individual high lift devices;
- while the flap airfoil profile does not significantly improve lift nor drag, the flap leading edge radius and shape can have considerable effect on the pressure peak generated over the flapped portion of the wing as well as the clean configuration

aerodynamics;

- there is little to gain in deflecting flaps beyond 40° or designing a flap chord longer than $0.30c_w$ of the wing chord; and
- while the optimal flap gap and overlap position can be found for any wing-flap configuration, the optimal flap cut-out for induced drag is less than $0.10c_w$.

In 1970, Foster et al [28] conducted a thorough experimental investigation of the boundary layer behaviour of a slotted flap configuration in optimum flap position. After investigating both the take-off (10° flap deflection, δ_{flap}) and landing configurations ($\delta_{flap} = 30°$), they found that the optimum flap position for the landing configuration was with a gap of $0.023c_w$ and an overlap of $(-0.01)c_w$ (flap leading edge just ahead of wing shroud). Foster et al [28] made several important discoveries, which are listed below:

- if inviscid theory predicts an optimum gap within a specific range, the experimental optimum will be very close to this value,
- both the variations of the wing lift with gap, and of the flap lift with gap, depart from the theoretical trends for gaps below optimum, but the biggest loss of lift occurs for the wing lift,
- near the optimum flap position, there is only a weak interference between the wake from the wing and the boundary layer on the flap, and
- the limit on this behaviour occurs when the boundary layer on the flap, and that on the shroud lower surface, just meet. This also indicates that the Reynolds number will influence the optimum flap position.

Following the illuminating work of Foster et al, Omar et al [63] investigated the utility of supercritical airfoils in high lift systems, Korbacher [41] pursued powered high lift systems, and Smith [89] published his seminal work on the theory behind high lift aerodynamics.

Searching for the optimum airfoil profile for transonic flight, in 1973 NASA introduced the general aviation airfoils GA(W)-1 and GA(W)-2 [49]. These airfoils were subsequently adopted by Wentz and Seetharam, who proceeded to conduct experimental campaigns implementing a Fowler flap for high performance. With 96% of the Fowler flap nested within the GA(W)-1 main wing, Wentz and Seetharam [107] first conducted two-dimensional flow tests of a $0.29c_w$ and $0.30c_w$ flap chord at Reynolds numbers ranging from 2.2 x 10^6 to 2.9 x 10^6 at a flap deflection of $\delta_{flap} = 40°$ and the optimal flap position of gap $= 0.027c_w$ and overlap $= 0.007c_w$. Collecting force, pressure and flow visualization data, the highest C_{lmax} obtained was for the $0.30c_w$ Fowler flap configuration at $Re = 2.2$ x 10^6, resulting in a $C_{lmax} = 3.8$.

Wentz [109] then carried out two-dimensional wind tunnel tests using the GA(W)-2 airfoil employing an aileron, Fowler flap, slotted flap as well as a spoiler. The maximum lift coefficient obtained utilized the Fowler flap, developing $C_{lmax} = 3.82$ at an optimum flap position of gap $= 0.012c_w$ and overlap $= (-0.0175)c_w$ (flap leading edge upstream from the wing trailing edge).

Next, Wentz and Seetharam [108] studied the impact of slot variation on flow separation employing a narrow ($0.02c_w$), optimum ($0.03c_w$) and wide ($0.04c_w$) slot gaps using hot-film anemometry at the slot exit. It was found that for all three angles of attack, the pressure profiles at the slot exit show centre regions of relatively constant total pressure, c_{pt}, even though the free-stream value of $c_{pt} = 1.0$ is not achieved. It is therefore reasonable to refer to a ‘core flow’ of constant energy with sheared flow above and below this core. With the wide gap, the core is displaced upward compared to the optimum gap case, indicating a tendency for boundary layer thickening on the flap. Pressure measurements further downstream showed that the reported core vanishes near mid-flap. Thus, it appears that Foster’s criteria of minimal boundary layer separation at the slot exit seems to be in error and that in fact a finite core must be retained at the slot exit, even for the optimum gap position.

In conclusion to the above experiments, Wentz and Ostowari [106] investigated slot-gap variation as well as cove shape modifications using a $0.30c_w$ Fowler flap. They found that, while the narrower than optimum gap has a larger region of high turbulence with intermittent reversal at the C_{lmax} angle of attack, the larger than optimum gap has separated regions over the flap at all angles of attack, thus producing substantially lower lift at pre-stall and C_{lmax} angles of attack. In fact, with the wider than optimal gap, the efflux from the slot exit does not follow the flap contour, but rather flows nearly stream-wise, merging with the airfoil forward element wake. The results from the cove shape study indicated that local flow separation within the flap cove region does not seem to be a hindrance to attainment of high C_{lmax} as long as the flow reattaches ahead of the flap slot. It was found, that a completely blended cove which did not have flow separation actually produced a slightly lower C_l than a more conventional cove with flow separation and reattachment. Detailed measurements of the three cove regions examined indicated that, while the details of the flow within the cove differ, all three coves produced very similar flap slot velocity profiles. These findings were also confirmed by Alemdaroglu [5] and Zabloudil et al [118].

The one aspect of the flow that Wentz did not investigate, was the effect of flow confluence over the flap. Bario et al [7] published a paper documenting the confluence of a wake and a boundary layer, and although their findings were not conclusive, they served to highlight the need for more research in this specific area. This void was subsequently filled by Squire and Zhou [94], who first investigated the interaction of a wake and a turbulent boundary layer in zero and adverse pressure gradients. They found that the level of turbulence in the wake has the strongest influence on the interaction, but more importantly, that numerical solutions of confluent flow relying on eddy viscosity turbulence models are incapable of accurately depicting the flow physics involved. Squire and Argoropoulos [93], Squire [92] and Moghadam and Squire [54] then furthered this research by experimental and numerical investigation of the interaction between the wake of a slat and the boundary layer on the main wing in two and three dimensional flows. These efforts were also pursued by Thomas et al [100] at NASA and Ying et al [113] at Boeing, who confirmed that there is little interaction between the wing wake and the flap boundary layer, but that the interaction between the slat wake and the wing boundary layer is considerable (hence most research is concentrated in that area). Thomas et al [100] also found, that in the initial region of the interaction, the shear stress and mean velocity gradient normal to the wall can have opposite signs which implies that the effective eddy viscosity is negative. This severely restricts the validity of all eddy viscosity based turbulence models still in use today, and thus researchers generate proprietary codes to solve confluent flows, or are forced to resort to the Reynolds Stress Model (RSM) or its variants.

In order to close the gap between the flight and wind tunnel Reynolds numbers, Spaid [90] focused his attention on high Reynolds number wind tunnel testing and flight testing. With the advent of advanced integrated sensors reported on by Greff [32], Yip et al [114] conducted a subsonic transport high-lift research program employing a B-737-100 with a triple-slotted Fowler flap for comparison with wind-tunnel and computational results. The studies focused on shock/boundary layer interaction on the slat, flow separation and reattachment, confluent turbulent boundary layer, flow transition, relaminarisation, employing Preston tubes, hot films, rakes and pressure belts, with the findings reported by Yip et al [115], VanDam [102] and VanDam [101]. The main finding of this research programme was the continual presence of laminar flow conditions over the wing even during flight, and the turbulent contamination of the laminar flow regions affected by upstream elements such as slats.

Finally, in 1997, Bertelrud et al [9], Bourassa et al [11], McGinley et al [50], and Moens et al [52] tackled the experimental and numerical investigation of flow transition in high lift devices, while Paschal et al [65], Takeda et al [96], Baragona et al [6], and Biber [10] focused on the unsteady aerodynamic effects in high lift systems.

2.2 Numerical Research

Numerical studies of high-lift aerodynamics started in 1971 when NASA commissioned a computer program, which evaluated the aerodynamic characteristics of multi-component airfoils in subsonic flows [95]. It was suggested that in most applications, the slot-flow analysis may be by-passed in the calculation sequence except where warranted by the more unique slot configurations. To improve the computation of slot flow and free turbulent mixing computations, Morel and Torda [56] tested Bradshaw et al's [12] interaction hypothesis, only to find that the structure of turbulence in free shear flows is less universal than that in boundary layers, but they concluded that the interaction hypothesis of Bradshaw to free shear flow is a "workable concept".

In 1993, as part of the Advisory Group for Aerospace Research and Development (AGARD) symposium focusing on high lift aerodynamics, Navier-Stokes calculations were performed on multi-element airfoils using a chimera based solver. A chimera based grid avoids the need for precise alignment of mesh blocks in complex geometries. Instead, the grid consists of independently constructed blocks that overlap. A Chimera based solver is a solver that can accommodate the domain discontinuity of a Chimera grid by interpolating between the grid blocks to construct a continuous flow. During the AGARD conference, it was found that for the two-element case without confluent boundary layer flow, excellent prediction was obtained up to stall, which was within 2% of the experimental values. Less accurate results were obtained for the case exhibiting confluent boundary layer flow [37]. This research was furthered by Jones et al [39] who investigated multi-zonal grid techniques, while Mathias et al [47] and Jirasek et al [38] focused strictly on the flow about the flap trailing edge. Jones et al [39] concluded that while the absolute level of the computed lift may not be in precise agreement with the experimental data, the fact that the difference between computation and experiment remains relatively invariant with angle of attack suggests that trends can be reliably detected from the computations. Both Mathias et al [47] and Jirasek et al [38] discovered that the precise geometric definition of the flap trailing edge (TE) can have significant impact on the computed results. While some researchers attempted to simplify the sharp geometry of a flap TE in an effort to affect a higher quality mesh, the simplified mesh construction came at the expense of the solution accuracy of the flow in that region.

In the 1990s, there were three numerical approaches, DNS, LES and RANS. Due to the astronomic computational requirements of DNS and LES, RANS simulations dominated the numerical research scene of high lift devices in the 1990s and early 2000s. Murayama et al [61] investigated the effect of mesh construction on the solution accuracy, and they found that while C_l was less sensitive to mesh density, and the difference was little between structured and unstructured meshes, the difference in C_d was much larger. However, with careful distribution of mesh points in unstructured meshes, the detail in flow physics could also be well resolved. Murayama and Yamamoto [60] determined that the computational domain boundary should be at least 50 chord lengths away from the body surface, and increased mesh density within 2 chord lengths of the body is required to accurately predict drag.

As discussed in the introduction, RANS simulations are largely dependent on the turbulence model employed. For this reason, considerable effort has been dedicated to quantifying the effect of turbulence model selection on the solution. Rogers et al [73] began this line of inquiry by evaluating four turbulence models (Baldwin-Barth, Spalart-Allmaras, Shear Stress Transport, and Durbin-Mansour). They found "excellent agreement between computational and experimental surface pressures, but only moderately good agreement was seen in the velocity profile data. In general, the difference between the predictions of the different models was less than the difference between the computational and experimental data". Some researchers believed that the poor simulation-to-experiment correlation was due to a lack of transition prediction modelling, which was investigated by Rumsey et al [83], who noted that the transition location is crucial to the accurate computation of boundary layer velocity profiles. Rumsey et al [83] also compared several turbulence models and they found that the SST model was more accurate in separated flow regions, the SA model performed better for attached flows and wakes including the region in which the wake and boundary layer merged, and that the explicit algebraic stress turbulence model (EASM) overall yielded results that were similar to linear eddy-viscosity turbulence models. Rumsey and Gatski [82] then investigated a new $k-\omega$ form of the EASM which included non-linear terms to improve predictions of turbulent shear stress behind the trailing edge of the main element and near mid flap. They found that the $k-\epsilon$ form of the EASM was "ill suited" for use in this flow, because it overpredicts turbulence regions of adverse-pressure gradient wall bounded flows. The new $k-\omega$ form does not suffer from this problem, and was shown to improve the prediction of the turbulent shear stress behaviour. Rumsey and Gatski [82] also noted that curvature corrections did not have significant effect in the flap region where the flow field undergoes the greatest curvature.

The one significant drawback of the EASM is its computational cost. Reyes et al [72] deemed this cost high enough to declare the $k-\omega$ EASM turbulence model "unsuited and computationally too expensive" for high-lift wing application. While most researchers have steered clear of the full Reynolds Stress Transport Model (RSM) due to its immense computational cost (7 equations), Davidson [19] illustrated the superiority of the RSM model over the $k-\epsilon$ turbulence model in the prediction of the stall angle of a low-speed airfoil. Chaouat [13] extended Davidson's work to high-lift flows and confirmed the superiority of RSM over the $k-\epsilon$ as well as the SST model. They found that the RSM model predicts numerically these airfoil flows for a large range of incidences in very good agreement with the experimental data.

A high-lift workshop was hosted by NASA [40] in 1997 in order to compare various numerical solutions of two-dimensional flow revealing the following findings:

- in general, RANS methods showed less variability among codes than did potential and Euler solvers coupled with boundary-layer solution techniques,
- lift was more accurately predicted than drag for both methods,
- the CFD methods did well in predicting lift and drag changes due to variations in Reynolds number, however, they did not perform well when predicting lift and drag increments due to changing flap gap,
- pressure and skin friction compared favourably with experiment for most codes, and
- there was a large variability in most velocity profile predictions.

At the McDonnell Douglas Corporation, Lynch et al [46] used their state of the art NSU2D RANS solver to investigate the accuracy of two dimensional CFD codes in predicting simple changes in flap rigging and flap deflection. They found that the predictions obtained with the one-equation turbulence model (SA) closely approximated the overall flow mechanism limiting maximum lift, but they did not adequately capture changes due to configuration modifications which influence the merging and spreading of shear layers and wakes. Their experimental results suggested that flow separation on the flap upper surface at approach conditions is often a limiting factor in establishing appropriate flap rigging, but the RANS CFD predictions of this flow phenomenon are not reliable. The study of two-dimensional flow over high-lift devices was then furthered by Murayama et al [59], who found that without transition modelling, Menter's SST turbulence model predicted the best results of aerodynamic forces, the maximum lift and the stall angle. In a further study, Murayama et al [58] also found that the difference between structured and unstructured grids was negligible, although a higher number of mesh points was required in an unstructured grid to match the accuracy of a structured grid. Murayama et al [57] expanded their study to three-dimensional flows over high lift devices. They confirmed that although at lower angles of attack a structured grid has the advantage of a lower computational cost, it takes considerably longer to generate initially. At higher angles of attack, the difference between the results of the structured and unstructured mesh became larger, with flow separation on the slat being particularly sensitive to the mesh density. Although the solution accuracy achieved was excellent for the lift force (a mere 1.4% difference in C_{Lmax}), the difference in drag calculation ranged between 3-6%. More importantly however, Murayama et al [57] found that the mesh resolution near the wing-fuselage junction was very important in improving the accuracy of three-dimensional computational results.

A large number of studies investigating the three dimensional aerodynamics of high lift systems originated in the early 1990s. A surface panel method and a Euler solution was compared to high-lift flight test data by Dodbele [22], who found considerable differences when the computational surface pressures were compared with the results from the high lift flight test. Edge and Perkins [23] demonstrated the ability of a low-order potential solver (PMARC) in predicting accurate inviscid 3-D flow features in complex geometries, by establishing that the panel method is able to predict reasonably well the pressure distributions of a multi-element wing. At NASA, Mavriplis and Pirzdeh [48] carried out a complete geometry to drag-polar analysis of a three dimensional high-lift configuration of a transport aircraft using RANS. They found that the experimental lift values are over-predicted by both fine and coarse grid results. However the slope of the lift curve is reproduced very accurately by both computations. Upon closer inspection, Mavriplis and Pirzdeh [48] also found that isolated flow features such as the slat wake are not captured adequately, because there had been no effort to anisotropically increase the grid resolution in these areas. A similar large scale project called MEGAFLOW [42] was initiated and led by the Deutches Zentrum für Luft-und Raumfahrt (DLR), employing their RANS solvers FLOWer (structured) and TAU (unstructured). The objective of MEGAFLOW was the development and validation of a dependable and efficient numerical tool for the aerodynamic simulation of complete aircraft in cruise as well as take-off and landing configurations. Rudnik et al [78] reported good comparison to experimental data for moderate angles of attack, α. Beyond $\alpha = 15°$, the FLOWer solution employing the $k-\omega$ turbulence model exhibited premature separation in the area of the flap cutout, which was not observed in the experiments, while the TAU code, which employed the SA turbulence model, did not exhibit this type of premature separation. Their results indicated that the stall mechanism is not properly simulated by the numerical approaches. Some potential causes of the discrepancies listed include: influence of artificial dissipation by incorporating preconditioning, turbulence model, lack of transition prescription, and minor geometrical differences between experimental and CFD geometries.

Following DLR's lead, Rogers et al [74] set out to perform a CFD analysis of an entire high-lift aircraft from CAD to post-processed solution in 50 working days. Rogers et al [74] were able to meet this objective using NASA's OVERFLOW software modelling a Boeing 777, while they investigated the effects of sealing a spanwise gap between two leading edge components and the effect of adding a nacelle chine. They reported that at approach conditions, the computational lift was within 1.5% of the experiment and the computed drag was within 4%. However, the computational model under-predicted the lift at higher angles of attack and missed its maximum lift by nearly 11%. As a result of the poor correlation reported by Rogers et al [74] at higher angles of attack, Rumsey et al [84] investigated the effect of side wall venting on three-dimensional flow. Rumsey et al [84] found that, while the modelling of the side wall venting in the CFD simulation reduced the simulation-to-experiment discrepancy from 11% to 5%, the effect of modelling support brackets brought the simulation to within 2-3% of the experimental results. Further lessons learned by Rumsey et al [84] included:

- 2-D CFD should not be expected to agree with the nominally 2-D wind tunnel experiment at high lift conditions because the experiment lost its 2-D character at high angles of attack, and
- 3-D CFD using the current grids and methodology compared well with the experiment at a low angle of attack, but did not adequately model the character of the wind tunnel flow field near maximum lift.

A similar automated CFD analysis was also investigated by Moitra [55], who reported that their automated software package was validated for slat and flap effectiveness studies, Reynolds number effects, and gap sensitivities. He demonstrated that the prediction of gap sensitivities for a range of flow conditions and geometric configurations was in very good agreement with test data.

By far, the largest project investigating high-lift systems in transport aircraft was the European High Lift Programme I and II (EUROLIFT I&II). Building on the work of ONERA [98] and GARTEUR [97] Aerodynamics Action Groups who investigated an Airbus A310 in take-off and landing configuration in an extensive wind tunnel and flight test campaign, EUROLIFT I [99] aimed to improve the understanding of dominant high-lift flow phenomena, and to account for these effects early on in the design process. While RANS simulations were utilized to prepare the test campaign, EUROLIFT I was primarily an experimental investigation, where Séraudie et al [88] investigated the transition behaviour under the Reynolds number influence. Under the leadership of Airbus-Deutschland, the EUROLIFT II [80] programme included a consortium of 13 partners from the European Airframe industry and European research institutions with general objectives of validation of numerical and theoretical methods for the exact prediction of the aerodynamics of a complete aircraft in high-lift configuration at flight Reynolds numbers by employing state-of-the art RANS-methods along with the European Transonic Wind Tunnel (ETW) and the Low Speed Wind Tunnel (LSWT) of Airbus-Deutschland. Beginning with a simple wing-fuselage configuration, the model complexity was increased in four stages. The last stage included the flaps, slats, pylon mounted nacelles and strakes. The second stage configuration, which included the wing, fuselage, flaps and slats, was analysed numerically by a large number of 3D RANS CFD codes. Rudnik et al [76] reported that maximum lift is simulated in fair agreement to the experimental evidence for wind tunnel conditions. Nevertheless, a considerable scatter of the results of a variety of European codes is observed, especially when computing drag. In their analysis of turbulence models, Rudnik et al [76] found that for high lift flows, the explicit algebraic Reynolds stress model (EARSM) has been shown not to offer the benefits observed in transonic applications. As part of EUROLIFT II, Moens et al [53] focused on the impact of transition on performance investigating Reynolds number dependent transition processes such as Tollmien-Schlichting and cross-flow instability growth, attachment line contamination, relaminarisation and separation bubbles. They verified that computations with transition prescribed using experimental results at limited wing sections led to an improvement of the performance prediction; close to maximum lift, the complex shape of the transition line on the wing surface must be considered in order to produce a more realistic solution. In particular when separation bubbles are present, a high sensitivity of the bubble size to the prescribed transition location has been shown. Various transition prediction tools were then evaluated; however, their utility was found to be quite limited. Rudnik [81] then investigated the stall behaviour of the various high-lift configurations. Specifically, Rudnik [81] analysed the stall behaviour spanwise pressure distributions at maximum lift and at lift breakdown at the two Reynolds numbers (2.3 x 10^6 and 25 x 10^6) for each of the four complexity stages. He found that mounting a nacelle and pylon to the configuration led to a distinct change in the location of the lift breakdown, which is not affected by Reynolds number. By adding the nacelle strake, the lift breakdown inboard of the nacelle is successfully alleviated. In a cooperative effort between DLR, ONERA, the Swedish Defense Research Agency and Centro Italiano Ricerche Aerospaziali, Wild et al [112] targeted the improvement of the take-off performance of a generic transport aircraft by a redesign of the trailing edge flap. A numerical optimization method was first performed using CFD analysis results of a two-dimensional wing-flap configuration. The results were then carefully transferred to a three-dimensional model, and a wind tunnel verification was performed. The comparison of numerically predicted improvements with experimental data showed an astonishing agreement [112]. Rudnik and Germain [77] investigated the Reynolds number scaling effects using the various configurations with respect to lift curves and drag polars. They investigated Reynolds number ranging from 1.5 x 10^6 to 25 x 10^6, finding that the strongest increase in maximum lift was observed up to Re = 5 x 10^6. In the intermediate range (Re = 5 x 10^6 to 15 x 10^6), a highly non-linear behaviour of the maximum-lift values was observed. Burg et al [103] studied the impact of geometric details in high-lift configurations on flow separation near maximum lift. Their objective was to examine the influence of pressure tube bundles, wind tunnel walls and model mounting and the effect of model deformation for a high-lift wind tunnel half-model using viscous flow computations. Burg et al [103] reported that of all configurations considered, the mounting of the half-model had the most significant effect on the aerodynamic coefficients. Specifically, the inclusion of wind tunnel walls explained the main difference between the experimental and the computed forces due to crossflow velocity components caused by the model mounting. They further suggested that this increased accuracy comes at a tremendous cost. While the model deformation and the inclusion of slat tracks and pressure bundles result in an increased cost of about 10% each, the inclusion of the wind tunnel walls and model mounting increases the computational cost by approximately 400%. This staggering cost increase is the result of the necessity to generate computational viscous grids for the entire wind tunnel, as well as the need to set the back pressure to match the upstream flow conditions [103]. Finally, following the extensive wind tunnel campaigns utilising the ETW and LSWT, a series of highly instrumented flight tests were planned to further validate the CFD results. Rudnik et al [79] reported on their progress on the implementation of integrated boundary layer rakes, boundary layer probes, in-flight PIV, and wing deformation measurements using Image Pattern Correlation Techniques for use during their flight testing stage on a A320-200 aircraft.

Although the predominant CFD method employed for the analysis of high-lift systems is RANS, some researchers have explored the field with other methods. Piomelli et al [67] employed Large Eddy Simulation (LES) to study the wake/boundary layer interaction at low Reynolds numbers ($Re = 385$ and $Re = 1155$), while Cummings et al [17] executed simulations of a NACA $63_2 - 215$ with a leading edge slat and a trailing edge Fowler flap using Detached Eddy Simulation (DES).

Chapter 3

Model Geometry

Since the primary objective of this project was to provide a quantitative analysis of the effect of the variation of the flap gap and overlap of a CP-140 Aurora (P-3 Orion) shown in Figure 3.1, it was essential to obtain or generate an accurate computer-aided design (CAD) model of the aircraft wing in question. In 2002, the National Research Council Canada (NRC) conducted wind tunnel experiments and CFD analyses in co-operation with the Directorate of Technical Airworthiness and Engineering Support (DTAES) as part of the CP-140 Service Life Assessment Program (SLAP). For this purpose, NRC generated a CAD model, which was verified and met the approval of the aircraft's manufacturer (Lockheed Martin) for accuracy. The wing portion of this NRC generated CAD model was obtained for the use in the present investigation from NRC [8]. The CAD model included the solid wing only (it did not include the engines, nacelles, propellers, flaps or ailerons) from wing station (WS) 90 outboard. WS90 is located 90 inches from the centre line of the fuselage. The model scale was determined to be 1:16 based on the measured wing tip chord of the CAD model. General aircraft specification were obtained from the NASA Airborne Laboratory Experimenter Handbook [16] for their P-3B Orion, which is the US variant of the

Figure 3.1: CP-140 Aurora[27]

CP-140 Aurora.

The NRC CAD model was generated based on laser scans of an actual CP-140 aircraft; the measurements were conducted in the clean, take-off, and landing configurations. The resulting coordinates from these scans were also obtained from NRC, and utilizing the scan of the aircraft in landing configuration (flap deployed and deflected to 40°), the flap profile was obtained following the application of rotation matrices accounting for the trailing edge sweep angle, wing anhedral, wing twist and flap deflection angle.

Using the CAD software Solidworks, the flap profile was then cut out of the existing CAD model to obtain the present flap geometry. Unfortunately, no information could be obtained for the geometry of the flap cove from the NRC measurements, hence the maximum allowable gap was assumed in accordance with Figure 3.2 and a flap cove was generated mimicking the flap profile. It was recognized that this is an unquantifiable uncertainty in this investigation. Fortunately, Wentz and Ostowari [106], who investigated the effect of the flap cove geometry of a deployed Fowler flap, found that three different cove geometries showed very similar flap slot velocity profiles. Since the objective of this investigation was the change in the aerodynamic force and not its absolute value, it was surmised that the flap cove geometry did not introduce a significant source of error. The clean configuration geometry is illustrated in Figure 3.3. Next, the hinge line of the flap was determined, in order to define the

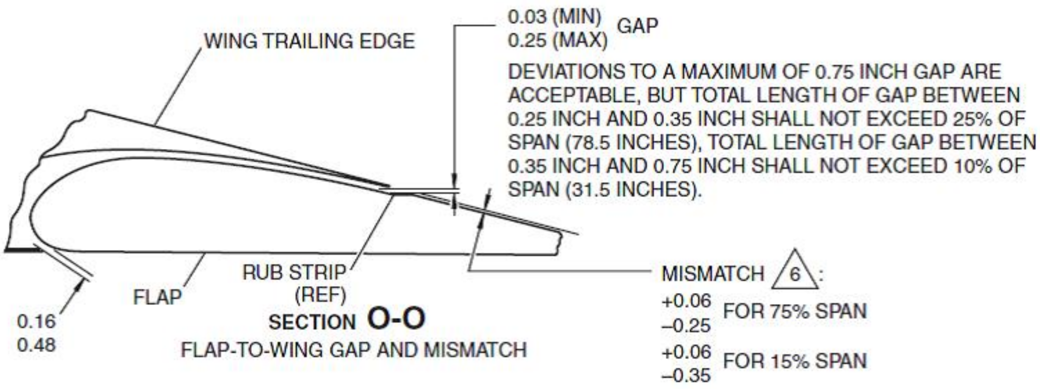

Figure 3.2: Stowed flap tolerances from technical publication [1]

Figure 3.3: 3D CAD model - Clean Configuration

landing configuration flap position. The flap hinge line location, its travel path and its fully deployed position (landing configuration) were determined using data from a combination of sources. The initial NRC scan included the definition of the flap track path. Adams [4] provided engineering drawings of the wing, while Harrison [34] took measurements of the flap gap and overlap of a newly re-winged CP-140 Aurora at IMP in Halifax. Utilizing the information from these sources, the landing configuration CAD model was constructed and is presently illustrated in Figure 3.4. Since this investigation consisted of a two-dimensional flow analysis, the representative cross-section of the wing was then selected at WS188, which is located directly behind the inboard engine. As the flap chord is constant along the entire flap span and the wing

Figure 3.4: 3D CAD model - Landing Configuration

has a taper ratio of $\lambda = 0.4$, the percent flap chord of the total wing chord varied along the wing span. At the selected location, WS188, the flap chord was 25% of the wing chord with the flap stowed ($c_{flap} = 0.25c_w$).

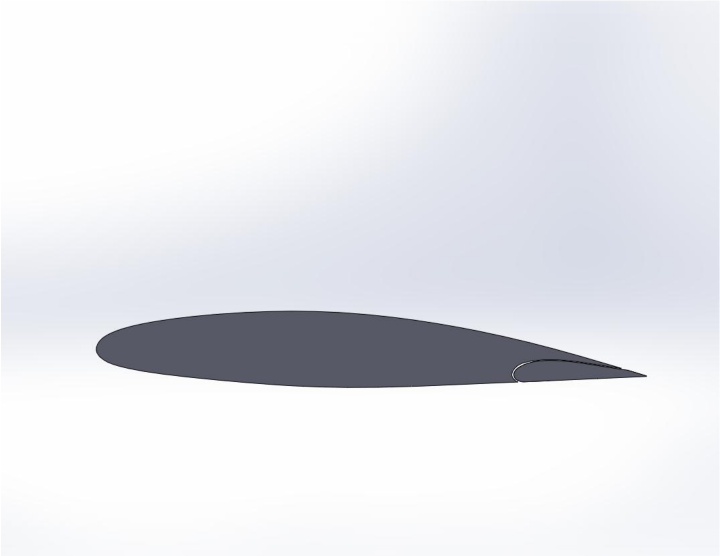

Figure 3.5: 2D CAD model - Clean Configuration

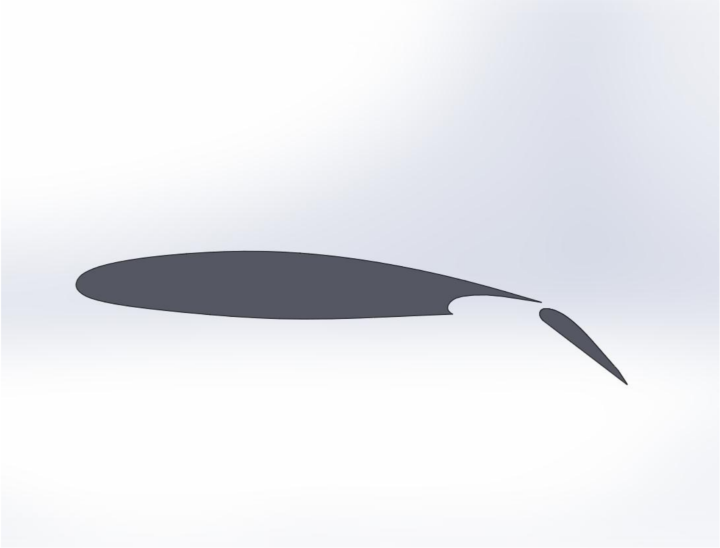

Figure 3.6: 2D CAD model - Landing Configuration

Chapter 4

Numerical Simulations

4.1 Geometry

In the present work, a 2D wing profile from the CP-140 Aurora was investigated in the clean and landing configurations. The focus of this study was on the effect of the variation of the flap gap and overlap on the aerodynamic performance of the wing in landing configuration. The complete definition of the geometry was outlined in Chapter 3. The airfoil profile of the CP-140 wing is based on the NACA 0014-1.10 40/1.051 [†] profile at the wing root, and NACA 0012-1.10 40/1.051 profile at the wing tip [16]. The simulations used an NRC CAD model of the CP-140 aircraft. The wing chord (c_w) with the flap nested measured $c_w = 184$". The measured maximum thickness to chord ratio of the selected cross-section was $t/c = 0.14$. Two configurations were investigated: clean configuration with $\delta_{flap} = 0°$ and landing configuration $\delta_{flap} = 40°$. All configurations investigated were solved using the Computational Fluid Dynamics (CFD) code ANSYS Fluent 14.0.

4.2 Fluent 14.0 solver validation

The commercially available CFD solver, Fluent 14.0$^{\mathrm{TM}}$, has been available for many years. Because of its availability, this software package has been used and validated in the scientific community for a number of flows. For example, the validation work of [86] [45] showed that the agreement with experimental data ranges from 6% to 10% when assessing the coefficient of lift, C_l. The general consensus [24] [36] [18] is that for angles of attack less than $\alpha = 10°$, Fluent is in good agreement with its corresponding experiments. These investigations also identified the turbulence model selection as the main source of the CFD-experiment discrepancy. For this reason,

---

[†] 1.10=Leading Edge Radius Parameter, 40 = location of t/c in percent chord, and 1.051 = Trailing Edge Parameter

ANSYS Fluent 14.0 was not validated as a solver in this investigation, and only the turbulence model selection was carefully reviewed.

4.3 Solver methodology

Fluent 14.0 was employed in the Reynolds Averaged Navier-Stokes (RANS) mode. This solver uses a control volume based technique to convert a general scalar transport equation to an algebraic equation that can be solved numerically [33]. Due to the low Mach number of the landing configuration of the CP-140 ($Ma = 0.24$), the pressure based method was used to solve the incompressible continuity (Eq 4.1) and momentum (Eq 4.2) equations.

$$\nabla \cdot V = 0 \tag{4.1}$$

$$\rho(\frac{\partial V}{\partial t} + V \cdot \nabla V) = -\nabla P + \mu \nabla^2 V + f \tag{4.2}$$

Where:
V = velocity vector
ρ = density
P = pressure
f = other body forces

This results in difficult convergence unless a suitable pressure-velocity coupling algorithm is used. Fluent was used in its uncoupled mode, which means that each equation was solved individually. Pressure-velocity coupling was achieved using the pressure-based segregated Semi-Implicit Method for Pressure-Linked Equations-Consistent (SIMPLE-C) algorithm, which indeed has proven to accelerate convergence in this study. The pressure gradient was discretized using the least squares cell based method, a standard pressure discretization and a second order upwind scheme were used for momentum and modified viscosity discretization. Higher-order term relaxation, Numerical Diffusion, was also utilized in order to reduce the fluctuations of the residuals; the higher order coefficient relaxation was set to 10^{-7} for all variables.

4.4 Turbulence model selection

Since it has been shown that the choice of turbulence model could be a source of error, much care was taken in this aspect of this work. In order to quantify the effect of the turbulence model, the 2D steady state solution was computed using three different turbulence models, namely, the Spalart-Allmaras (SA), the Shear-Stress Transport (SST), and the Reynolds Stress Transport (RSM). The initial conditions were set to a uniform flow-field corresponding to the inflow conditions. These conditions were the starting point for computations using the SA turbulence model. Once a converged solution was obtained, the computation was repeated using the SST turbulence model first, and then followed by the RSM turbulence model. Hence, the converged solution of the SA turbulence model computation was used as the initial conditions for the computations employing the SST and RSM turbulence models in an effort to accelerate convergence.

4.5 Boundary conditions

Standard boundary conditions appropriate for a 2D steady computation analysis were used for all configurations. Since Fluent is a finite volume based solver, a 2D analysis was achieved with a domain depth of one cell. Subsequently, symmetry boundary conditions were applied to the spanwise faces thereby simulating an infinite wing. The wing as well as the flap were defined as stationary walls with no slip condition, and the domain outlet was defined as a pressure outlet. The reported stall speed of the P-3 Orion was 133 knots ($68.42m/s$)[2], hence the free stream velocity, U_∞, at the inlet was set to $U_\infty = 1.2V_{stall} = 82m/s$ ($Ma = 0.24$) at $\alpha = 0°$ with a turbulence intensity specified at the domain inlet as $Tu = 10\%$. At these conditions, the computed lift coefficient, C_l, for the landing configuration was 2.37. Since these simulations were executed months ahead of the experimental campaign, the turbulence intensity level within the wind tunnel was not known, and the $Tu = 10\%$ was selected arbitrarily. This turbulence level at the inlet resulted in a $Tu \approx 1\%$ at the wing LE. Atmospheric pressure was specified at the velocity inlet as standard atmospheric ($P = 101.325kPa$), and laminar to turbulent transition was not specified anywhere in the domain.

4.6 Mesh Methodology

The mesh or grid is the method of discretizing the physical domain of the problem. All grids in this investigation were constructed using the mesh generation software *Pointwise*®. According to Murayama et al [57], while the generation of a structured versus unstructured grid is more time consuming, the solution of a structured grid is considerably more economical. Due to the large number of cases comprising this investigation, and consequently the considerable amount of computational time required, a structured mesh was chosen.

A C-Grid topology was selected in order to better accommodate the complex geometry, mesh point distribution, and cell diffusion of the problem at hand. The domain boundary was placed 50 chord lengths away from the airfoil surface in every direction in accordance with Murayama and Yamamoto [60], who determined this to be the minimum acceptable domain size capable of producing accurate flow predictions. The boundary layer around the airfoil was fully resolved in the solution grid with a $y^+ = 0.75$ at the wing and flap surfaces. The y^+ parameter was derived from the law of the wall [87], and represents the dimensionless wall distance that was normalized with the friction velocity and the local kinematic viscosity. The increased grid density within 2 chord lengths suggested by Murayama and Yamamoto [60] for accurate drag prediction was not adhered to due to the significant increase in computation time that it would require. A maximum cell growth rate of 1.1 was employed within the boundary layer, and a maximum growth rate of 1.2 was utilized in the remainder of the domain as recommended by Piomelli [66]. Figure 4.1 illustrates the solution mesh generated for the clean configuration. The domain size approximately 450 x 450m^2, while the wing chord was 4.526m in length.

For the numerous landing configuration cases, the mesh construction method was carefully considered. Since both the flap gap and overlap were varied in increments of $0.01c_w$ up to a maximum increase of $0.04c_w$; 25 distinct landing configurations were needed. In an effort to minimize the mesh generation time, the dynamic mesh function of Fluent was employed. For further detail, refer to the Landing configuration mesh generation Section 4.8.1 on page 38.

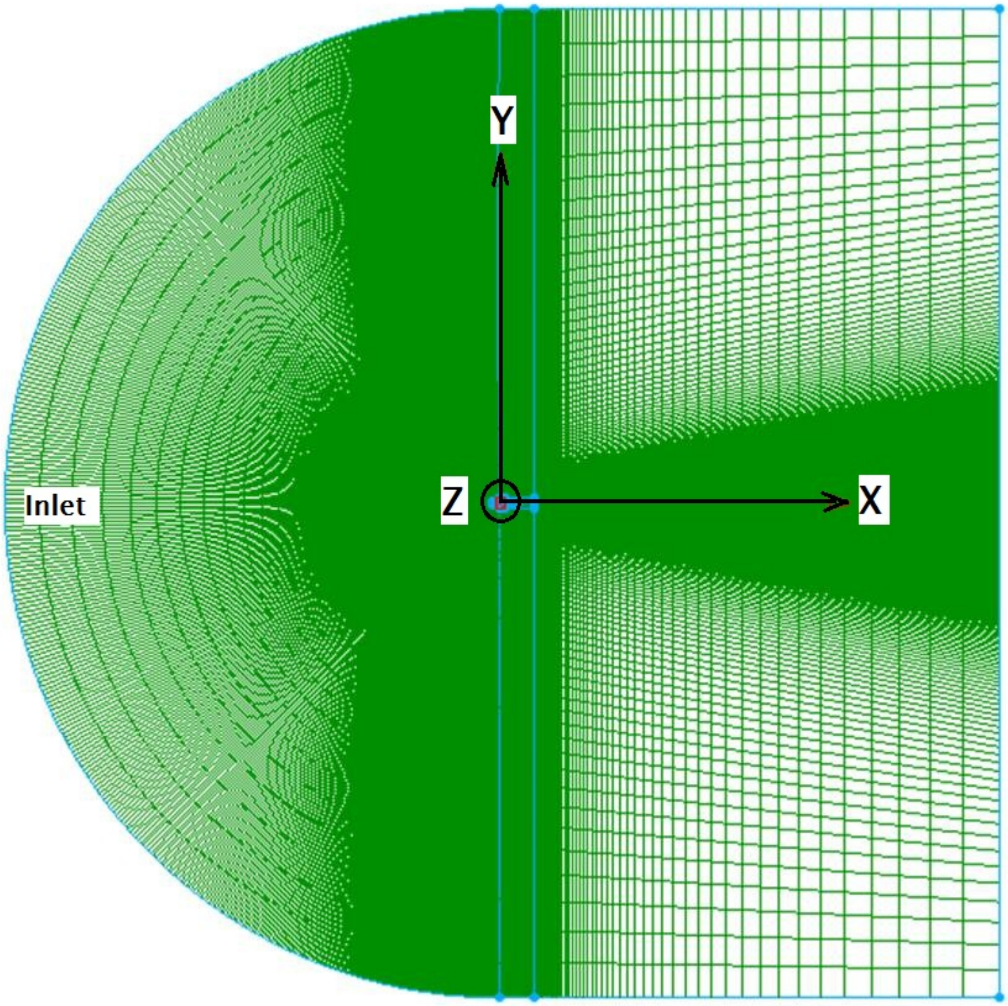

Figure 4.1: Clean Configuration - fine mesh

Two HP Z800 workstations containing 2 Intel(R) Xeon(R) X5650 processors each, were available for the duration of the investigation. Additional computers were utilized in an effort to solve multiple cases simultaneously. These additional computers were HP Compaq 6005 machines equipped with AMD Phenom (tm) II X4B95 processors.

4.7 Clean Configuration

4.7.1 Grid Generation

The clean configuration consisted of the wing with the Fowler flap nested in the flap cove. Considerable effort was devoted to validating the mesh using grid convergence studies. First, a coarse mesh was generated by distributing 370 mesh points along the airfoil and 170 mesh points along the trailing edge with a $y^+ = 2$. Subsequent meshes were generated by increasing the mesh density by 40% each time, and by increasing the boundary layer resolution to $y^+ = 1$ and $y^+ = 0.75$ respectively. Figures 4.2, 4.3, and 4.4 illustrate the mesh density progression for the clean configuration. The number of total points in each grid was: coarse = 0.36 x 10^6, medium = 0.48 x 10^6, and fine = 0.69 x 10^6. Figures 4.5 and 4.6 illustrate the details of the fine mesh.

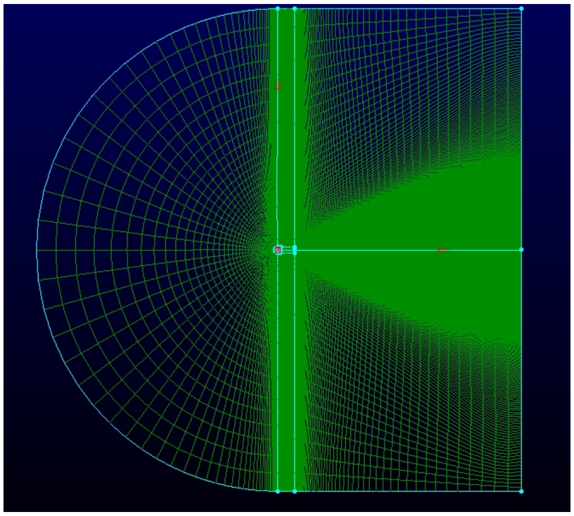

Figure 4.2: Clean configuration coarse mesh

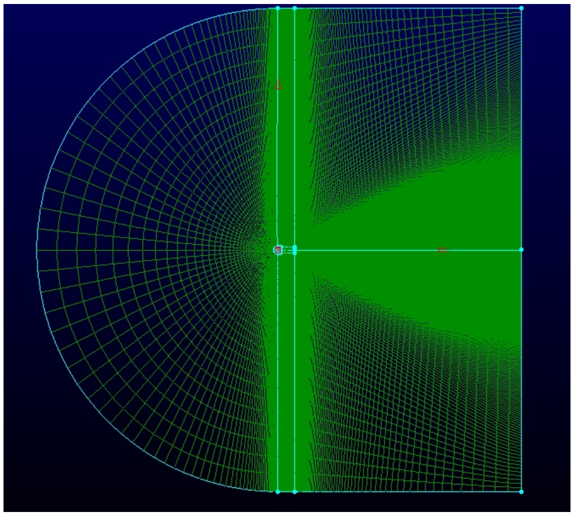

Figure 4.3: Clean configuration medium mesh

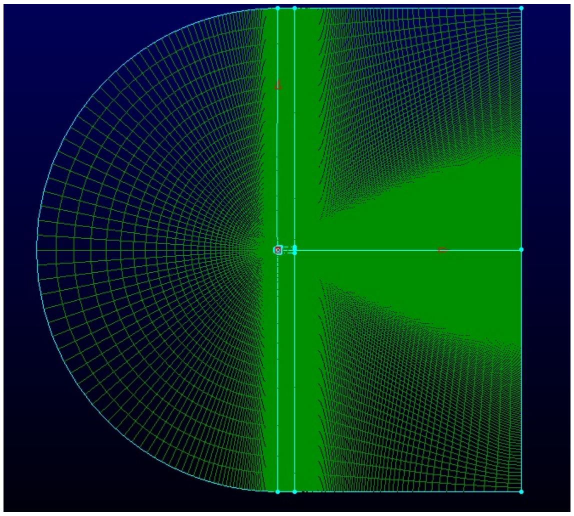

Figure 4.4: Clean configuration fine mesh

It is important to note that flow through the gap between the main wing and the Fowler flap was not modelled in the clean configuration, although its outline can be seen in Figure 4.5. Several attempts were made to model the flow through this slot in the clean configuration, however due to the sharp geometry near the front of the flap cove on the lower surface of the wing a sufficiently converged solution remained elusive. Furthermore, since the flow through this clean configuration slot was minimal, its effect on aerodynamic performance was consequently negligible.

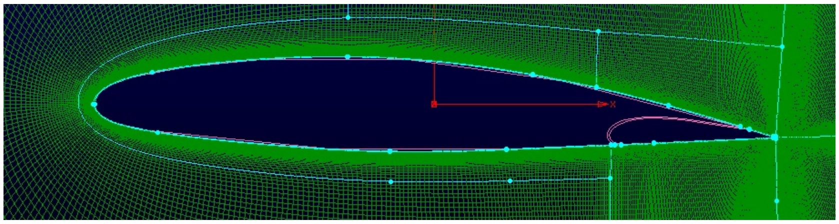

Figure 4.5: Clean configuration boundary layer mesh

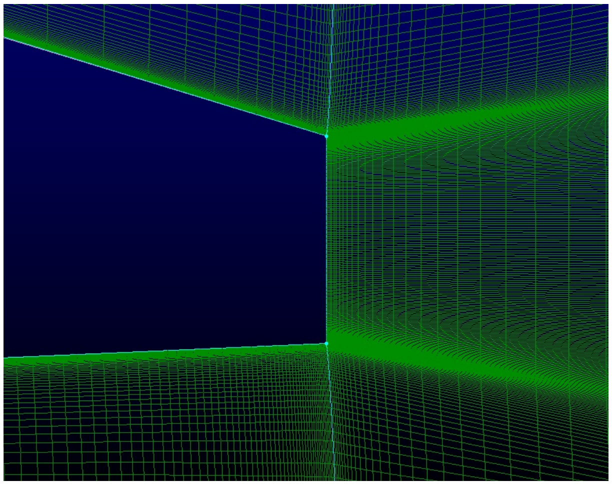

Figure 4.6: Clean configuration trailing edge mesh

4.7.2 Solution Convergence

In Fluent, the scaled residuals are computed as follows; the conservation equation for a general variable ϕ at cell P is:

$$a_P\phi_P = \sum_{nb} a_{nb}\phi_{nb} + b \tag{4.3}$$

Where:

a_p = centre coefficient and is computed as:

$$a_P = \sum_{nb} a_{nb} - S_P \tag{4.4}$$

a_{nb} = influence coefficients of neighbouring cells

b = contribution of the constant part of the source term S_c in S = $S_c + S_P\phi$

Hence, the unscaled residual (R^{ϕ}) is computed as:

$$R^{\phi} = \sum_{cellsP} \mid \sum_{nb} a_{nb}\phi_{nb} + b - a_P\phi_P \mid \tag{4.5}$$

and the scaled residual is obtained as:

$$R^{\phi} = \frac{\sum_{cellsP} \mid \sum_{nb} a_{nb}\phi_{nb} + b - a_P\phi_P \mid}{\sum_{cellsP} \mid a_P\phi_P \mid} \tag{4.6}$$

The convergence of the clean configuration solution was determined by the magnitude of the scaled residuals. A residual threshold of less than 10^{-6} was deemed sufficient for the continuity, x-velocity and y-velocity residuals for all three turbulence models.

4.7.3 Grid Convergence

A grid convergence study scrutinized the profiles of velocities U, velocity V, pressure P, and the friction coefficient C_f at the 10 stations illustrated in Figure 4.7. An example of the grid convergence analysis illustrating velocity U at the location of maximum t/c is illustrated in Figure 4.8.

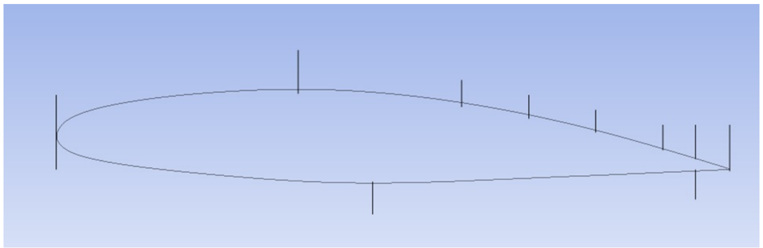

Figure 4.7: Grid convergence test stations

Velocity U was the velocity in the local x-direction, U_e represented the external velocity in the local x-direction outside the BL, and velocity V was the velocity in the local y-direction. First, the average velocity and pressure of each profile at each station was evaluated with a grid convergence criterion of $< 2\%$ variation. Next, a comparison of the maximum velocity and pressure magnitudes followed at each station. For the SA solution, the maximum variation with respect to the fine grid

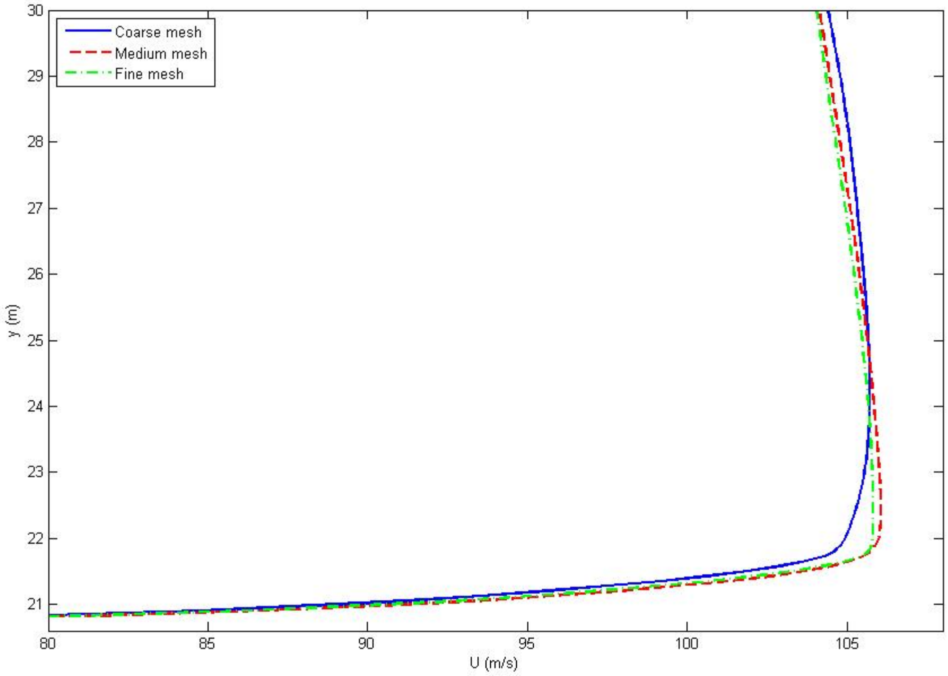

Figure 4.8: Grid convergence using velocity U at location of maximum t/c

found in the velocity and pressure maxima between the medium and fine grids were: $\Delta U_{max} = 0.4\%$, $\Delta V_{max} = 0.1\%$, and $\Delta P_{max} = 0.99\%$. The friction coefficients were completely converged. The lift coefficient, C_l, for the wing section was also monitored for convergence, and the variation in C_l between the grids, using the SA turbulence model, was $\Delta C_l = 1.4\%$.

4.7.4 Clean configuration solution

Due to the grid quality ($y^+ = 0.75$), it was possible to compare the simulations to the law of the wall, which deals with the laminar sub-layer and turbulent region of a 2D boundary layer. Figure 4.9 compares the simulated results to the law of the wall at $0.70c_w$. It shows that, while all three turbulence models approximate the law of the wall quite closely, the SA turbulence is the closest simulation. The von Kármán constant used was $\kappa = 0.41$ as generally accepted for this type of flow [87]. Considering that the SA turbulence model was specifically designed for aeronautical flows, this conclusion was not unexpected.

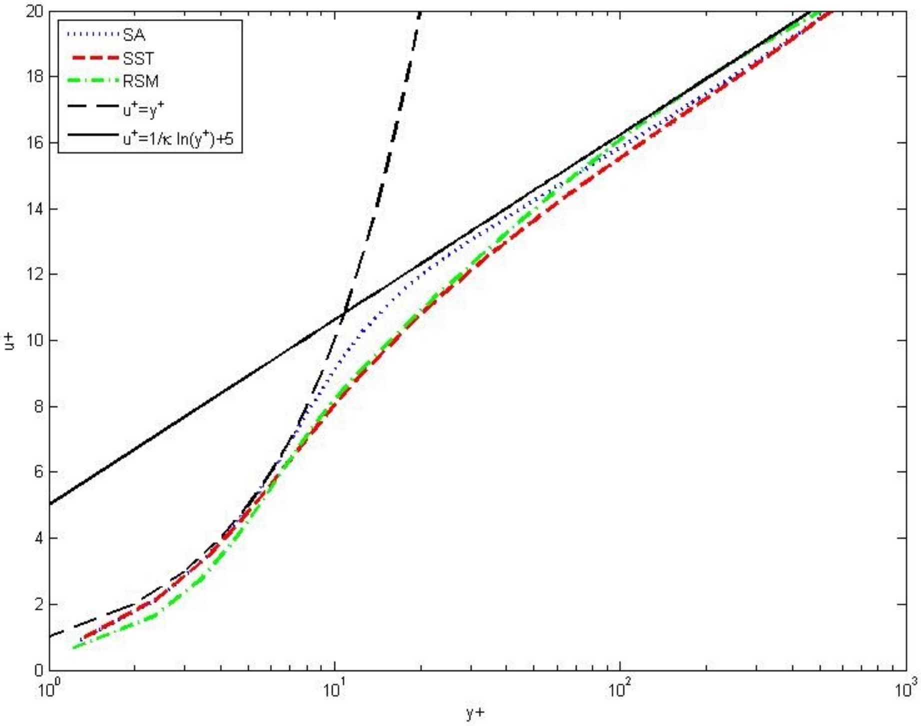

Figure 4.9: Law of the wall verification, clean configuration at $0.70c_w$, $Re = 24 \times 10^6$

Table 4.1 summarizes the lift coefficients, C_l, computed for the clean configuration using all three turbulence models. Figure 4.10 illustrates the same lift coefficients graphically.

Table 4.1: C_l values for different Tu models - clean configurations

Angle of Attack	SA	SST	RSM
0°	0.58	0.56	0.56
5°	0.85	0.84	0.84
10°	1.08	1.07	1.06
12°	1.16	1.13	1.13
14°	1.21	1.15	1.19
16°	1.24	1.21	1.22
18°	1.25	1.23	1.23

As can be seen from Figure 4.10, the influence of the turbulence model on C_l was negligible. All three models investigated underestimated BL separation, thereby delaying stall to a much higher angle of attack as was confirmed by the present as well as the NRC experimental campaigns. The prediction of the separation location on the TE of the clean configuration will be discussed in Chapter 6.

4.8 Landing Configuration

4.8.1 Grid Generation

The landing configuration consisted of the flap deployed to a maximum deflection angle of 40°. Following the successful simulation of the clean configuration, a grid of identical domain dimensions and similar mesh density was constructed for the landing configuration. The G0-O0 (gap increase = $0c_w$, overlap increase = $0c_w$) landing configuration consists of the Fowler flap deployed to 40°, with a flap gap = 3.625" and overlap = -0.5". Each landing configuration was identified by the size of flap gap and overlap increase from this manufacturer specified position in increments of

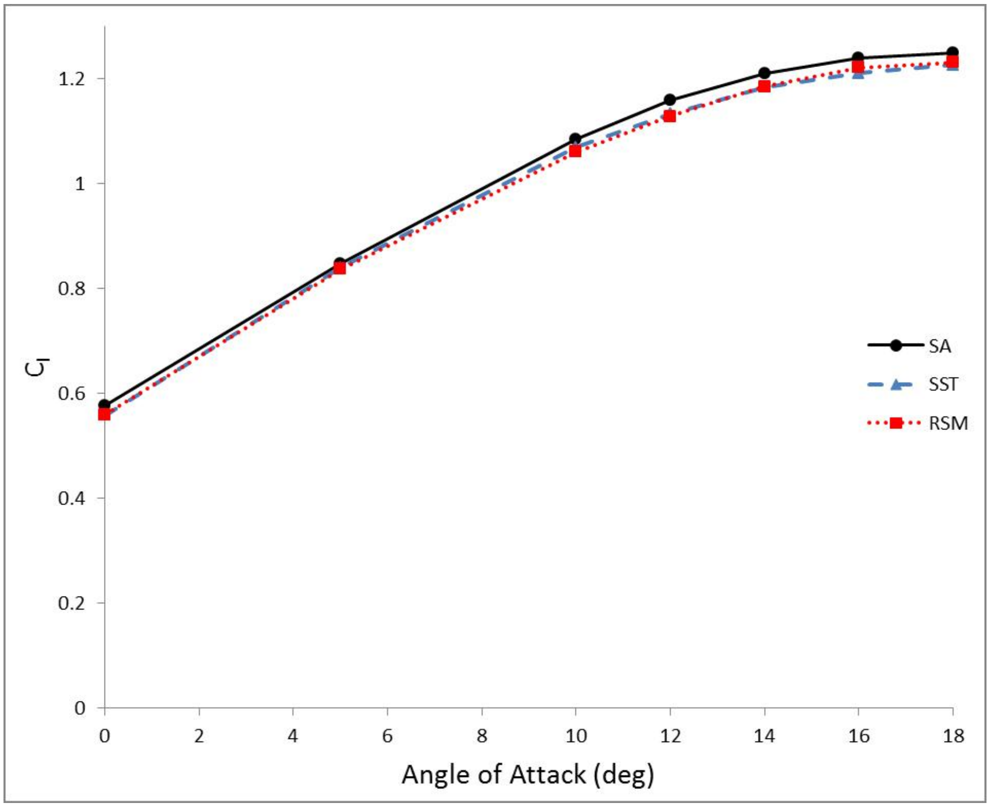

Figure 4.10: Clean configuration lift curves - variation between different turbulence models

percent wing chord (c_w).

Although the final goal was to employ the dynamic mesh function with multiple domains, a single domain mesh was first created for the purpose of grid convergence analysis. Using a similar grid convergence methodology as for the clean configuration, a grid convergence study was conducted using four meshes namely, coarse = 0.37 x 10^6 cells, medium = 0.56 x 10^6 cells, fine = 0.89 x 10^6 cells, and superfine = 1.28 x 10^6 cells. Having identified a grid of sufficient density, five more grids were then constructed for the purpose of mesh density distribution analysis. Considering the complex geometry, the effect of varying the mesh density in key locations was explored and compared. Finally, a multi-domain grid was constructed, and was then subjected to a further grid convergence study to identify any effects that domain segregation may have on the solution. Four multi-domain grids designed to accommodate the dynamic mesh function as well as the sliding mesh function in Fluent were thus constructed. The domain division effectively separated the flap from the wing, thereby allowing independent movement as illustrated in Figure 4.11. The grid along the interfacing domain boundary was designed to accommodate cell generation as illustrated in Figure 4.12. Using this grid configuration, the flap could then be moved independently of the main wing, thereby increasing the flap gap or overlap at will.

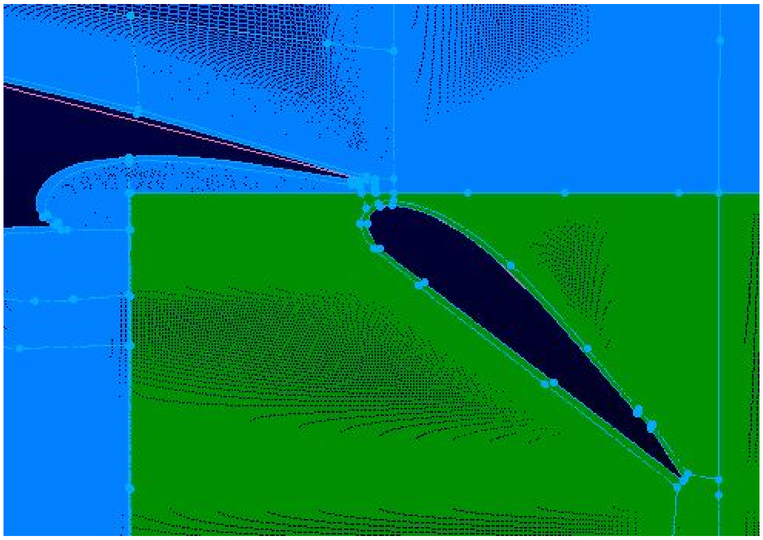

Figure 4.11: Solution multi-domain mesh

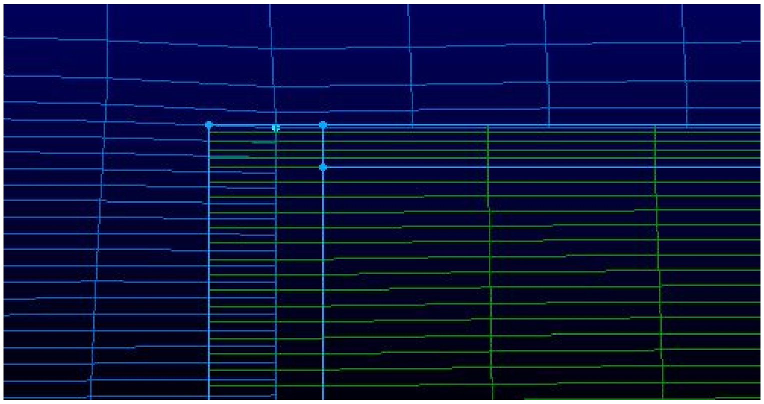

Figure 4.12: Solution multi-domain mesh

The three options for the dynamic mesh function in Fluent include smoothing, layering and re-meshing. Since the re-meshing and smoothing functions could only be used with an unstructured grid, only one option was suited to the problem at hand, the layering option. The layering function either generates new cells or deletes existing cells at a domain boundary, according to the speed and translation of the entire domain. When a mesh moves away from a domain boundary, the adjacent cell is stretched until it exceeds a user specified growth, at which point it splits in two cells. In the case of a mesh approaching a domain boundary, the cell is reduced in size until it again reaches a user specified reduction in width, and then is merged with the next adjacent cell. The layering function in this investigation was controlled so that a new layer was added at the top of the flap domain, thereby displacing the flap downwards, and whereby increasing the flap gap. Alternately, a new layer can also be added on the left side of the flap domain, thereby moving the flap aft and increasing the overlap. A UDF (User Defined Function) was written in C++ to control the speed and direction of the dynamic mesh movement, and was employed with the layering function so that each new layer of cells was of equal size to the preceding domain boundary layer. Due to the difference in cell width in the X and Y direction, as seen in Figure 4.12, 37 new layers were generated for every $0.01c_w$ increase in flap overlap (x-direction), while 363 new layers were generated for every $0.01c_w$ increase in flap gap (y-direction). The solution grid for the G0-O0 configuration contained 0.95 x 10^6 cells (1.9 x 10^6 points) while configuration G4-O4 contained 1.5 x 10^6 cells (3.5 x 10^6 points).

4.8.2 Solution Convergence

The convergence of the landing configuration solutions was considered at length. While the clean configuration solutions did not display any convergence instability, the landing configuration solutions displayed an exponential decay of the lift coefficient, C_l, drag coefficient, C_d and moment coefficient, C_m as illustrated in Figure 4.13. This exponential decay was exacerbated by increases in flap gap and overlap. While the scaled residuals were still monitored, the solution convergence was judged based on the convergence of C_l. The convergence criterion was the periodic oscillation amplitude of $C_l < \pm 0.01$, thus resulting in a relatively small solution uncertainty. For the example illustrated in Figure 4.13, the scaled residuals were as follows: continuity = 5.45 x

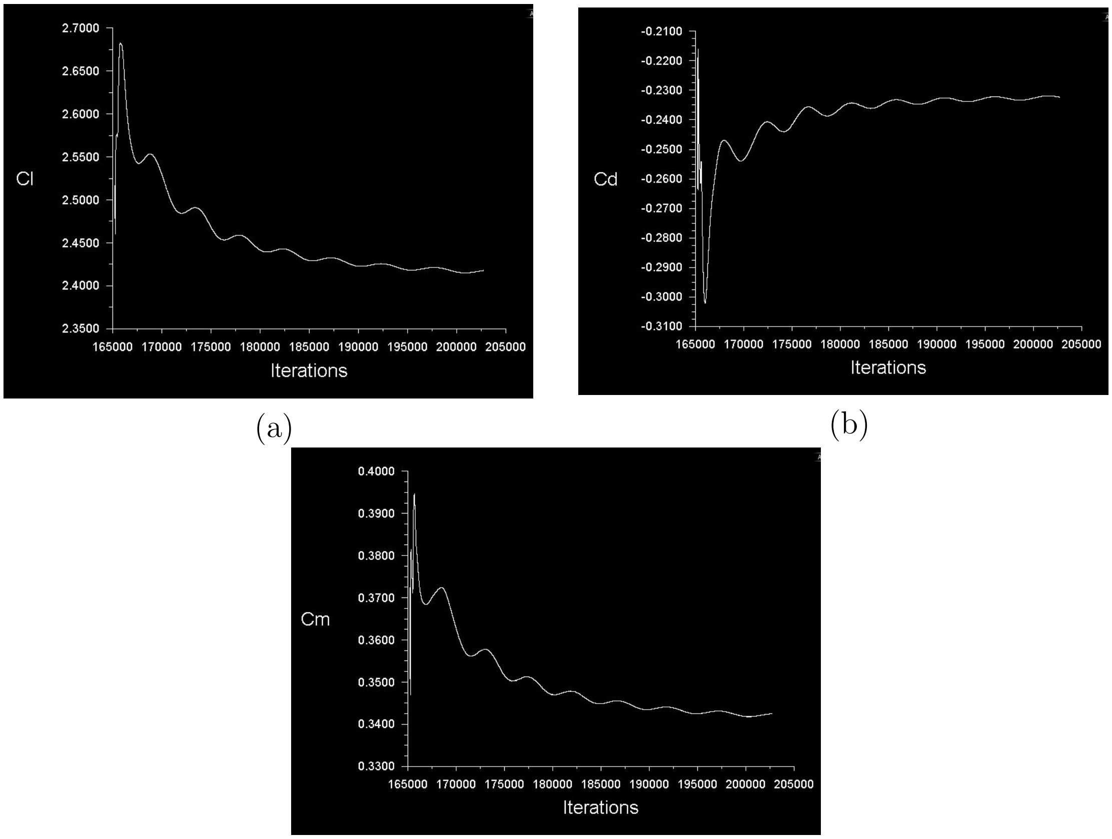

(a) (b)

(c)

Figure 4.13: Convergence history of coefficients of configuration G0-O0 $\alpha = 0^o$ (a) C_l, (b) C_d, (c) C_m about $0.25c_w$ positive indicates downward moment

10^{-5}, x-component of velocity = 7.49 x 10^{-8} and y-component of velocity = 4.65 x 10^{-8}.

It is important to note that due to the orientation of the coordinate system in Fluent, the moment coefficient, C_m, was defined as positive in the downward direction. As can also be seen in Figure 4.13, the computed C_d was inaccurate. This was most likely due to poor mesh density within the 2 chord lengths of the wing-flap configuration as discussed by Murayama and Yamamoto [60], which resulted in a negative drag coefficient. Accurate drag prediction using CFD is an ongoing challenge. The difficulties pertaining to the computational prediction drag were summarized by Rumsey and Ying [85].

4.8.3 Grid Convergence

The grid convergence of the landing configuration was investigated in detail. Figure 4.14 illustrates the locations used for analysing all G0-O0 solutions. As was discussed in the Grid Generation section, the grid convergence for the landing configuration (G0-O0) was first explored using a single domain grid. Employing the SA turbulence model, the maximum deviations between the fine and superfine meshes with respect to the superfine mesh were $\Delta U_{max} = 1.8\%$, $\Delta V_{max} = 0.2\%$, $\Delta C_l = 2.0\%$ and $\Delta C_d = 2.1\%$. Similar results were found using the RSM and SST turbulence models.

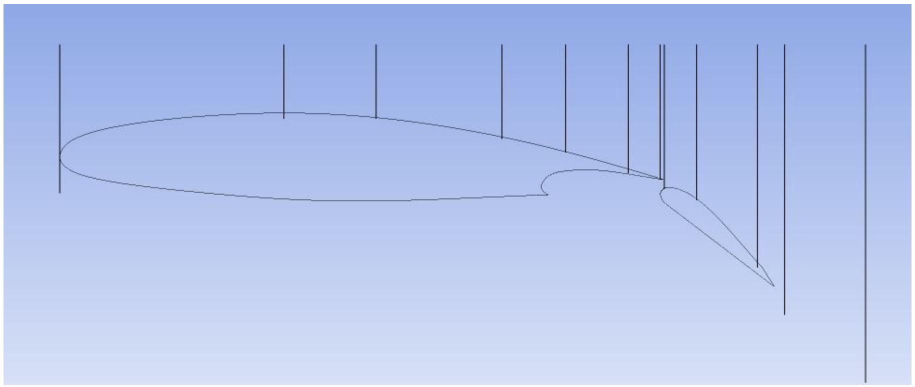

Figure 4.14: Landing configuration grid convergence test locations

Finally, four multi-domain grids were constructed. The ensuing grid convergence analysis no longer explored a large variation in the total number of cells, but instead focused on the cell distribution along the interfacing boundaries of the two domains. The domain interface was particularly important because of the automatic generation of new layers now involved. The number of cells along the domain interfaces would no longer match for all subsequent configurations. The sliding mesh function was employed to reconcile this challenge. The solution was found to be particularly sensitive to mesh density and cell distribution near the top left corner of the flap domain. A grid was modified until it was in close agreement with the superfine single domain grid investigated earlier. Details of the final, multi-domain solution grid can be seen in Figures 4.15 and 4.16.

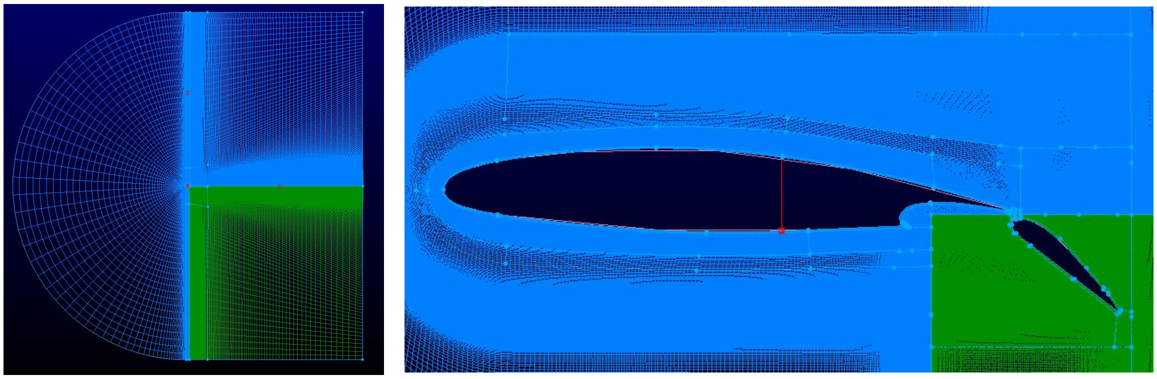

(a) (b)

Figure 4.15: Multi-domain solution mesh for configuration G0-O0 (a) Full domain (b) Landing configuration wing

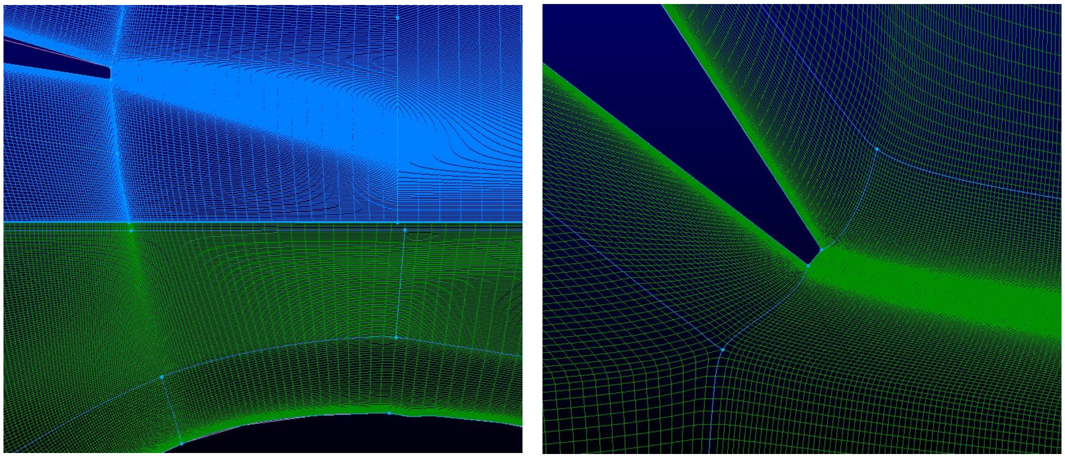

(a) (b)

Figure 4.16: Multi-domain solution mesh (a) Slot region (b) Flap TE

4.8.4 Landing configuration solutions

The G0-O0 landing configuration solution was first computed using the SA turbulence models at $\alpha = 0°$. Using the converged SA solution as the initial condition, the SST and RSM computations were then carried out. Next, the angle of attack was varied by adjusting the x and y components of the inlet velocity. The angles of attack investigated were $\alpha = 0°$, 5°, 8°, 10°, 12°, and 14°. Table 4.2 summarizes the lift coefficients computed for the G0-O0 landing configuration. Figure 4.17 illustrates the computed lift curves of the G0-O0 configuration employing the various turbulence models, and include the uncertainty of $\Delta C_l = \pm 0.01$ discussed earlier. The mesh

Table 4.2: C_l values for different Tu models - landing configurations

Angle of Attack	SA	SST	RSM
0°	2.37	2.45	2.43
5°	2.54	2.67	2.57
8°	2.56	2.76	2.57
10°	2.54	2.79	2.64
12°	2.50	2.78	2.62
14°	2.42	2.74	2.58

for each misaligned case was then generated using the dynamic mesh function in Fluent. Due to time restrictions and the considerable computational time required to reach convergence for the SST and RSM turbulence models, the vast majority of the misaligned configurations were solved using the SA turbulence model only. A small number of cases was solved using the SST turbulence model (G0-O2 and G0-O4) in order to verify that the difference between the turbulence models remains constant, and it was found that the difference was negligible as illustrated in Figure 4.18.

Table 4.3: Effect of gap and overlap on C_l (landing configuration, $\alpha = 0°$, SA)

	Overlap = 0	1	2	3	4
Gap = 0	2.37	2.27	1.94	1.69	1.53
1	2.29	2.02	1.86	1.63	1.49
2	1.93	1.85	1.75	1.62	1.47
3	1.76	1.70	1.62	1.53	1.45
4	1.63	1.60	1.53	1.48	1.45

Table 4.3 represents the test matrix devised for the CFD investigation of the landing configuration misalignment. All the variations listed in Table 4.3 were then investigated at all angles of attack listed in Table 4.2, resulting in a total of 150 configurations using the SA turbulence model alone. Due to the large number of configurations simulated, the use of the SST turbulence model, beyond the brief sensitivity analysis shown in Figure 4.18, was limited to the G0-O0 landing configurations. Due to the poor separation location prediction exhibited by the RSM turbulence model during

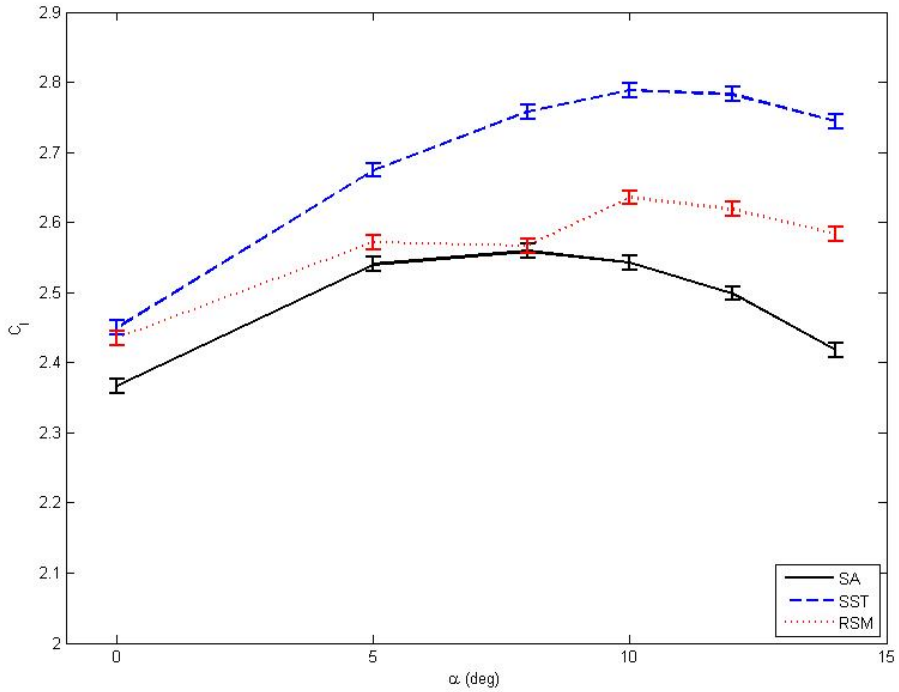

Figure 4.17: G0-O0 landing configuration lift curves

the clean configuration analysis, the RSM turbulence model was only employed for the G0-O0 configurations as well.

4.9 ‘A priori’ Landing Configuration

As will be discussed in Chapter 6, the landing configuration solutions without ‘a priori’ knowledge of the flow were not accurate. In an effort to correct this deficiency, the solution grid was modified to accommodate input from the user in order to ‘force’ the correct solution. The principal failure of the CFD solver was in computing the magnitude of the jet emanating from the flap slot. This information was obtained from the experimental results, and was subsequently incorporated into the simulation.

4.9.1 Grid Generation

The only objective of this revised mesh was the ability to control the slot flow. For that reason, the solution grid that was used to calculate the initial landing config-

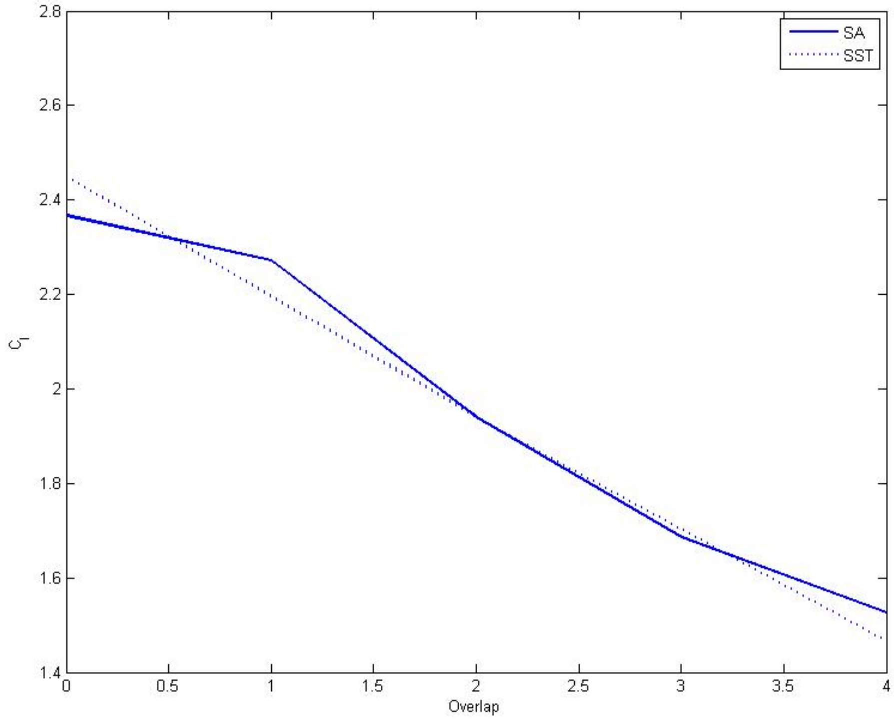

Figure 4.18: Comparison of C_l values calculate as a function of overlap variation using SA and SST turbulence models at $\alpha = 0°$, $\delta_{flap} = 40°$

uration solutions was subdivided into four domains as shown in Figure 4.19. This new mesh retained the versatility which was exploited earlier using the dynamic mesh function to increase the flap gap and overlap, and it enabled the user to insert a new boundary condition at the slot exit. Unfortunately, this mesh could only accommodate a variation in flap gap. The initial negative overlap resulted in an ideal location for this additional boundary condition. The variation in flap overlap however resulted in a discontinuity in the jet inlet boundary condition. As a result, the location and orientation of the jet boundary condition had to change, as the LE of the flap traversed farther downstream of the wing TE shroud. A grid accommodating variations in flap overlap was not completed.

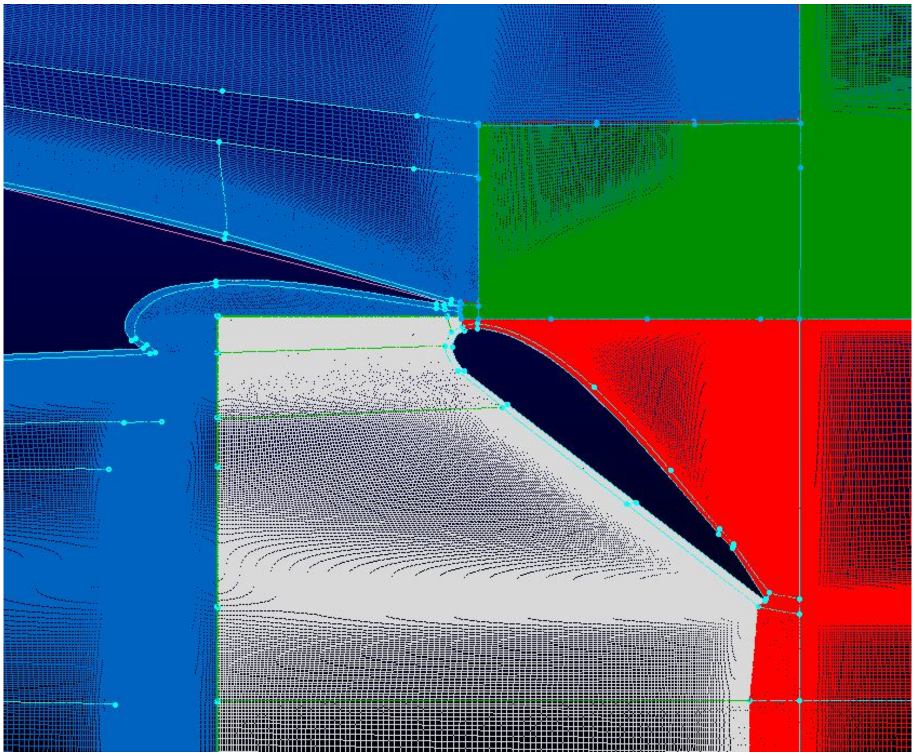

Figure 4.19: Four domain mesh

4.9.2 Solution Convergence

The solution convergence of the modified landing configuration grid was determined similar to the initial landing configuration simulations. The lift coefficient, C_l was observed until its oscillations decayed to $\Delta C_l = 0.01$.

4.9.3 'A priori' configuration solutions

Due to time constraints, only a limited number of 'a priori' configuration simulations were executed. The 'a priori' configurations were; G0-O0, G1-O0 and G2-O0. Qualitatively, the 'a priori' CFD results are in much closer agreement with the experimental results as illustrated in Figures 4.20, 4.21, 4.22, and 4.23. A quantitative analysis will be discussed in Chapter 6.

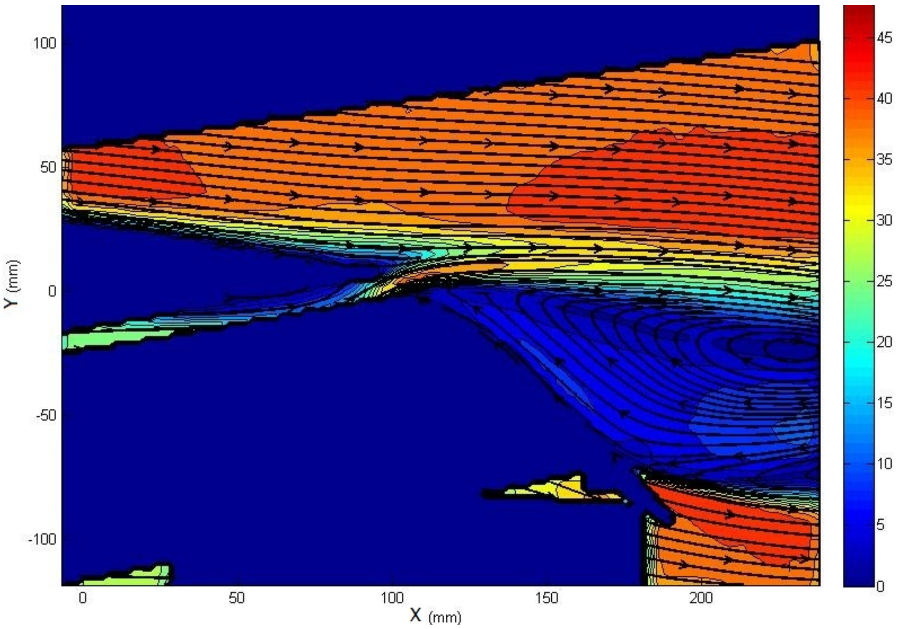

Figure 4.20: G0-O0 configuration velocity contours with streamlines, $\alpha = 0^\circ$ (PIV)

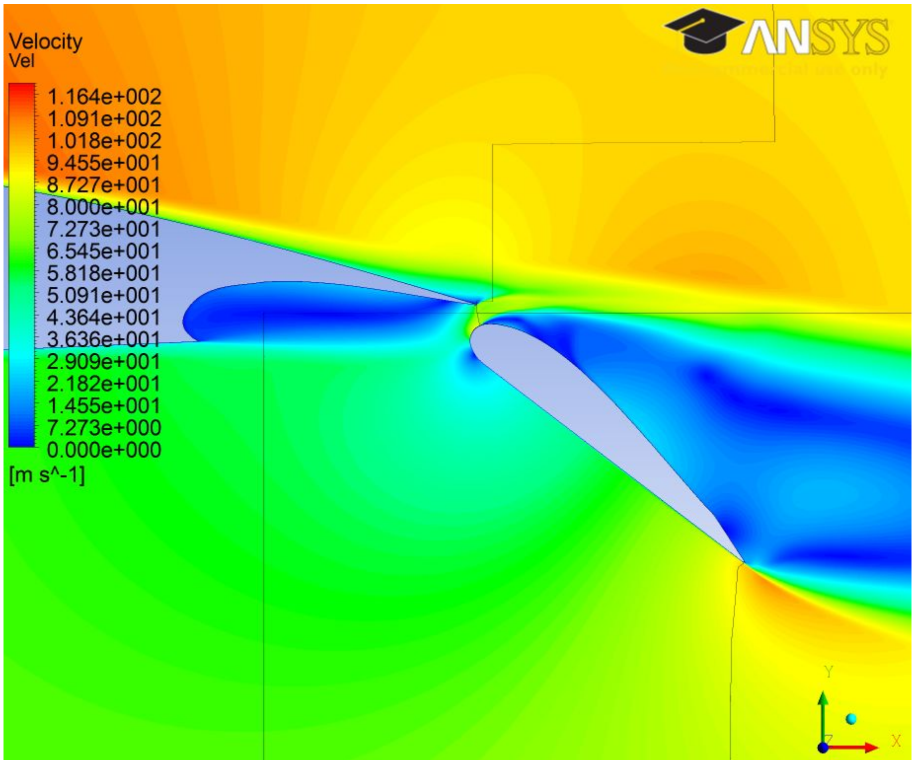

Figure 4.21: G0-O0 'a priori' configuration velocity contours, $\alpha = 0^\circ$ (CFD - SA)

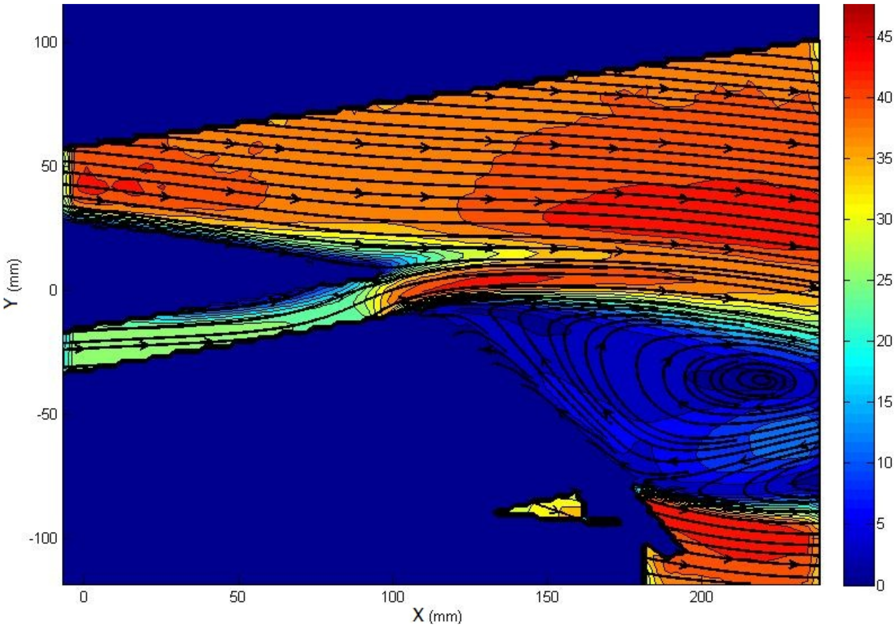

Figure 4.22: G2-O0 configuration velocity contours with streamlines, $\alpha = 0°$ (PIV)

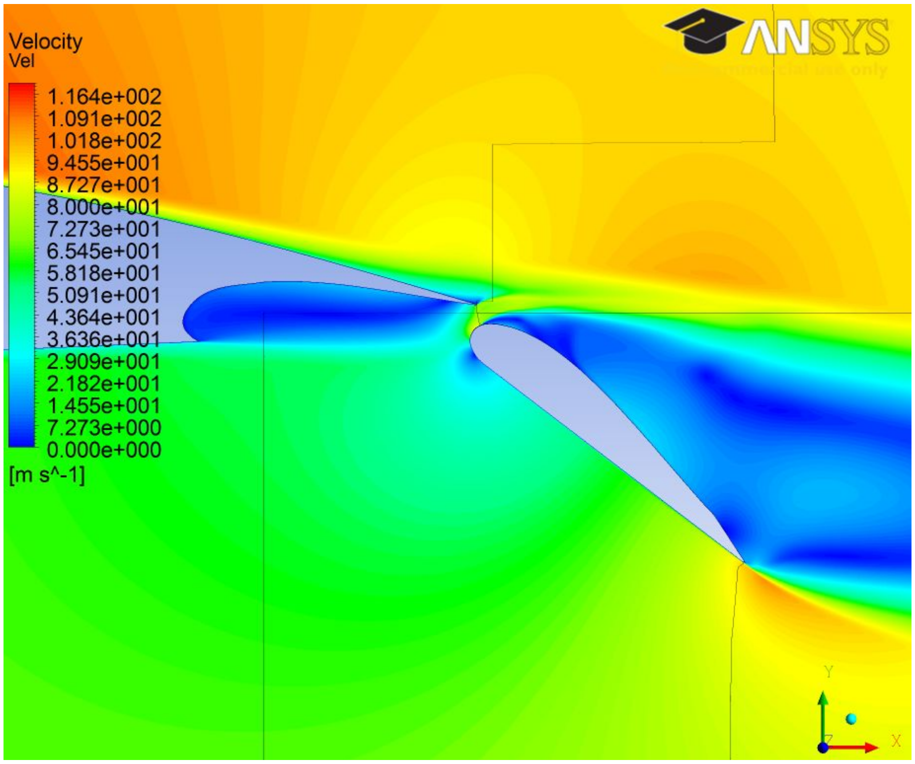

Figure 4.23: G2-O0 'a priori' configuration velocity contours, $\alpha = 0°$ (CFD - SA)

Chapter 5

Experimental Investigation

The experimental investigation consisted of two distinct parts. First, hot-wire measurements were performed for the purpose of flow similarity, and the second part consisted of PIV measurements of the flow as the flap gap and flap overlap were varied.

5.1 Similarity Study

In order to reconcile the large difference between the flight Reynolds Number ($Re = 24$ x 10^6) and the Reynolds Number achievable in the wind tunnel ($Re = 1.0$ x 10^6), the boundary layer (BL) developing on the main wing in the wind tunnel was tripped with a variety of tripping wires of different gauges. Based on the correlation between local Reynolds Number and the friction coefficient provided in White [29], it was determined that the tripping wire diameter required was approximately $2.0mm$. The tripping wire size was selected such that the BL shape factor ($H = \delta^*/\theta$) would be as close as possible to the flight $H = 1.45$ at the $x/c_w = 0.7$ location(as estimated in the CFD study), where the BL was fully attached.

For the preliminary experiment the model consisted of the 2D clean wing configuration (flap nested in the flap cove). The model and supports were designed so that the model could be installed in the 16" x 16" RMCC homogeneous flow wind tunnel shown in Figure 5.1. The model was allowed to rotate about the $0.25c_w$ location in order to adjust the angle of attack. The model which is illustrated in Figure 5.2 contained a chord of 16.5" and a span of 15.5" .

The model was manufactured by the RMCC Mechanical and Aerospace Engineering Department machine shop. The wing consisted of two aluminium end-plates with a foam core, both of which were subsequently enveloped in fibreglass, sanded and painted in order to produce smooth wing surfaces. Various gauge tripping wires

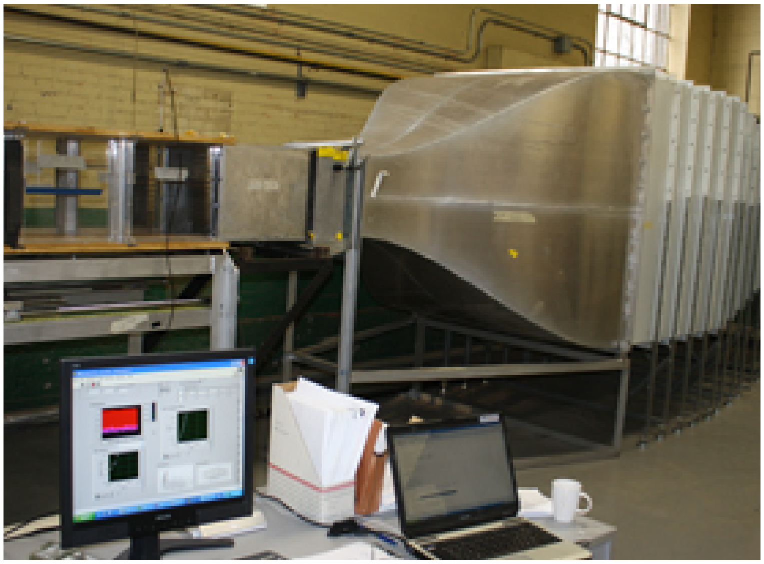

Figure 5.1: RMC Homogeneous Flow Wind Tunnel

Figure 5.2: Preliminary experiment model

were then attached at $0.05c_w$ from the leading edge.

The RMCC homogeneous flow wind tunnel consisted of a 16” x 16” cross section and can attain wind speeds up to $38m/s$. The wind tunnel is equipped with a $20Hp$ motor which drives a mixed flow fan made by the New York Blower Company; for further information relating to the wind tunnel specifications, see Fellouah et al [26]. A hot-film velocity transducer (Air Velocity Transducer Model 8455) manufactured by the TSC corporation was used to measure the free stream velocity. A four-channel (IFA 300 Constant Temperature) anemometer was employed in connection with an X-wire probe for flow quality test measurements and an L-shaped BL probe (Figure 5.3). Accurate horizontal alignment was achieved using a Cathetometer (The Precision Tool & Instrument Co Ltd).

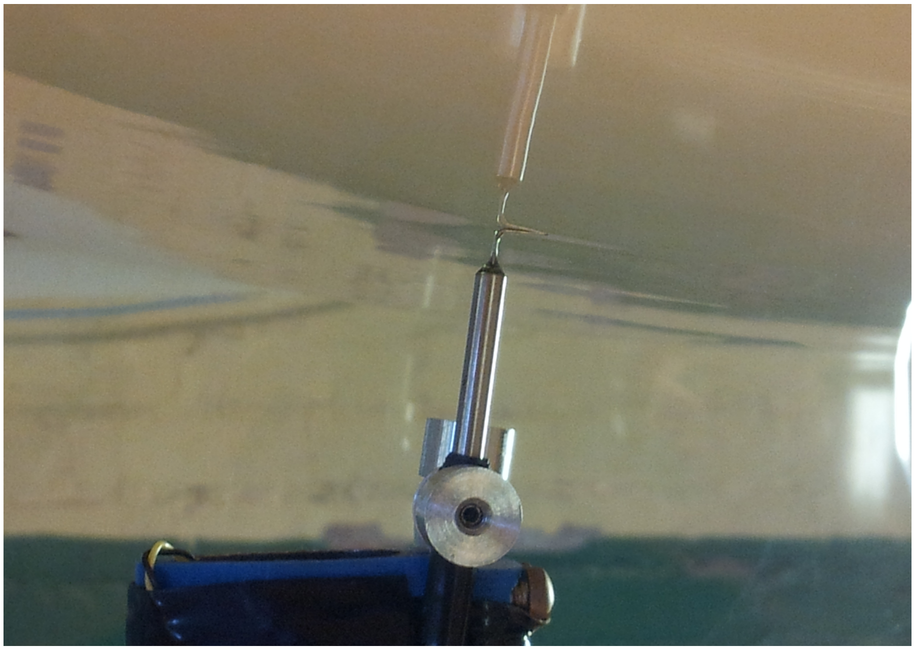

Figure 5.3: Boundary layer probe

The preliminary experiment started with a flow quality analysis using the X-wire probe. Following an initial calibration using King's Law, multiple freestream velocities were tested namely; $U_\infty = 25m/s$, $30m/s$, $35m/s$, $38m/s$ and $35m/s$ again. At the velocity of interest $U_\infty = 35m/s$, the flow quality test revealed a maximum turbulence intensity of $Tu = 0.3\%$ in the test section. The temperature rise during a single test did not exceed $0.1°C$, and the temperature rise over the full range of tests was $0.7°C$.

The BL profiles were measured at a zero angle of attack, perpendicular to the wing surface at the following locations: $0.42c_w$ [(t/c) location], $0.70c_w$ and $0.80c_w$. Measurements were averaged over approximately 26.2 seconds of data sampled at $5kHz$ at each point. The resolution of the first 0.5" of travel was 0.005" in the y-direction, with a subsequent decrease in resolution to 0.01" up to a total distance of 1.0". This distance was sufficient to reach a uniform U_e outside the BL in all cases. The BL probe was mounted on a thin profiled arm extending from an external traversing mechanism and aligned with the wing surface. The mechanism allowed traversing in the streamwise and vertical directions with a resolution of 0.127 mm.

Based on the theoretical tripping wire diameter of $2.0mm$ [29], three tripping wire configurations were selected: 1.60 mm diameter wire, 2.40 mm diameter wire, and $1.60mm$ & $2.40mm$ diameter wires combined. It quickly became evident that the $1.60mm$ diameter wire displayed insufficient change in the BL profile, hence this configuration was not considered in the test matrix. Consequently, BL profiles were measured for a baseline clean BL configuration, a single $2.40mm$ wire mounted at $0.05c_w$, and finally a $2.40mm$ wire mounted at $0.05c_w$ with an additional $1.60mm$ diameter wire mounted at $0.10c_w$ to overcome any potential flow relaminarization.

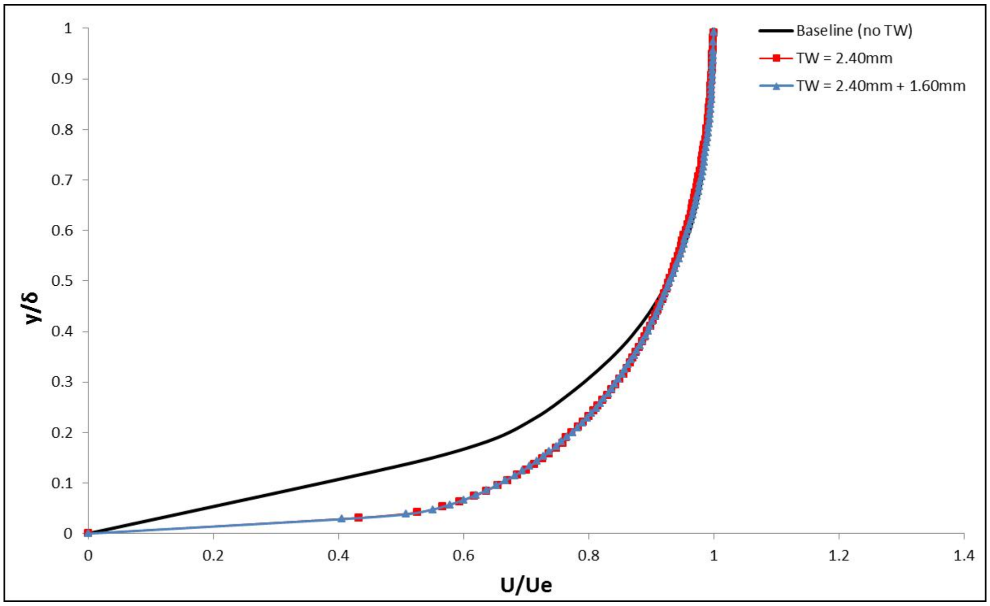

Figure 5.4: Boundary layer profiles at $x/c_w = 0.7$

The BL profiles obtained at $0.70c_w$ and $0.80c_w$ are displayed in Figures 5.4 and 5.5. It can be seen that for the Baseline (no TW) configuration at the $x/c_w = 0.8$ location, a fully separated BL was indicated by the shape parameter magnitude $H > 4$, which is typical of a turbulent separated BL. Table 5.1 summarizes the BL shape parameters obtained using both numerical and experimental methods at $x/c_w = 0.70$

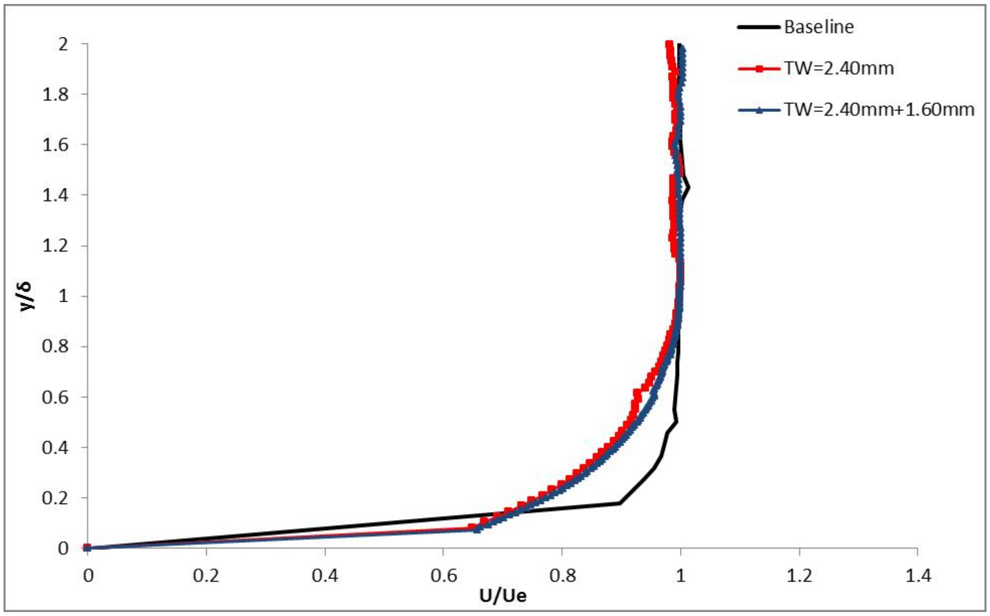

Figure 5.5: Boundary layer profiles at $x/c_w = 0.8$

and $x/c_w = 0.80$ for the given airfoil profile.

In an effort to maximize the number of correlations to compare, Head's Method was first used to estimate the BL progression over the wing profile. Due to the lack of velocity measurements available for this particular wing, NACA 0015 [closest (t/c) and airfoil profile available] velocity measurements ($Re = 9$ x 10^6) were used from Abbott and Doenhoff [3]. The transition from laminar to turbulent flow was estimated using two methods with similar results, namely, Wazzan's Method which yielded $x_{tr} = 0.10c_w$ and Michel's Methods $x_{tr} = 0.0375c_w$ [29]. Consequently, the transition location was set at $0.05c_w$. Based on these criteria, the BL momentum

Table 5.1: Clean configuration BL shape parameter obtained using various methods

	x/c=0.7	x/c=0.8
Head's Method	3.11	3.62
CFD SA	1.39	1.40
CFD SST	1.45	1.47
CFD RSM	1.48	1.53
Baseline (no TW)	2.36	4.83
TW=2.40mm	1.55	1.73
TW=2.40mm+1.60mm	1.55	1.72

thickness, θ, displacement thickness, δ^*, the friction coefficient, C_f, and shape parameter, H, were computed. The CFD generated H values were computed using a structured grid, employing the Spalart-Allmaras (SA), the Shear-Stress Transport (SST) and Reynolds Stress (RSM) turbulence models. The CFD simulations were conducted at the flight Reynolds number of 24 x 10^6 using the clean configuration at a zero angle of attack (see Chapter 4 for further details regarding the development of these simulations).

The difference between the effect of the single 2.40mm wire as opposed to the two wires combined was negligible. Consequently, the single 2.40mm diameter wire was selected to trip the BL at a location of $x/c_w = 0.05$ from the leading edge. Figure 5.6 illustrates the comparison between the tripped BL profile obtained using the hotwire measurements as well as the CFD generated profiles at the flight Reynolds number.

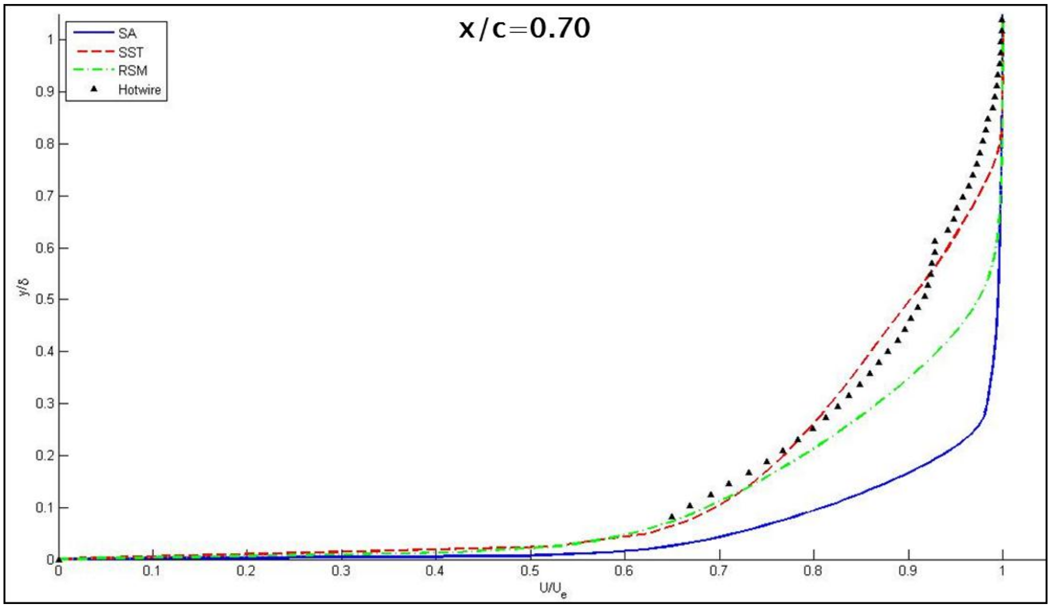

Figure 5.6: BL velocity profiles at x/c=0.7

5.2 Main Experiment

As it has been mentioned in Chapter 1, the objective of this work was to study the effects of the flap gap and overlap at various angles of attack on the flow field. As such, the experimental model was designed with a full span Fowler flap to ensure two dimensional flow over the entire configuration, while permitting independent variation of the flap gap, flap overlap, as well as angle of attack, α. The task consisted of investigating the clean configuration as a validation case, and the landing configuration (flap deflected to 40°) with specific geometric variations. The experimental rig was designed to fit into the S1 Wind Tunnel at Université de Sherbrooke 5.15. The model rig was designed to accommodate a 2D PIV system and a Scanivalve for data acquisition.

5.2.1 The Model

Since the flight Reynolds number of the CP-140 Aurora during landing is 24 x 10^6, it was essential to maximize the Reynolds number of the model by maximizing the wing chord, c_w.

Pope and Rae [70] recommended that the model chord should not exceed 40% of the test section height, and the model span should be 2.5 times smaller than the test section height. With a test section height of 4', the model chord, with the flap extended, was thus sized to 19" and the model span was sized to 19" as well. The resultant clean configuration, flap stowed, model chord was 16.5", which was also the model chord used in the preliminary experiment. The maximum angle of attack in the test matrix for the landing configuration was 12°. With the flap deflected to 40° (with respect to horizontal) and the flap gap and overlap at their maxima, the flow blockage was no more than 4%. Based on the model dimensions and a prescribed freestream velocity of $35 m/s$, the maximum Reynolds Number achievable for the landing configuration based on model chord was 1.03 x 10^6.

The sizing of the flap gap and overlap was considered at length. In an effort to replicate the flow character of the aircraft landing configuration, it was deemed that the flap gap and overlap should be sized using the BL momentum thickness, θ. This is a new approach, since traditionally the sizing of the flap gap and overlap was normalized by the wing chord [28] [108]. It was believed that this geometric approach to the model scaling is not accurate as it does not account for the flow dynamics. Since the goal of the wind tunnel experiment was to duplicate the flow character of the flight configuration, it was reasoned that the model sizing should be done with respect to a flow characteristic length. It was believed that the principal factor affecting the flow confluence of the wing wake and slot flow was the flow momentum emanating from the slot. The additional momentum originating from the slot flow thus determined the character of the flow confluence downstream of the flap slot. For this reason, the BL momentum thickness was selected as the scaling parameter. In comparison, if the flap gap and overlap were sized using the model chord, the resultant initial gap of the model would have been larger.

With the aid of the CFD simulations of the clean configuration, θ was computed at $x/c_w = 0.7$ employing the RSM turbulence model yielding $\theta_{RSM} = 12.26mm$. Then, using the θ obtained from the preliminary experiment at $x/c_w = 0.7$ of $\theta_{exp} = 1.04mm$, the reference flap gap spacing was sized to $7.9375mm = 0.3125$". The reference flap position refers to the flap gap within the manufacturer specified limits; gap = 3.625" and overlap = 0.5". This configuration was designated as G0-O0 (Gap variation = 0, Overlap variation = 0). Since the gap on the aircraft represents $0.02c_w$, this spacing was maintained for further gap and overlap variation. For example, the configuration designated as Gap = 2 and Overlap = 0 (G2-O0) refers to an increase in flap gap by $0.02c_w = 0.3125$" from the manufacturer specified location, while the manufacturer specified flap overlap spacing was maintained. Figure 5.7 illustrates the maximum flap gap (G4 = 0.625" increase beyond the manufacturer

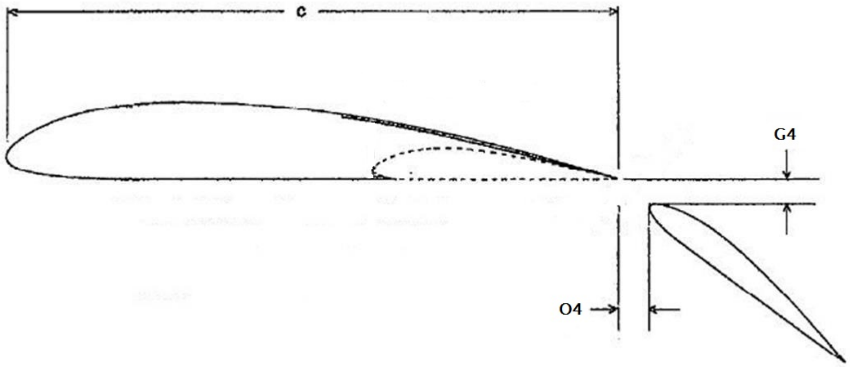

Figure 5.7: Fowler flap gap and overlap definition, both gap and overlap were increased by $0.04c_w$ beyond manufacturer specified limit

specified limit) and maximum flap overlap (O4 = 0.625" increase beyond the manufacturer specified limit).

Figure 5.8 illustrates the main experimental rig design. The final design consisted of two vertical aluminium plates with sharp leading edges to ensure undisturbed 2D flow within the experimental test section as shown in Figure 5.9. The two vertical plates were mounted on a solid aluminium plate to ensure correct alignment, while

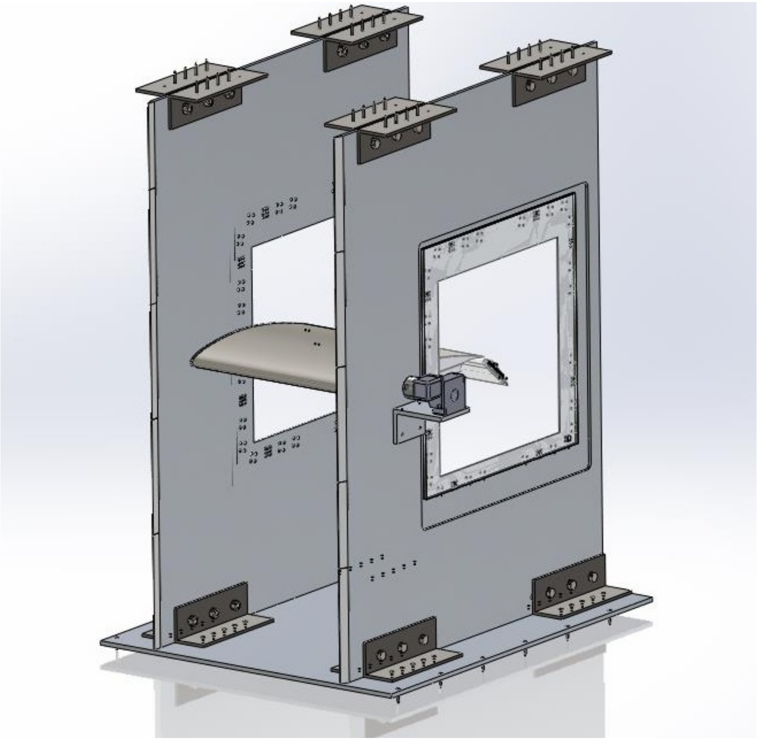

Figure 5.8: Experimental rig design

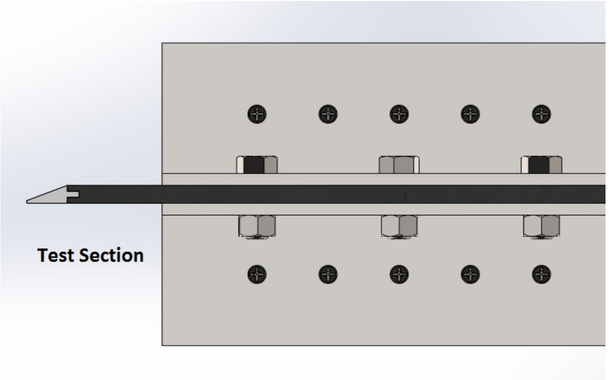

Figure 5.9: Left vertical plate leading edge

the entire frame fit into the wind tunnel test section (Figure 5.10).

Figure 5.10: Main experiment rig installed in the wind tunnel

To ensure sufficient visibility of the Fowler flap by the PIV camera, windows were cut out of the side plates as shown in Figures 5.11 and 5.12. A Velmex Model B5990TS rotary table and a stepper motor were incorporated for precise angle of attack positioning. The flap was also equipped with 17 pressure taps (Figure 5.13).

The design of the flap traversing system included the following design requirements. The system must enable independent variation of the flap gap and overlap, it shall accommodate both the clean configuration and the landing configuration, it must permit variations in angle of attack, and finally the model must present an unobstructed

Figure 5.11: PIV camera access window - external view

Figure 5.12: PIV camera access window - internal view

field of vision for the PIV camera. Foregoing the design of a complex flap traversing mechanism similar to that found on the aircraft, 22 specific test cases were identified, and a PMMA (Plexiglas) plate was then manufactured for each configuration. The flap gap and overlap variation was achieved by moving the entire Plexiglas plate using pre-drilled holes, as seen in Figure 5.11. Table 5.2 summarizes the experimental test

Figure 5.13: Stepper motor and Fowler flap pressure tubes

cases. Similar to the preliminary experiment, the main wing consisted of aluminium end plates and a foam core both of which were enveloped in Fibreglass, sanded and painted with matte black finish. The flap was manufactured using a 3D printer (ProJet 3000 HD made by 3D Systems) which allowed for precise integration of pressure taps along its upper surface (Figure 5.14). Due to the size of the wing span, the flap had to be printed in three separate sections. These sections were then individually fitted, sanded and painted with the same matte black paint. The sanding was professionally done by Perma Buff in Kingston Ontario. The S1 wind tunnel at Université de Sherbrooke shown in Figure 5.15 provided slots for wooden inserts that allowed the freestream velocity through the test section to increase. With the inserts in place, the maximum freestream velocity was approximately $43m/s$. A flow quality test of the wind tunnel was conducted using a Cobra Probe (Turbulent Flow Instrumentation, Australia). The transverse velocity profiles were constructed from data records of 17

Table 5.2: Experimental test matrix

Angle of Attack	Clean	Landing
0°	✓	G0-O0, G0-O2, G0-O4 G2-O0, G2-O2, G2-O4 G4-O0, G4-O2, G4O4
5°	✓	✘
10°	✓	G0-O0, G0-O4, G4-O0, G4-O4
12°	✓	G0-O0, G0-O4, G4-O0, G4-O4
14°	✓	✘

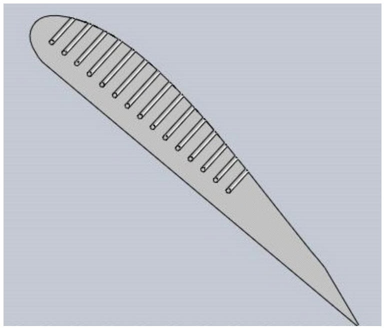

Figure 5.14: Flap pressure tap positions

Figure 5.15: S1 Wind Tunnel at Université de Sherbrooke [25]

seconds in length at a sampling frequency of 5kHz. The flow measurements revealed that with the inserts and the experimental model installed, the maximum turbulence intensity, $Tu = u_{rms}/U_{\infty}$), was 1.4%. During the experiment, the freestream velocity was gauged using a water manometer, while a temperature transducer was installed to measure the temperature downstream of the fan.

A Scanivalve (model ZOC 22B/32Px) was employed to record pressure measurements on the upper surface of the Fowler flap. For each run, 256 readings were averaged at a sampling frequency of 5Hz. In an effort to validate the two-dimensionality of the flow within the experimental test section, three pressure taps on the flap were aligned at the same x/c_w station in a spanwise direction.

The LaVision PIV system consisted of Imager ProX 4M camera, YAG Dual Cavity pulsed LASER, LaVision computer hardware with the associated 2D PIV software packages, as shown in Figures 5.16, 5.17, and 5.18. The Rocket (LVI 502 Fogger) smoke machine (Pea Soup Ltd., England) using Persistent Smoke Fluid A was found to be the best choice for seeding, due to the superior smoke particle persistence at the $35 m/s$ freestream velocity, as well as the consistent 0.2-0.3μm particle size. Data post-processing was completed using DaVis 7.2 software. In spite of the matte black paint covering the wing and flap surfaces, the high LASER intensity still resulted in significant scatter from the surface thus saturating the image and data with noise. For this reason, a Rhodamine 6g solution was applied to the wing and flap surfaces in order to shift the spectrum of the reflected LASER sheet such that it was subsequently filtered out by the camera. The PIV training and initial set-up was assisted by Dr Gray from the North American division of LaVision Inc.

5.2.2 Uncertainty

The uncertainty of the experimental results was investigated. The uncertainty of velocity vectors obtained from a PIV is an area of continued research. According to Grey [31], one of the ways to verify PIV results is to use hot wire anemometry in conjunction with the PIV system. Although hot wire anemometry was not employed in the S1 wind tunnel at Université de Sherbrooke, the pressure measurements obtained from the Scanivalve were used to evaluate the accuracy of the PIV system. It was found that the difference between the velocity recorded by the PIV and the velocity resulting from the pressure reading was less than 1.0%. As a result, a quantifiable measure of uncertainty for the PIV measurements was not computed.

The uncertainty of the Scanivalve measurement were ±0.15% [14], the uncertainty of the IFA 300 Constant Temperature Anemometer system employed during the pre-

Figure 5.16: PIV camera Imager ProX 4M

Figure 5.17: YAG Dual Cavity pulsed LASER

liminary experiment was 1% [20], and the air velocity transducer had an uncertainty of $\pm 0.5\% m/s$ [21]. The resulting uncertainties were too small to be visible on any of the plots and graphs produced.

Figure 5.18: The Rocket smoke machine

An attempt was made to calculate BL parameters from the PIV obtained data. However the physical uncertainty related to the camera resolution resulted in a considerable experimental error. While the velocity and TKE profiles were accurate for qualitative flow analysis involving BL separation, identification of maximum velocity vectors and related angles, higher order statistical data such as δ^*, θ and H could not be computed without a level of uncertainty that rendered the quantitative result meaningless. As a result, the BL shape parameters discussed in Chapter 6 were only to illustrate the relative development of the BL with respect to geometric configuration changes.

5.2.3 Data Acquisition

Given the lens and camera distance from the projected LASER beam, the measurement field formed an X - Y plane 247mm x 247mm in size with a resolution of 1.93mm. At first, 300 images were acquired at a frequency of 4.064Hz with a time between LASER pulses $dt = 13\mu s$. These images were then processed to generate an average velocity field, an instantaneous vorticity field, and an average Turbulent

Kinetic Energy (TKE) field. Due to poor seeding density, the first 20 images were ignored, and a convergence analysis was then performed. It was found that the percent change between the average velocity field comprised of 180 images versus 280 images was less than 1%, with the majority of change localized in the unsteady flap wake region. Consequently, 200 images were recorded for all subsequent experimental runs with the first 20 images being discarded.

The use of background noise subtraction was investigated in order to improve the fidelity of the experimental data, however it was found that with the use of the Rhodamine 6g solution, the background subtraction function eliminated significant amount of valid data. Hence this function was not employed.

Although the Scanivalve measurements were manually executed, the pressure data acquisition was simultaneous with the PIV velocity field data acquisition. Both measurement acquisition times were approximately 1 minute and 10 seconds.

Due to the type of motor-to-shaft coupler employed, a considerable amount of uncertainty resulted in the angle of attack determination. This unforeseen short coming of the model was rectified by installing the clean configuration at each angle of attack first. Due to the precise fit of the Fowler flap into the flap cove in the main wing, this ensured correct angle of attack alignment (Figure 5.19). The main wing was then fixed in its aligned position using the 1.25” securing nut, and then the landing configuration was installed. Most importantly, this initial oversight resulted in the data acquisition of some unplanned configurations. These configurations were later identified based on the measured flap gap and overlap.

5.2.4 Results

The PIV associated software, DaVis, was used to generate average Turbulent Kinetic Energy (TKE) data fields, average velocity data fields, instantaneous velocity flow fields, and instantaneous vorticity flow fields. The remainder of the data processing was executed using Matlab. Since only 2D data was acquired, the DaVis-generated TKE was calculated using Eq (5.1) [43], which assumes that the $\overline{ww}$ component of

Figure 5.19: Clean configuration at 5° angle of attack

TKE is the average of $\overline{uu}$ and $\overline{vv}$, and hence TKE would be approximated as:

$$TKE = \frac{1}{2}\overline{uu} + \frac{1}{2}\overline{vv} + \frac{1}{2}(\frac{\overline{uu}}{2} + \frac{\overline{vv}}{2}) = \frac{3}{4}(\overline{uu} + \overline{vv}) \tag{5.1}$$

Additionally, the term $\overline{ww}$ was evaluated based on the correlation of Liu [44] as:

$$\sqrt{\overline{ww}} = \sqrt{\overline{uu}} * \frac{\sqrt{\overline{vv}_{max}}}{\sqrt{\overline{uu}_{max}}} \tag{5.2}$$

In the case of the present experimental data, it was found that the difference between the two methods was no more than 1.6%. Consequently, the DaVis calculated data (Eq 5.1) was used for the remainder of the data analysis.

For processing purposes, the data field was segregated into three distinct regions: the main wing BL, the jet protruding from the flap slot during the landing configuration, and the flow over the deployed flap. Data analysis of each region will be discussed in Chapter 6. A sample velocity contour plot obtained for the reference landing configuration (G0-O0) is shown in Figure 5.20.

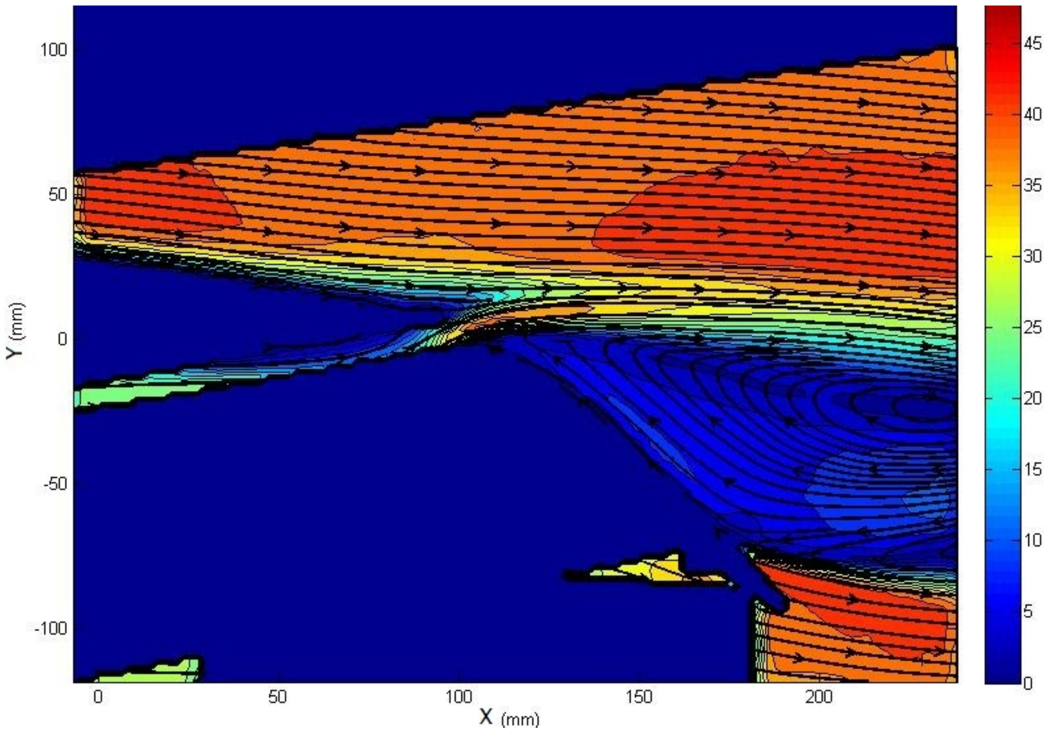

Figure 5.20: G0-O0 landing configuration at 0° angle of attack velocity contours and streamlines

Chapter 6

Results

The results from this work are presented in two distinct parts. The experimental results are presented first, followed by an in-depth analysis of the CFD results. For the purpose of the data presentation and analysis, two different coordinate systems were defined. The global coordinate system, X - Y, and the local coordinate system which was adjusted for local surface inclination x - y. Note that the Z axis in the global coordinate system is oriented according to the coordinate system used in Fluent, hence the Z axis is oriented coming out of the page. As a result, the moment about $0.25c_w$ is defined positive in the counter-clockwise direction (down). The two coordinate systems are defined in Figure 6.1.

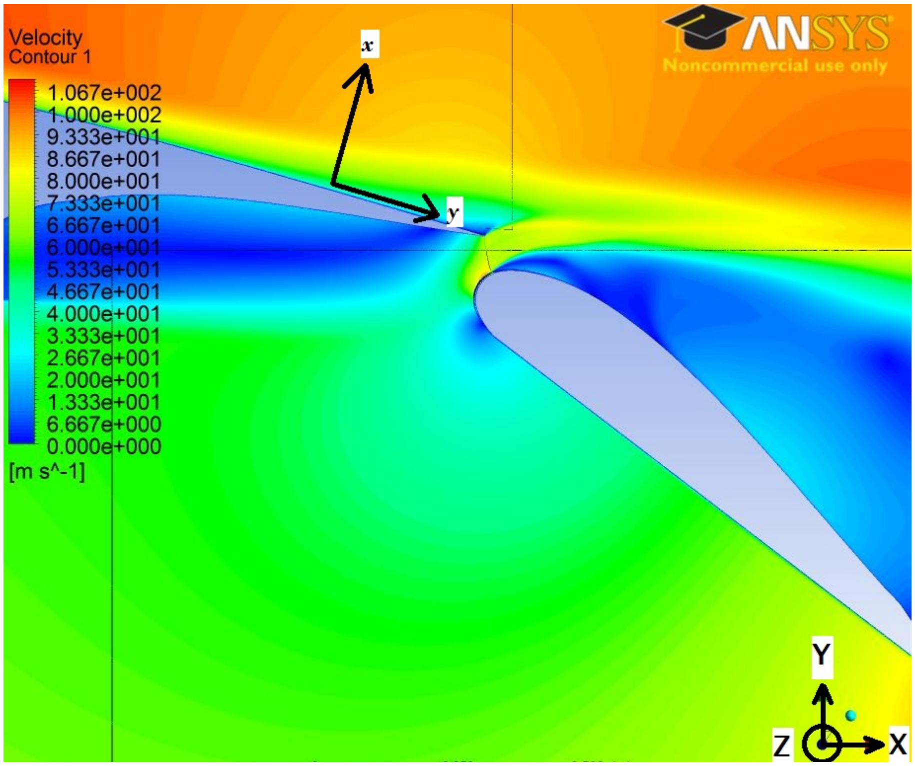

Figure 6.1: Definition of the coordinate systems used for flow analysis

6.1 Introduction

All PIV data was acquired on an X - Y plane of $247mm$ x $247mm$ in size with a resolution of $1.93mm$ in both the X and Y directions. Figure 6.2 is a typical data field acquired for the clean configuration at $\alpha = 0°$ illustrating the velocity contours with streamlines. The triangular region near the centre of the flow field represents the wing trailing edge (TE). The data in the top region of the flow field was excluded from analysis because the LASER intensity was low in that region which resulted in a large amount of noise and erroneous data.

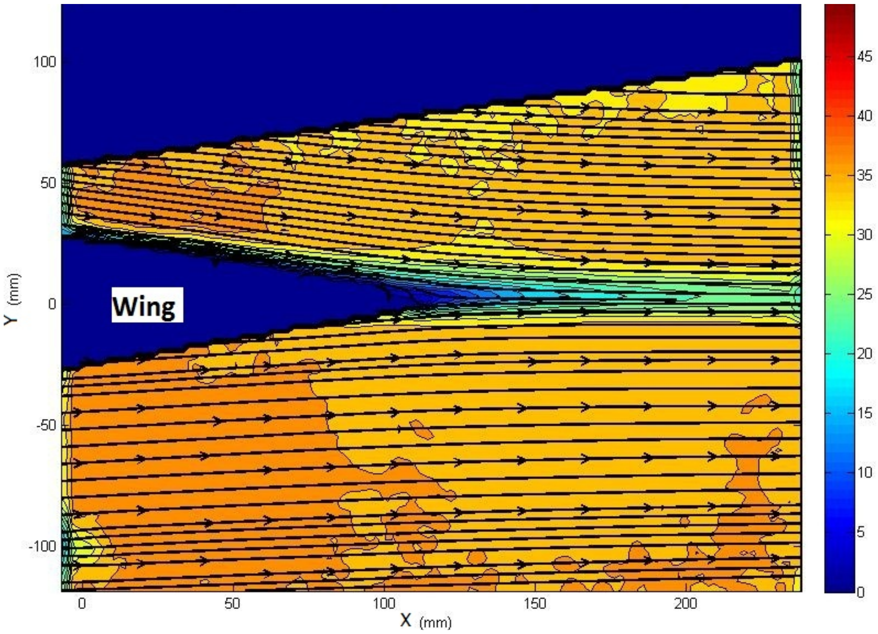

Figure 6.2: Velocity contours and streamlines of the clean configuration at $\alpha = 0°$ in m/s

6.2 Flow Validation

For a 2D PIV system, there is no flow metric such as the mass flow rate that would verify the validity of the statistically derived PIV data. In an effort to validate the PIV data obtained, an analysis was conducted of the clean configuration wing BL.

For the purpose of flow field validation, four locations were identified which are shown in Figure 6.3. The Reference location was located at the trailing edge of the wing, Stn(-1) is $5.8mm$ upstream from the Reference location at $x = 0.986c_w$, Stn(-2) is 11.6mm upstream from the Reference location at $x = 0.972c_w$, and finally Stn(-3) is located at $x = 0.90c_w$ (42.5mm upstream from the Reference location).

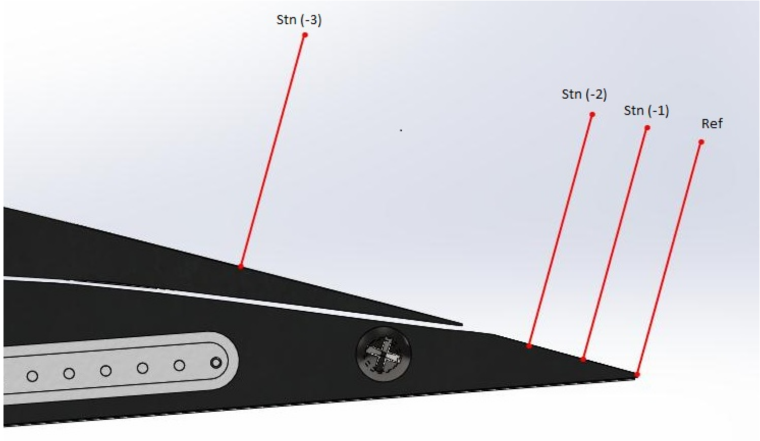

Figure 6.3: Boundary layer locations

Figures 6.4 and 6.5 illustrate the boundary layer velocity and turbulent kinetic energy (TKE) profiles at the four selected locations. All boundary layer profiles were adjusted for local surface orientation using interpolation.

The relatively poor data field resolution (ΔX = ΔY = 1.93mm) resulted in uncertainty in the exact location of the wing surface. For the purpose of the velocity and TKE profiles presented in this work, it was assumed that the first data point indicating a velocity $U \approx 0m/s$ occurred at the wing surface, and that the data point next to it that registered a non-zero velocity was the nearest data point to the wing surface (Figure 6.4). In fact the surface was located somewhere between these two points, and the present assumption represents the worst case scenario.

Figures 6.4 and 6.5 clearly illustrate a fully attached flow at the wing TE. The TKE profiles also confirm a fully attached BL by exhibiting the expected [29] larger values within the first $0.10(y/\delta)$. The streamlines for the clean configuration at $\alpha = 0°$ as well as the vorticity contours in Figure 6.6 further cemented the validity of the flow field based on canonic external flows over an airfoil. The streamlines did not indicate any flow separation, and the negative (clockwise) rolling BL vortex on the top surface of the wing was conclusively indicative of an attached boundary layer.

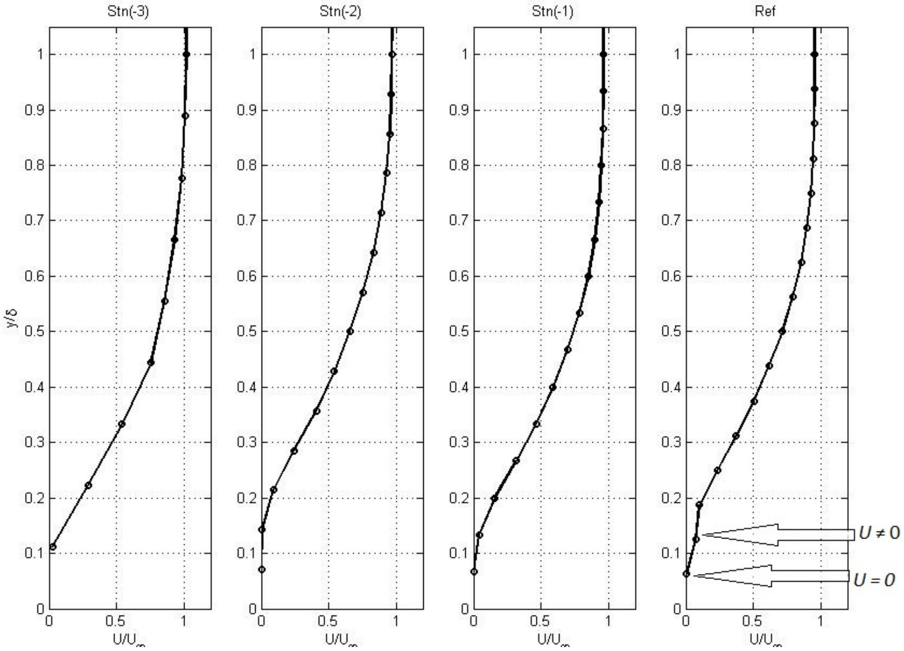

Figure 6.4: Clean configuration velocity profiles U/U_∞

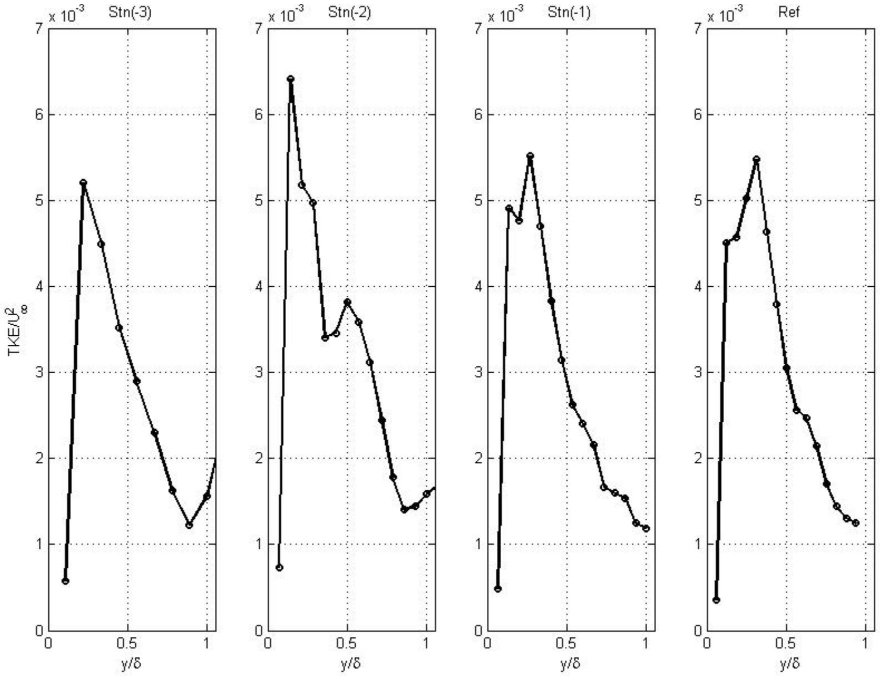

Figure 6.5: Clean configuration TKE profiles TKE/U_∞^2

The presence of the rolling vortex may also have been the result of the tripping wire, however it was uncertain whether this effect of the tripping wire would survive this far downstream given the strong turbulent eddies close to the surface.

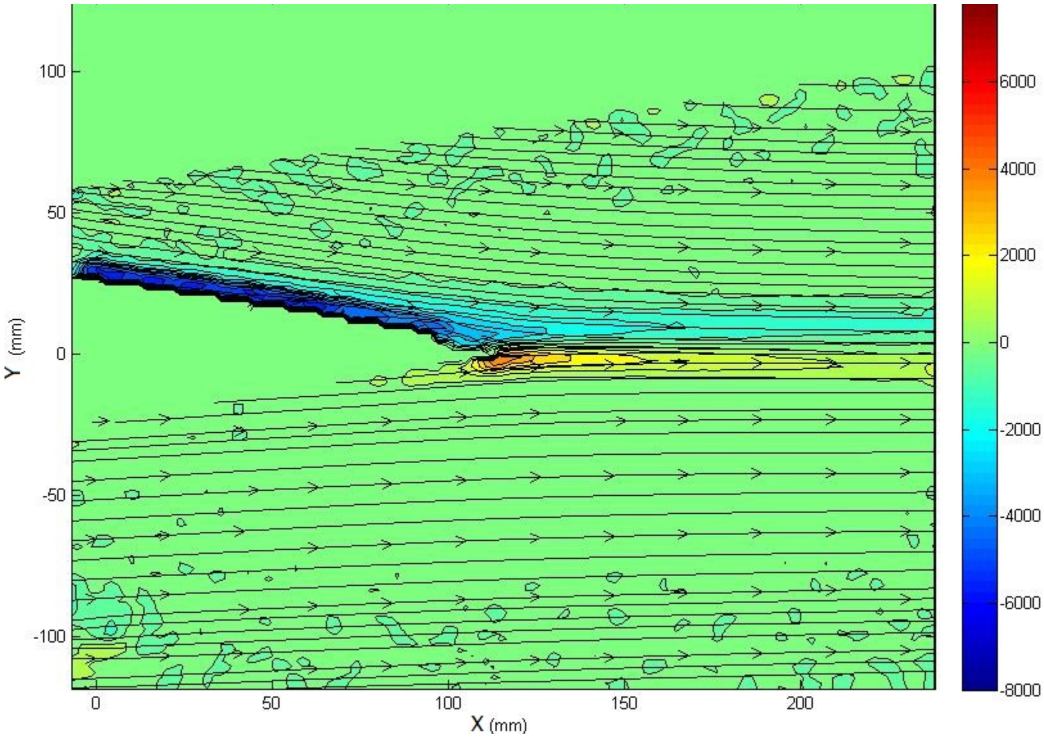

Figure 6.6: Mean spanwise vorticity contours, clean configuration at $\alpha = 0°$

Following the confirmation of the flow field, PIV data was acquired for increasing angles of attack. The angles of attack investigated included $0°, 5°, 10°, 12°$, and $14°$. Separation was first observed at the wing TE when α reached $10°$ as illustrated in Figures 6.7, 6.8, 6.9, and 6.10.

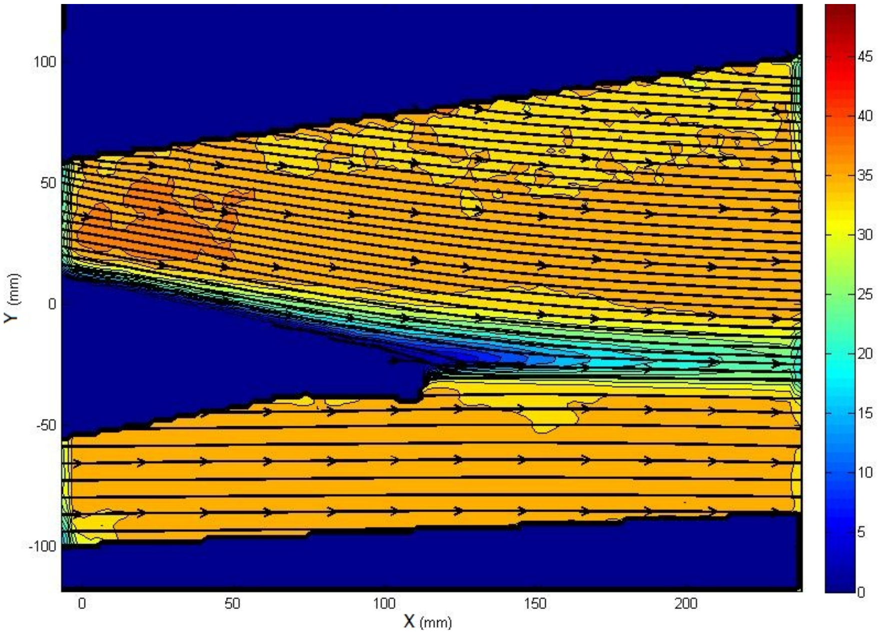

Figure 6.7: Clean config. at $\alpha = 5^\circ$ velocity magnitude ($\overline{V}$) contours (m/s) with streamlines

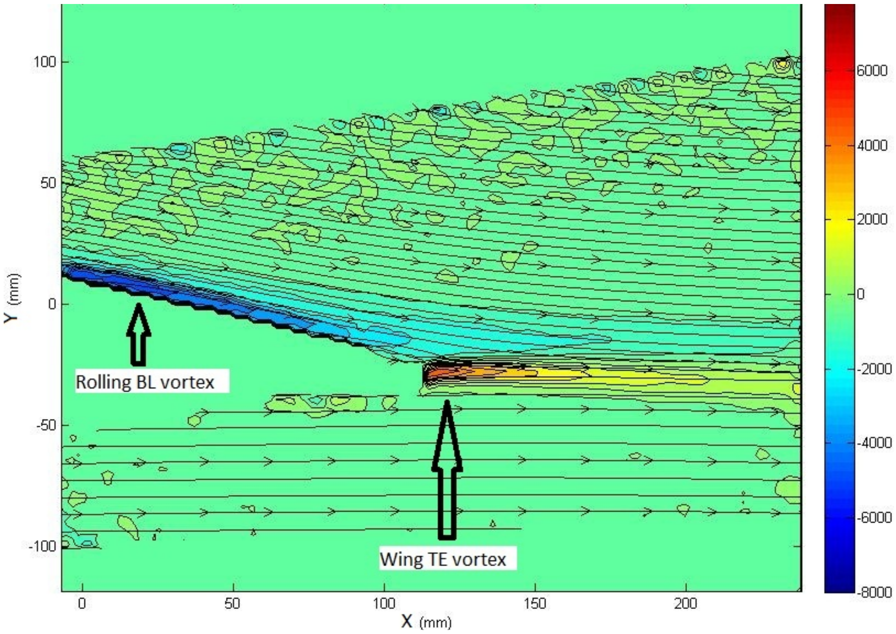

Figure 6.8: Clean config. at $\alpha = 5^\circ$ mean spanwise vorticity contours ($1/s$) with streamlines

Using the BL profiles (not shown), it was confirmed that at $\alpha = 10^\circ$, the BL separated at $0.945c_w$. It was noticed that although BL separation did not occur until $0.945c_w$, the gradual deterioration of the BL towards separation could be seen in the degradation of the rolling BL vortex as far upstream as $0.75c_w$. The eventual

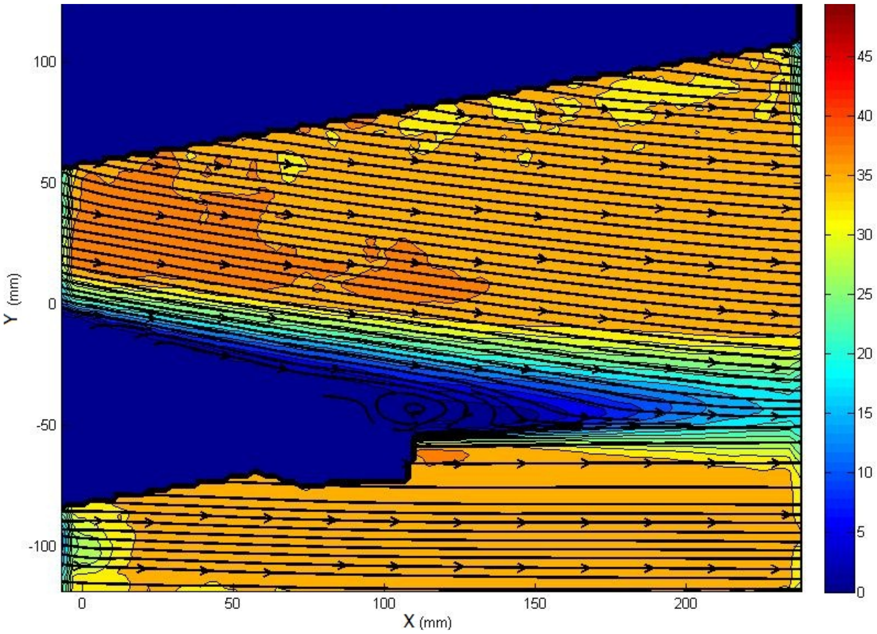

Figure 6.9: Clean config. at $\alpha = 10^\circ$ velocity magnitude ($\overline{V}$) contours (m/s) with streamlines

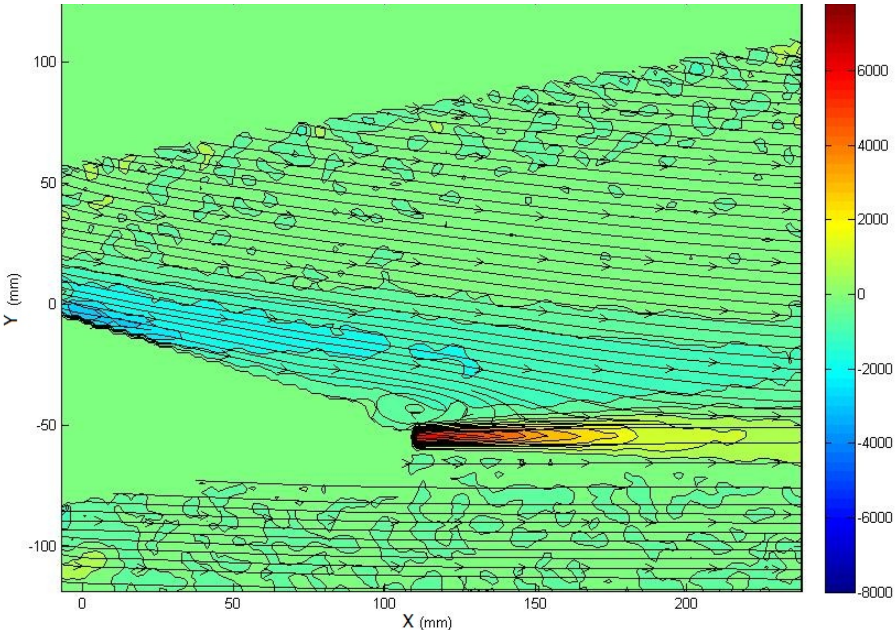

Figure 6.10: Clean config. at $\alpha = 10^\circ$ mean spanwise vorticity contours ($1/s$) with streamlines

breakup of the rolling BL vortex by the strong adverse pressure gradient at $\alpha = 10^\circ$ then resulted in increased mixing near the wing TE.

The magnitude of the strong positive (counter-clockwise) wing TE vortex was also investigated. Table 6.1 summarizes the maximum vorticity of the wing TE vortex at various angles of attack. Indicative of the Kutta condition, the magnitude of the wing TE vortex, had a direct correlation to the angle of attack. As the angle of attack increased and a recirculation region formed near the wing TE, the increased velocity difference between the top and bottom of the wing resulted in a increase in the wing TE vortex magnitude. The increase in the intensity of the wing TE vortex at higher angles of attack is shown in Figures 6.11 and 6.12.

Table 6.1: Maximum mean spanwise vorticity magnitude of TE vortex and separation location

Angle of Attack	ω $(1/s)$	Separation location (x/c_w)
0°	4258	none
5°	4935	none
10°	6395	0.945
12°	6604	0.876
14°	7198	<0.74

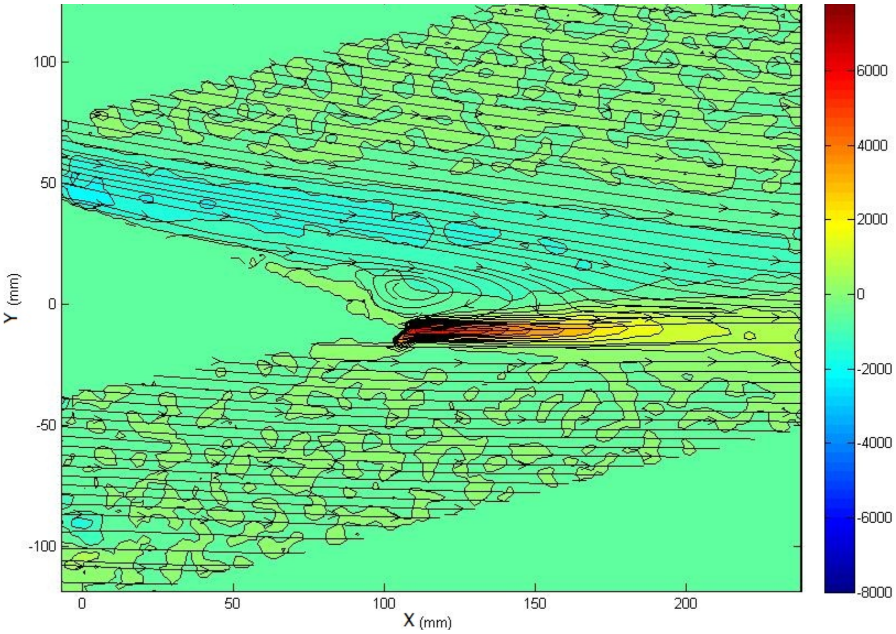

Figure 6.11: Clean config. at $\alpha = 12°$ mean spanwise vorticity contours $(1/s)$ with streamlines

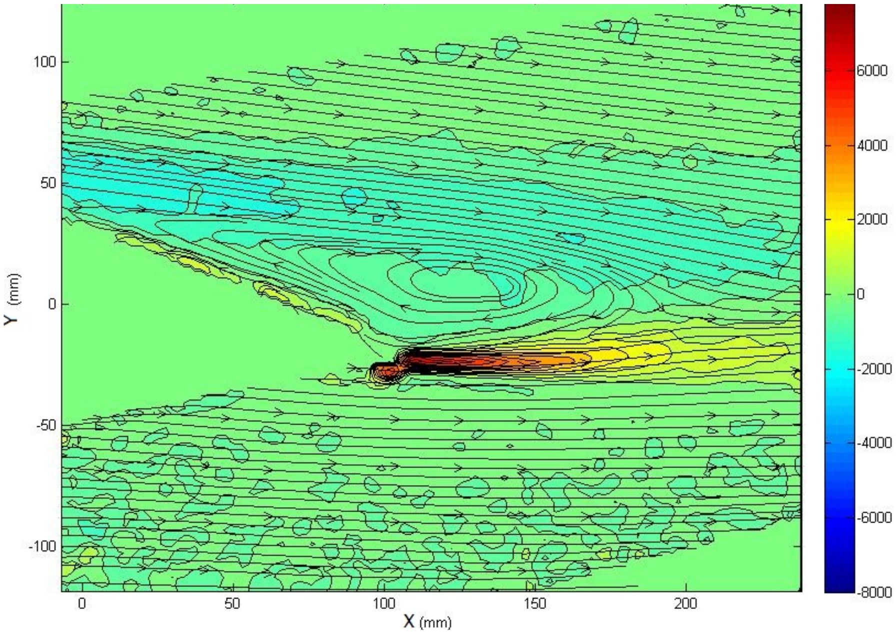

Figure 6.12: Clean config. at $\alpha = 14°$ mean spanwise vorticity contours $(1/s)$ with streamlines

6.3 Flow Development over the Wing

Since the flow over the flap was massively separated in the experiment for all the landing configurations, the investigation of the landing configuration began by scrutinizing the BL on the TE of the main wing, and the effect of the flap gap and overlap variation on the BL. For the manufacturer specified flap position (G0-O0 see Figure 5.7) at $\alpha = 0°$, the flow over the wing TE was fully attached as can be seen in Figures 6.13 and 6.14. These mean velocity, U, and TKE profiles showed similar flow conditions to those found at the TE of the clean configuration.

With an increased flap gap, it was found that the flow at the wing TE remained attached, and the BL experienced an improvement in flow quality, as indicated by a fuller velocity profile and a corresponding decrease in the BL shape parameter H ($H_{G0-O0} \approx 3.05, H_{G2-O0} \approx 2.80$, and $H_{G4-O0} \approx 2.78$). These results were found to be in agreement with Wentz et al [106], but were never explained why. The BL profiles for configuration G4-O0 are shown in Figures 6.15 and 6.16.

With an increase in the flap overlap however, the BL near the wing TE was forced towards separation, its BL shape parameter H increased until, in configura-

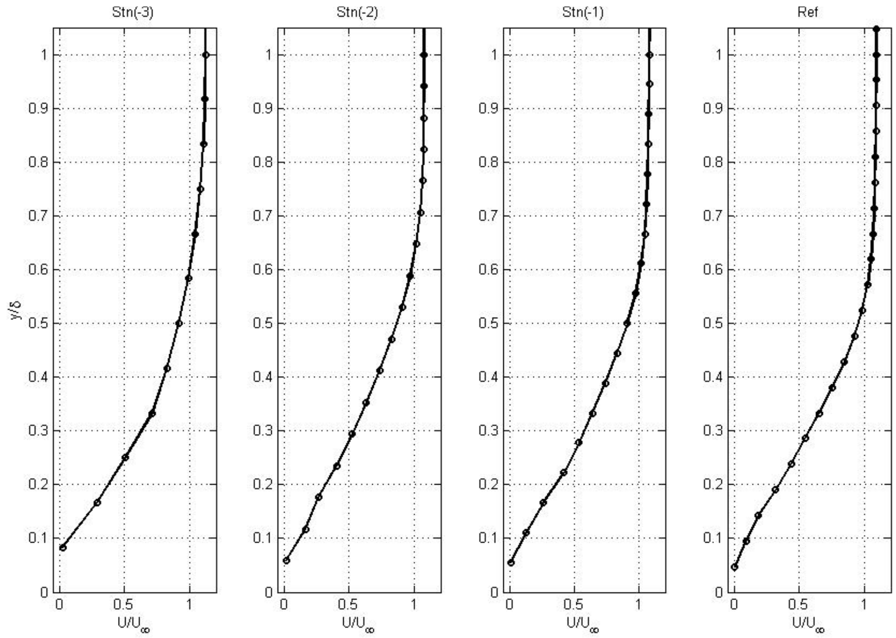

Figure 6.13: U/U_∞ velocity profiles at wing TE of G0-O0 (Gap = 0, Overlap = 0, $\delta_{flap} = 40°$) configuration at $\alpha = 0°$

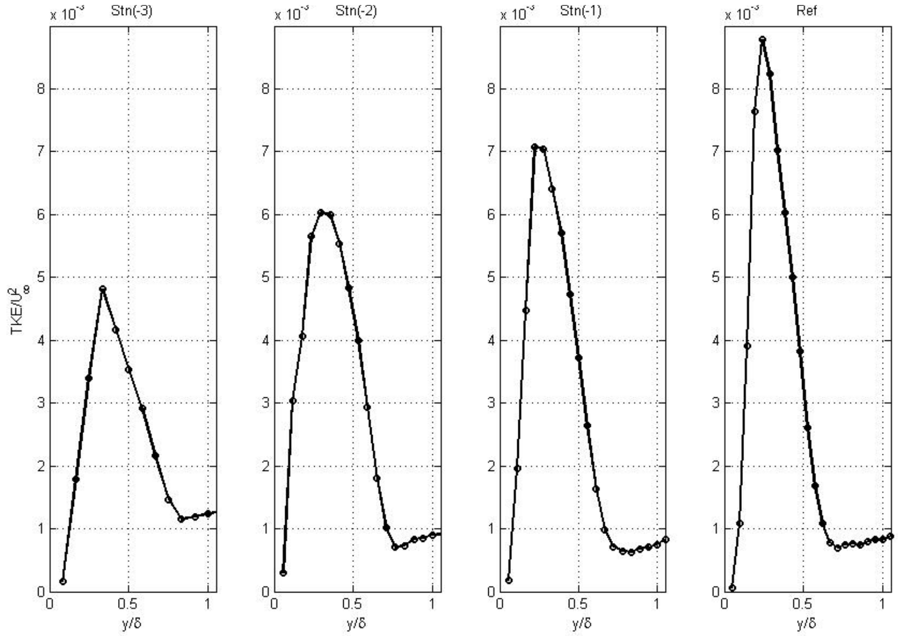

Figure 6.14: TKE/U_∞^2 profiles at wing TE of G0-O0 (Gap = 0, Overlap = 0, $\delta_{flap} = 40°$) configuration at $\alpha = 0°$

tion G0-O4, a separation bubble formed at Stn(-1) as illustrated in Figure 6.17. The TKE profiles in Figure 6.18 also confirmed the approach and presence of separation by the appearance of a secondary peak near the wing surface. Figure 6.19 focuses

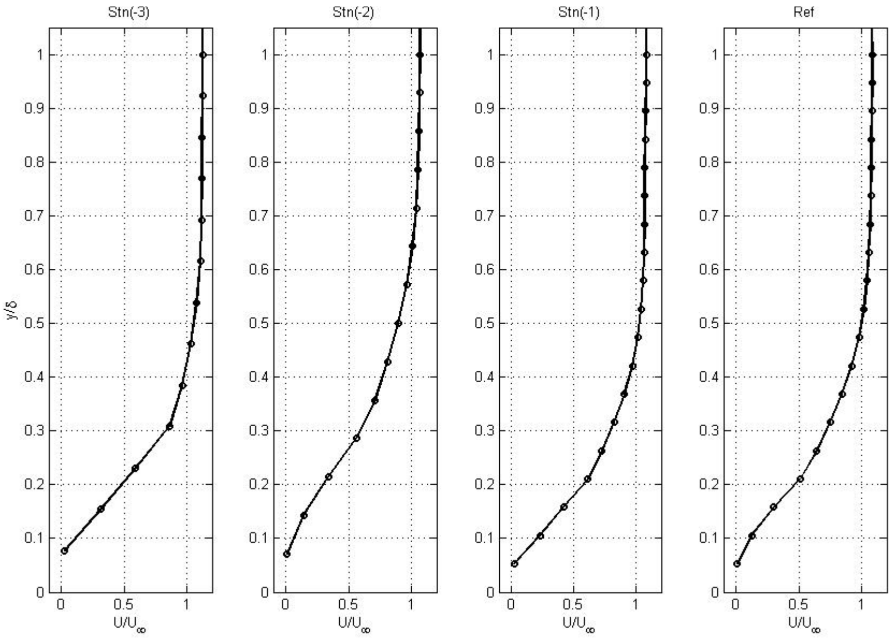

Figure 6.15: U/U_∞ velocity profiles at wing TE of G4-O0 (Gap = 4, Overlap = 0, $\delta_{flap} = 40°$) configuration at $\alpha = 0°$

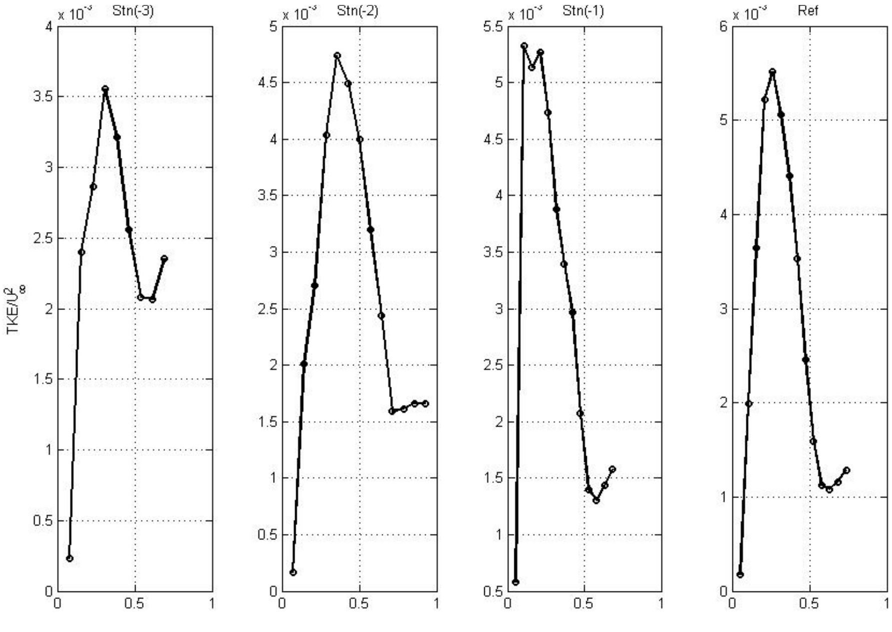

Figure 6.16: TKE/U_∞^2 profiles at wing TE of G4-O0 (Gap = 4, Overlap = 0, $\delta_{flap} = 40°$) configuration at $\alpha = 0°$

on the relatively small separation bubble near the wing TE, and highlights the local flow reversal. Note that the physical spacing between the BL profiles in Figure 6.19 was $1.94mm$. The BL re-attachment on the wing TE in configuration G0-O4 could

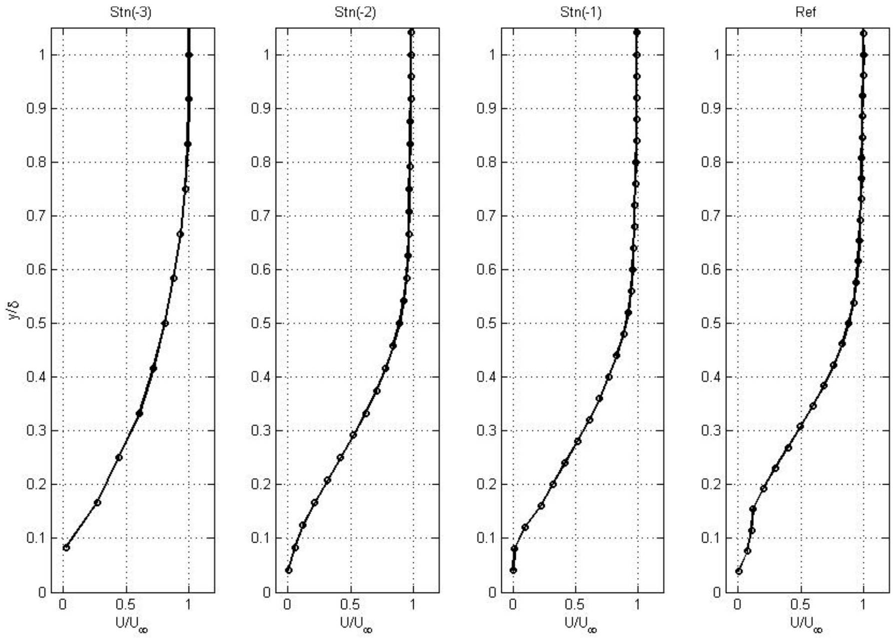

Figure 6.17: U/U_∞ velocity profiles at wing TE of G0-O4 (Gap = 0, Overlap = 4, $\delta_{flap} = 40°$) configuration at $\alpha = 0°$

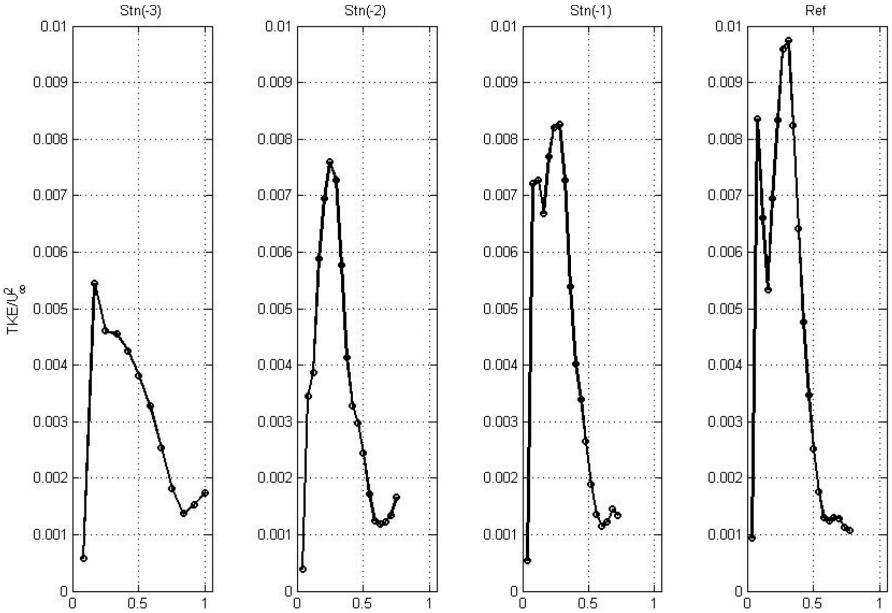

Figure 6.18: TKE/U_∞^2 profiles at wing TE of G0-O4 (Gap = 0, Overlap = 4, $\delta_{flap} = 40°$) configuration at $\alpha = 0°$

be explained by the presence of the slot flow which induced a strong favourable pressure gradient to the flow in the trailing edge regions, energizing the flow so that it temporarily reattached.

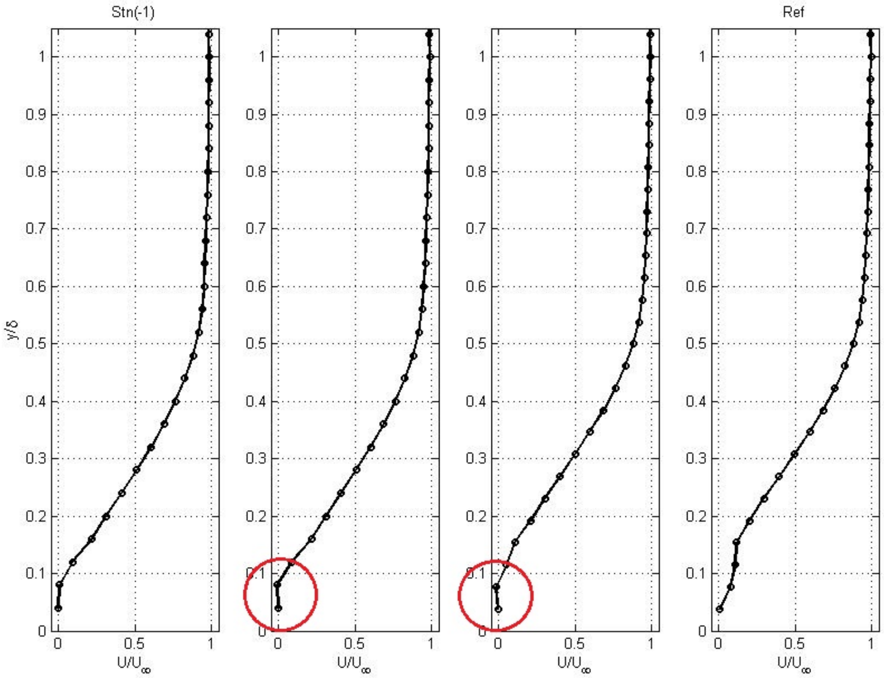

Figure 6.19: U/U_∞ velocity profiles at wing TE of G0-O4 (Gap = 0, Overlap = 4, $\delta_{flap} = 40°$) configuration at $\alpha = 0°$ highlighting local flow separation

The present analysis of the flow development over the wing has revealed new trends in this complex flow field. However, the dominant flow feature of a slotted flap configuration is the slot flow itself. Due to the novelty, importance and complexity of the experimental results and subsequent analysis, the slot flow findings and interpretation were deferred to Chapter 7.

6.4 CFD Results

The accuracy of the CFD simulations was evaluated by comparing the BL separation location in the clean configuration. At $\alpha = 0°$ and $\alpha = 5°$, neither the CFD nor the experiment indicated any BL separation along the wing. At $\alpha = 10°$, the experimental results showed BL separation at $0.945c_w$. Of the three turbulence models employed, only the SST model was able to predict such a separation, but farther downstream at $0.995c_w$ as shown in Figures 6.20 and 6.21. This separation underestimation was further exacerbated at $\alpha = 12°$ and $\alpha = 14°$. At $\alpha = 12°$, the experimental results

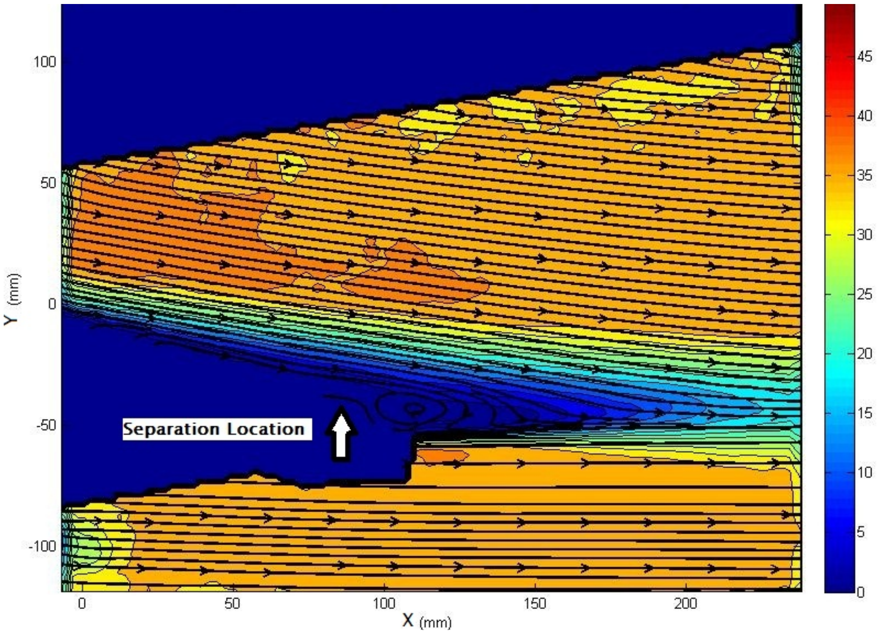

Figure 6.20: Clean configuration velocity contours $\alpha = 10°$ using PIV

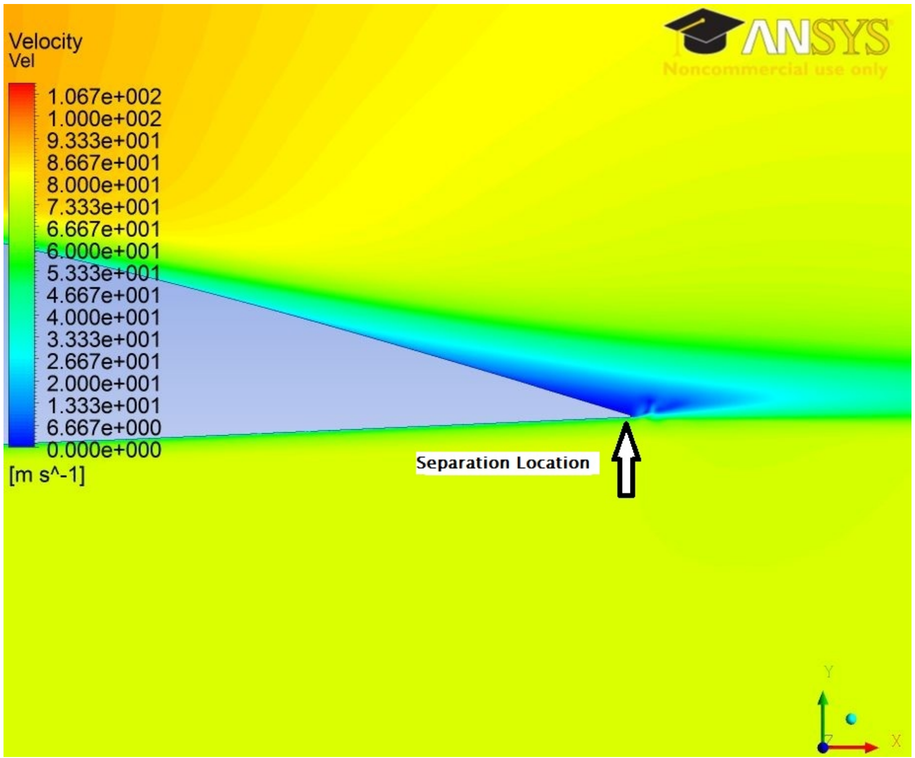

Figure 6.21: Clean configuration velocity contours $\alpha = 10°$ using CFD (SST)

depicted a separation location at $0.88c_w$; both the SA and SST turbulence models predict separation at $0.95c_w$, while the RSM model failed to predict any separation at all. At $\alpha = 14°$, the experimental separation location was no longer in the camera field of view ($< 0.74c_w$), whereas the CFD predicted separation at SA $= 0.89c_w$, SST $= 0.89c_w$, and RSM $= 0.95c_w$. The approach of flow separation in the experiment seemed to be reflected in the TKE profiles by the presence of a secondary peak in TKE, indicative of velocity profile inflection points and increased mixing.

As can be seen in Figures 6.22 and 6.23, the flow character of the landing configuration was not depicted accurately by the RANS CFD. While the CFD predicted attached flow over the flap for the G0-O0 configuration and partially attached flow for the G0-O2 and G0-O4 configurations, the experiments revealed a massive separation region over the flap for all configurations. Similar results were obtained for the gap variation. This discrepancy between the CFD and experiments can be partially attributed to the difference in the slot flow; the CFD solution led to a computed velocity magnitude at the slot exit (Figure 6.24) that was greater by a factor of two as illustrated in Figure 6.25 and 6.26. For this reason, the 'a priori' configurations were simulated next, in which the correct slot flow velocity magnitude and direction based on the experimental results were incorporated.

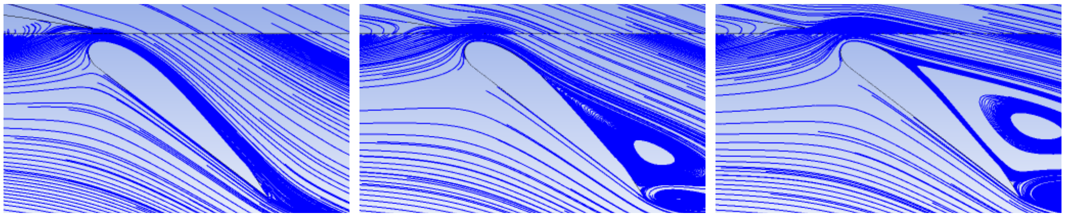
(a) (b) (c)

Figure 6.22: CFD Streamlines over the flap, (a) G0-O0 SA (b) G0-O2 SA (c) G0-O4 SA

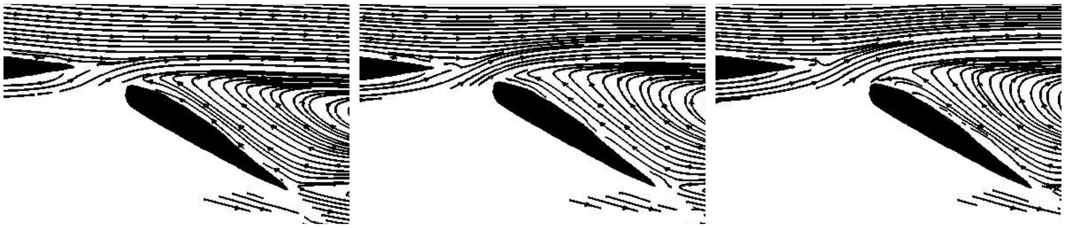
(a) (b) (c)

Figure 6.23: Experimental Streamlines, (a) G0-O0 (b) G0-O2 (c) G0-O4

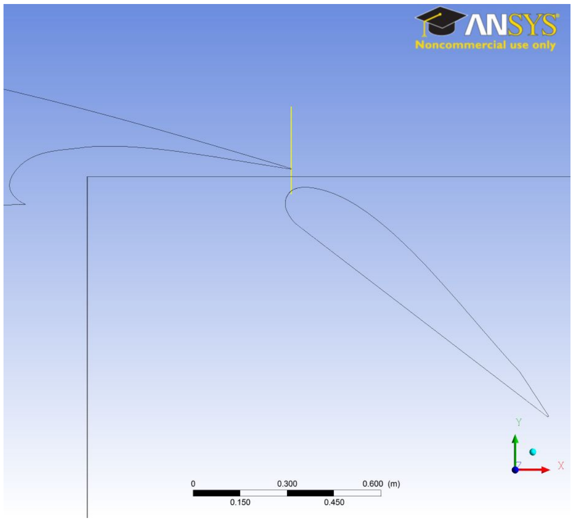

Figure 6.24: Location of the slot flow profiles illustrated in Figures 6.25 and 6.26

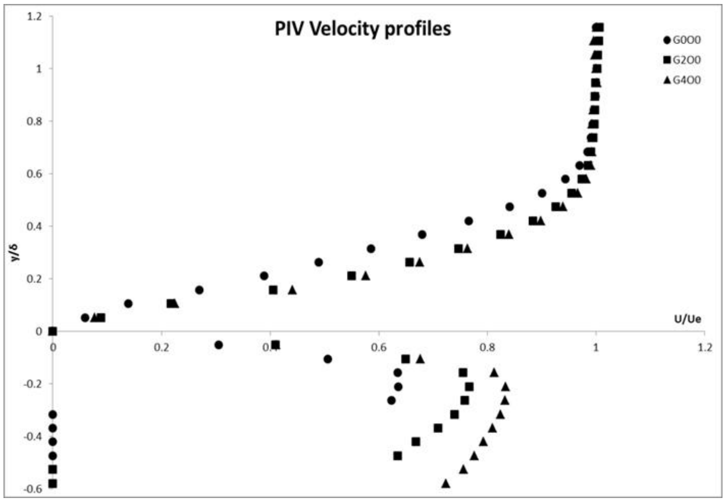

Figure 6.25: PIV slot flow profiles at $\alpha = 0°$ at wing TE, ● = G0-O0, ■ = G2-O0, ▲ = G4-O0

In an effort to reconcile the CFD with the experimental results, a new mesh was constructed, which enabled the user to 'force' a slot flow emanating from the flap slot of correct velocity magnitude as that found in the experiments. Only configurations G0-O0, G1-O0 and G2-O0 were simulated. Figure 6.29 shows the velocity profiles above the flap. As can be seen in Figures 6.27 and 6.28, there is a dramatic improvement in the level of agreement between the CFD and the experiment. Although the 'a priori' configuration depicted the flow character accurately, a quantitative comparison of the wake profiles revealed that the quantitative agreement of the individual velocity profiles was only fair.

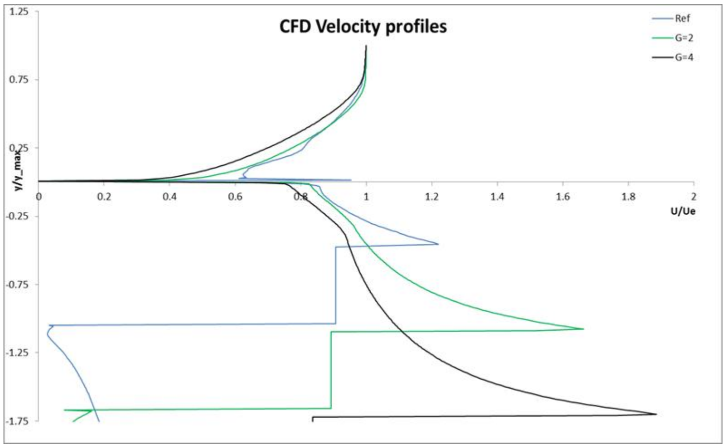

Figure 6.26: CFD slot flow profiles at $\alpha = 0°$ at wing TE, blue = G0-O0, green = G2-O0, black = G4-O0

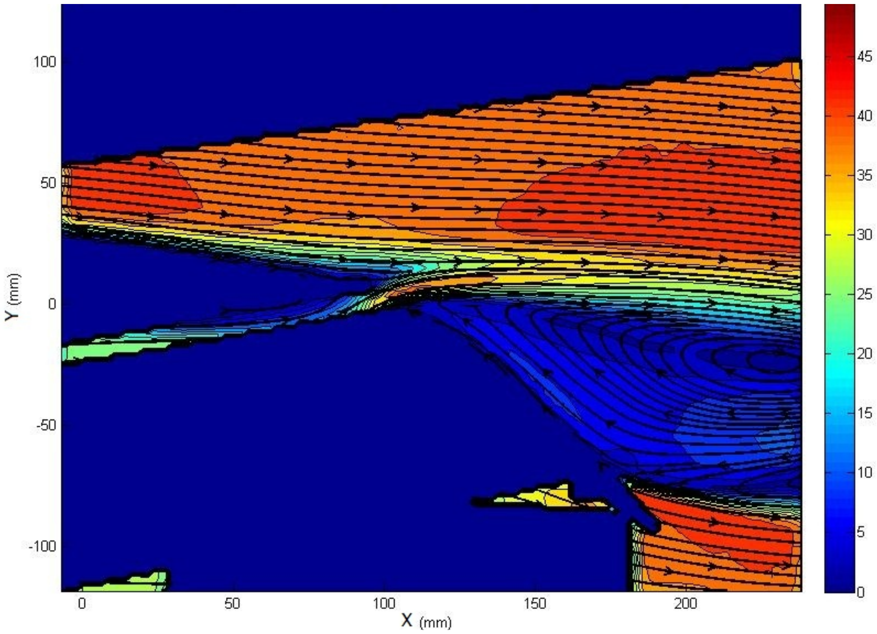

Figure 6.27: Landing configuration (G0-O0) velocity contours $\alpha = 0°$ using PIV

One of the reasons for this lack of agreement was the slot flow velocity profile infused into the flow. Due to the relatively low resolution of the PIV (see Figure 6.25), a detailed velocity profile of the slot flow was not obtained. As a result, the slot flow was defined with a uniform velocity profile, which can be seen at stations 1 and 2 of Figure 6.29. This uniform velocity profile introduced additional momentum to the flow, which was not present during the experimental campaign. Consequently, the uniform velocity profile maintained its flat identity further downstream, and the

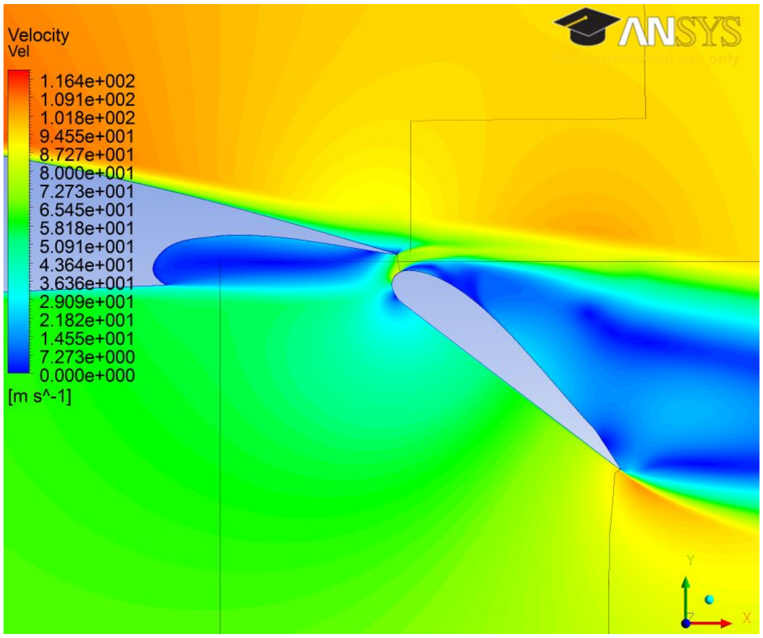

Figure 6.28: Landing configuration (G0-O0) velocity contours $\alpha = 0°$ using CFD (SA)

additional momentum led to a noticeable decrease in the magnitude of the reversed flow over the flap.

As the flap gap increased in size, the slot flow became less affected by the vorticity at the slot exit, and the slot flow developed a ‘core’. This ‘core’ was also noted by Wentz et al [106] and Foster et al [28] in their experiments. As a result, the agreement between CFD and PIV of configuration G2-O0 was improved in comparison to configuration G0-O0, as shown in Figure 6.30. This seemed to validate the fair CFD to PIV agreement of the G0-O0 configuration which seemed to have resulted from a poor definition of the slot flow velocity profile. The slot flow velocity profile of the G2-O0 configuration was also not matched to the slot flow velocity profile found in the experiment, hence the CFD to PIV agreement was good.

With the flow downstream of the slot seeing a marked improvement in accuracy, the attention was turned back to the wing TE BL. As can be seen in Figure 6.31, the wing TE BL computed by the ‘a priori’ simulations still did not exhibit the same trend in the BL flow found during the experimental campaign. In fact, the opposite trend was depicted by the ‘a priori’ simulations. It is believed that this deficiency could also be the result of the estimated uniform velocity slot flow. The additional

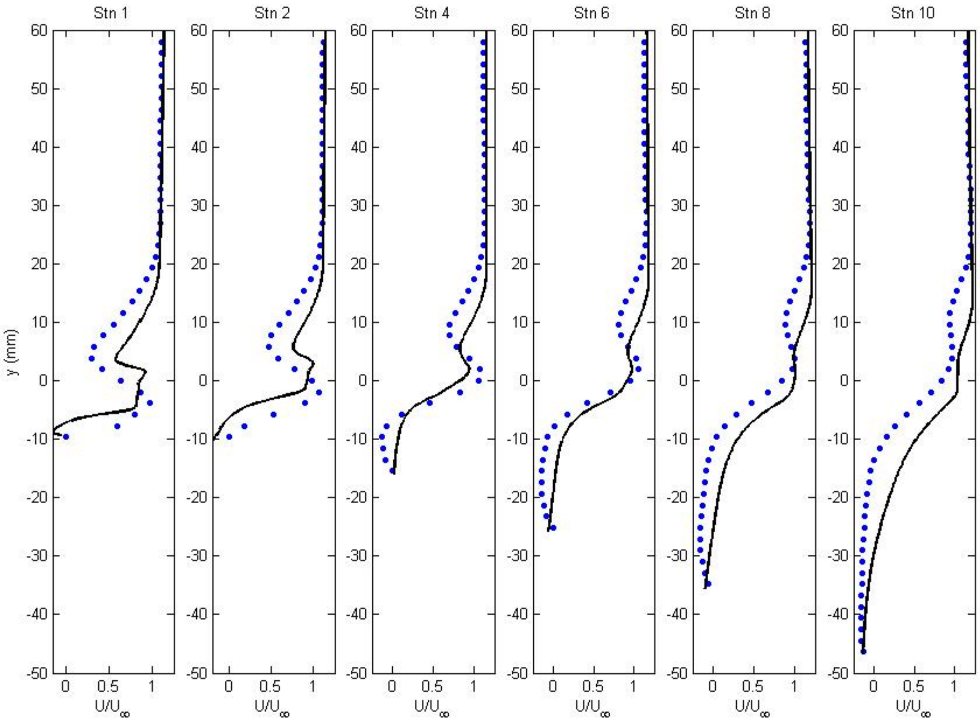

Figure 6.29: CFD vs PIV comparison of wing wake velocity profiles of configuration G0-O0

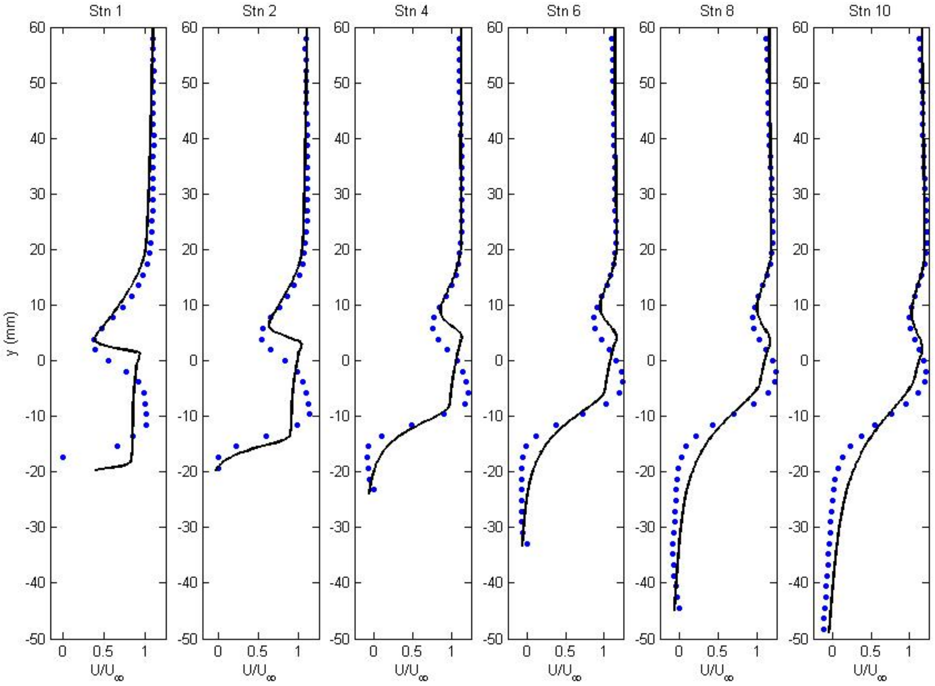

Figure 6.30: CFD vs PIV comparison of wing wake velocity profiles of configuration G2-O0

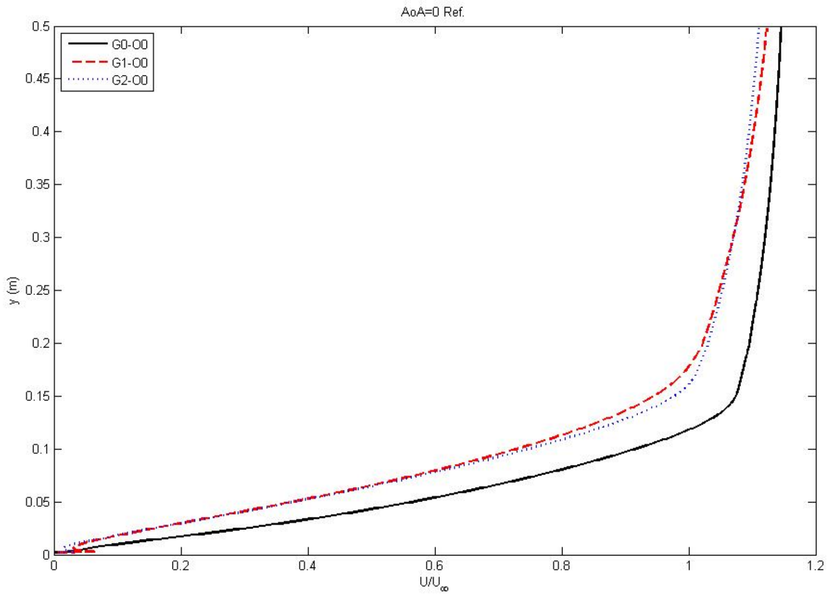

Figure 6.31: Wing TE BL variation with flap gap as computed by CFD ‘a priori’ simulation

momentum at the slot flow periphery could have had a significant effect on the BL confluence which may have affected the upstream flow of the wing TE BL. The exact reason for this discrepancy remains uncertain. It is likely that, while the slot flow definition was not exact, the diffusive nature of the turbulence models employed in RANS simulations also contributed to the disagreement between the CFD simulations and the experimental data.

The C_l values obtained from the ‘a priori’ simulation were considerably lower than the original CFD simulations. As the exact value of the landing configuration C_l was questionable due to the poor flow prediction, the change in C_l resulting from the change in geometry was compared. The decrease in C_l found in both simulation approaches are summarized in Table 6.2.

Table 6.2: Cumulative C_l decrease with increasing flap gap

Config.	CFD	‘a priori’ CFD
G0-O0	0	0
G1-O0	0.08	0.145
G2-O0	0.43	0.165

Interestingly, the initial decrease in lift coefficient, corresponding to a flap gap increase of $0.01c_w$, increased in the 'a priori' simulation. For the following $0.01c_w$ flap gap increase however, the decrease in C_l was markedly reduced. This was most likely due to the relative lack of change in the flow field depicted in the 'a priori' simulations with an increasing flap gap, as opposed to the significant change in the flow separation region over the flap computed in the simulations without any 'a priori' knowledge.

Chapter 7

Slot Flow Analysis

The following analysis of the experimental slot flow, to the best knowledge of the author, is the only attempt found to date at a detailed explanation of the flow behaviour of a wing equipped with a slotted flap. Even though a significant number of studies focused at quantifying the effect of the change in the slot geometry on the aerodynamic forces [28] [109] [108] [106], a detailed explanation of the flow behaviour has not been reported in the literature.

Although the slot flow has not customarily been referred to as a jet [28] [109], it will be shown that given a minimum gap size, the slot flow did indeed resemble and behave like a jet. For the duration of this study, the slot flow will be referred to as a jet regardless of the gap size. In order to analyse the jet flow and its development for various configurations, the jet velocity profile was adjusted for location and inclination according to the local flow coordinate system (x - y) illustrated in Figure 6.1. First, the magnitude of the maximum velocity vector, $\overline{V}_{jetmax}$, and its position, y_{max}, were found for each jet velocity profile. Next, the mean velocity profiles were plotted against the coordinate $(y - y_{max})$. The angle associated with vector $\overline{V}_{jetmax}$ was identified as Θ_{max} which was defined with respect to the global X-axis. The jet progression was investigated at five locations beginning at the wing TE (Ref), Stn 3 was at $4.3\%c_w$ ($17mm$) downstream from the wing TE, Stn 5 was at $7.1\%c_w$ ($29mm$) downstream from the TE, Stn 7 was at $11.4\%c_w$ ($46mm$) downstream from the TE, and Stn 8 was at $14.7\%c_w$ ($60mm$) downstream from the TE.

The progression of the jet in configuration G0-O0 can be seen in Figure 7.1. The successive velocity decrease in $\overline{V}_{jetmax}$ resulting from the increased mixing downstream of the wing TE is evident. The TKE peaks found at stations 5, 7 and 8 in Figure 7.2 correspond to the inflection points found within the velocity profiles as expected. As indicated by the TKE profile at the reference location (wing TE), the

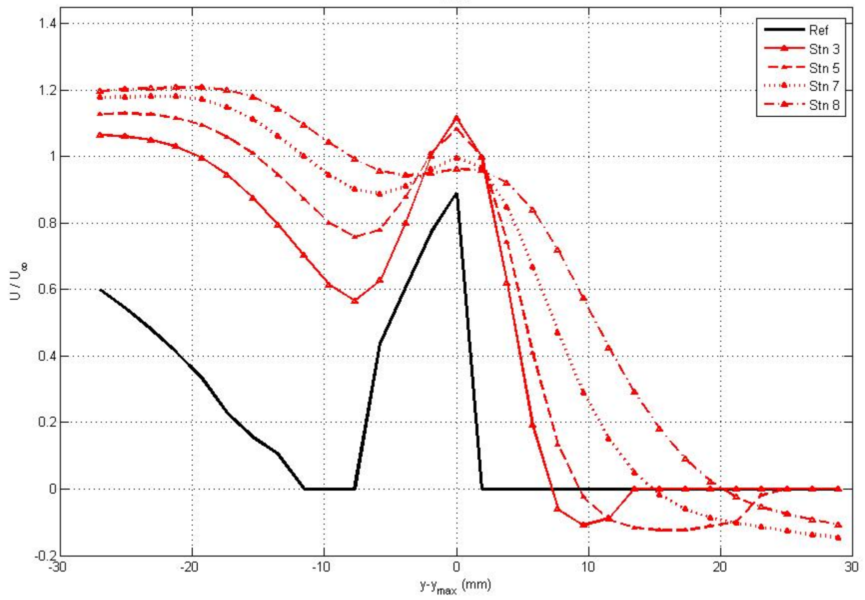

Figure 7.1: G0-O0 Jet velocity profiles at $\alpha = 0°$, U/U_∞

slot flow of this configuration did not exhibit a core flow indicative of a jet.

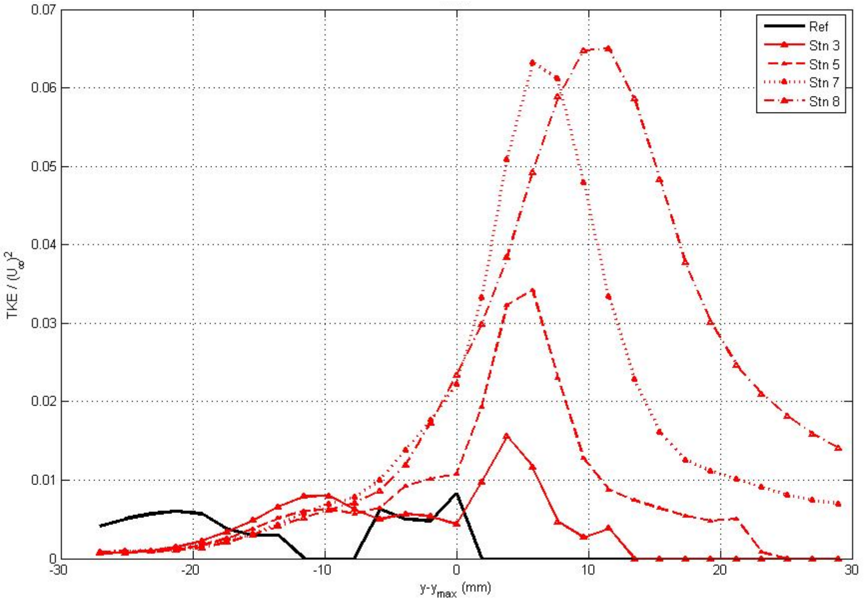

Figure 7.2: G0-O0 Jet TKE profiles at $\alpha = 0°$, TKE/U_∞^2

With an increase in flap gap, the slot flow assumed a jet-like flow quality, as shown in Figures 7.3 and 7.4. The TKE profiles revealed the jet-like flow character of this configuration by depicting two TKE peaks at the G4-O0 reference location, indicative of the emergence of a turbulent jet from a channel [87]. It was noted that with the increased flap gap, not only did the maximum velocity magnitude of the G4-O0 configuration increase compared to the G0-O0 configuration by 17%, but it also moved further downstream by $10.4\%c_w$ ($43mm$) from Stn 3 to Stn 8. The larger slot width thus increased the flow momentum, which made the jet far less susceptible to the mixing affected by the large recirculation region generated over the flap. The G4-O0 jet maintained its shape further downstream in comparison the G0-O0 jet. This conclusion was further supported by a decrease in the TKE by more than 35% with the increased flap gap, which was also indicative of reduced mixing between the jet and the recirculation region over the deployed flap. Hence, as suspected during the initial flap gap sizing, the momentum of the slot flow seemed to be the key flow characteristic of this flow configuration.

The presence of the jet in the G4-O0 configuration was further corroborated by the velocity and mean spanwise vorticity contours illustrated in Figures 7.5 and 7.6. While the vorticity at the wing TE and flap LE prevented the formation of a true jet in the G0-O0 configuration, the increase in the flap gap permitted the passage of an undisturbed core flow that can be seen passing through the slot in Figure 7.6.

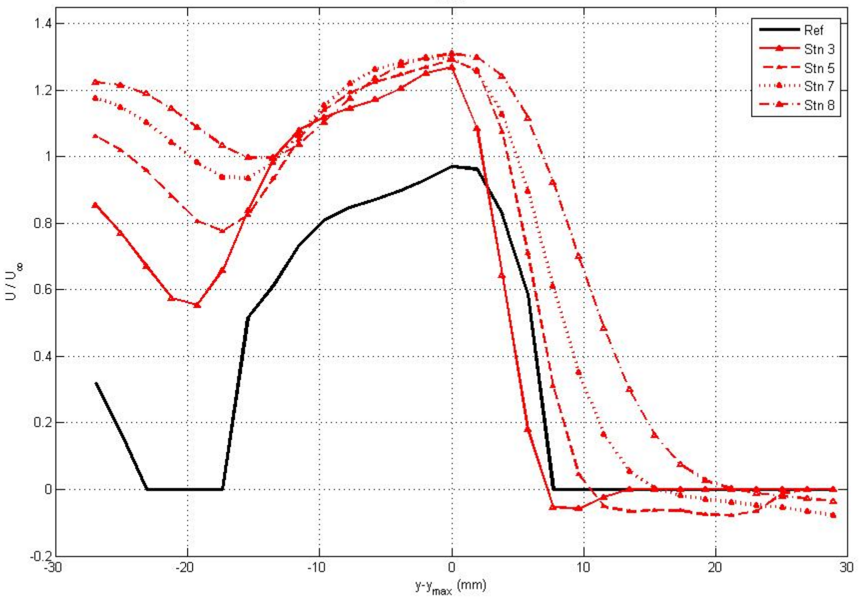

Figure 7.3: G4-O0 Jet velocity profiles at $\alpha = 0°$, U/U_∞

With an increase in flap overlap, the slot flow adopted a different character; as

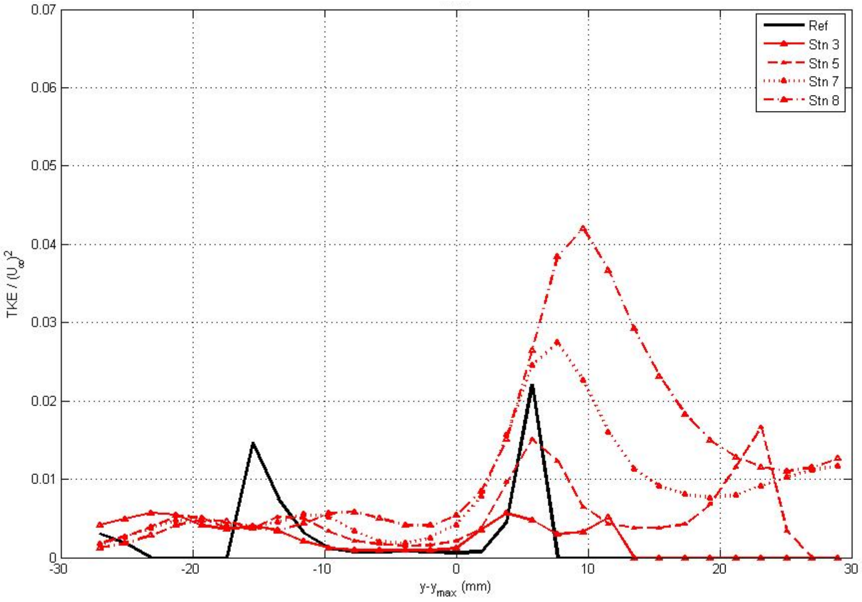

Figure 7.4: G4-O0 Jet TKE profiles at $\alpha = 0°$, TKE/U_∞^2

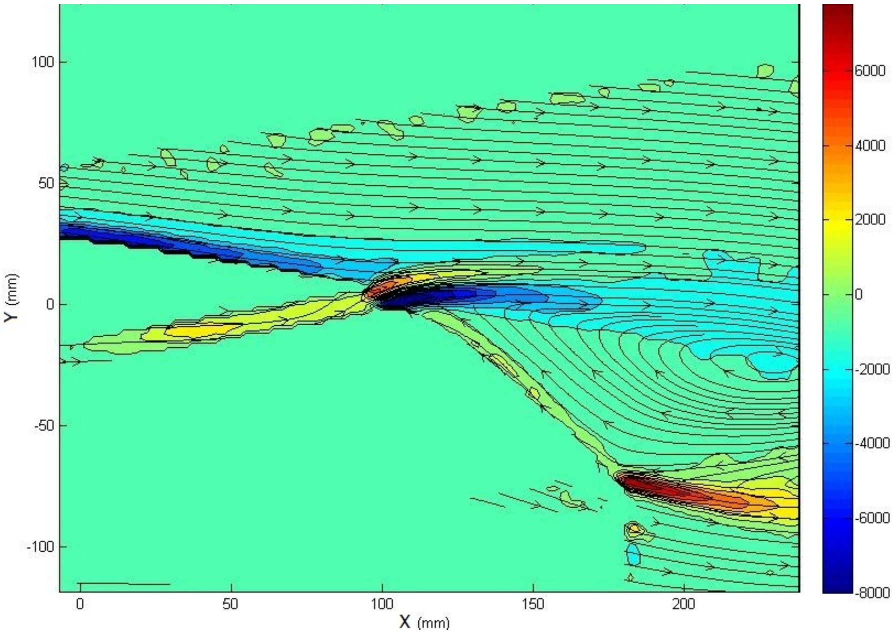

Figure 7.5: G0-O0 configuration mean spanwise vorticity contours $(1/s)$ with streamlines at $\alpha = 0°$

can be seen from Figure 7.7, $\overline{V}_{jetmax}$ of the G0-O4 configuration also increased in magnitude and traversed downstream in comparison to the G0-O0 configuration, but the $\overline{V}_{jetmax}$ increase was 5% less than the G4-O0 configuration $\overline{V}_{jetmax}$. The jet-like flow definition at the slot exit (Ref Stn) in Figure 7.8 was not as definitive for the G0-

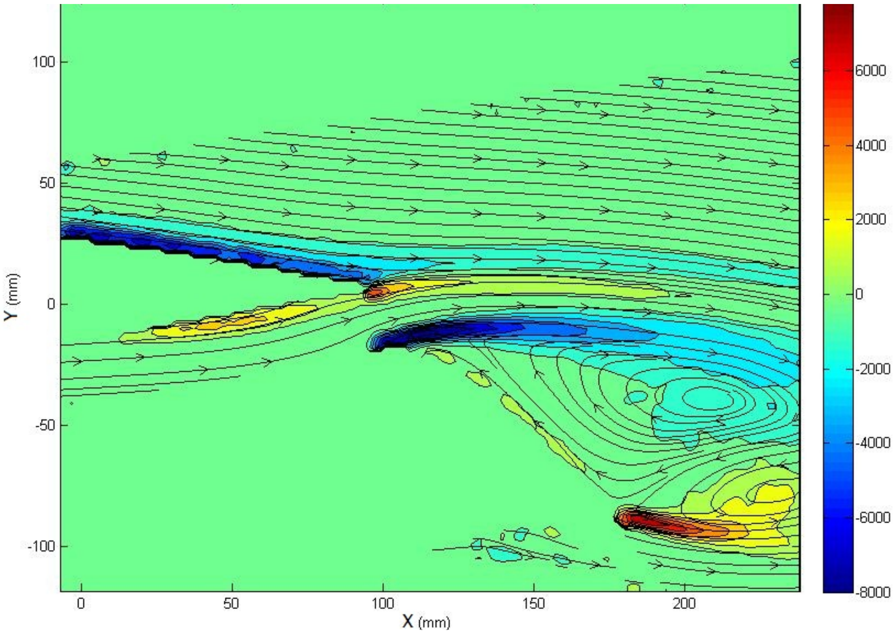

Figure 7.6: G4-O0 configuration mean spanwise vorticity contours $(1/s)$ with streamlines at $\alpha = 0°$

O4 configuration compared to the G4-O0 configuration. More surprisingly however, the level of TKE in the G0-O4 configuration was more consistent with the G0-O0 configuration rather than the G4-O0 configuration. In fact, the G0-O4 configuration saw a mere 8% decrease in the TKE at Stn8 compared to the G0-O0 configuration. This was in sharp contrast to the 35% decrease noted in the G4-O0 configuration at the same downstream location.

7.1 Interpretation of the Flow Behaviour

In an effort to quantify the jet velocity profile definition, a velocity defect was defined for this purpose as the difference between the maximum jet velocity, $\overline{V}_{jetmax}$, and the point of confluence corresponding to the point of merger between the jet and the BL that was shed from the main wing. For example, for the G0-O0 jet at station 8, $\overline{V}_{jetmax}/U_\infty = 0.962$, while the velocity at the point of merger was $\overline{V}_{merger}/U_\infty = 0.942$ thus resulting in a velocity defect of $\delta\overline{V}_{G0O0} = 0.02$. The velocity defect at station 8 for configuration G4-O0 was $\delta\overline{V}_{G4O0} = 0.31$ while for configuration G0-O4 the defect was only $\delta\overline{V}_{G0O4} = 0.20$. This finding also indicates a significant increase in mixing from the G4-O0 to the G0-O4 configuration.

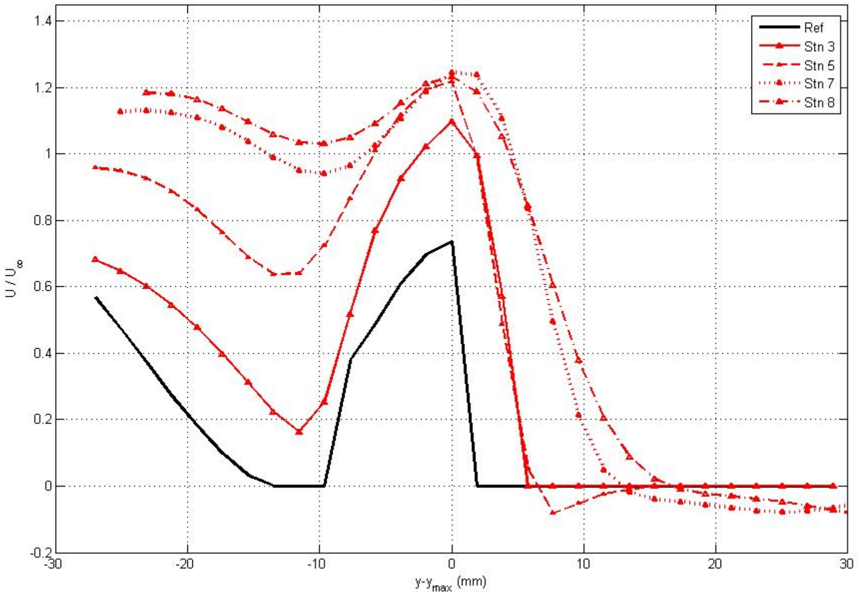

Figure 7.7: G0-O4 Jet velocity profiles at $\alpha = 0°$, U/U_∞

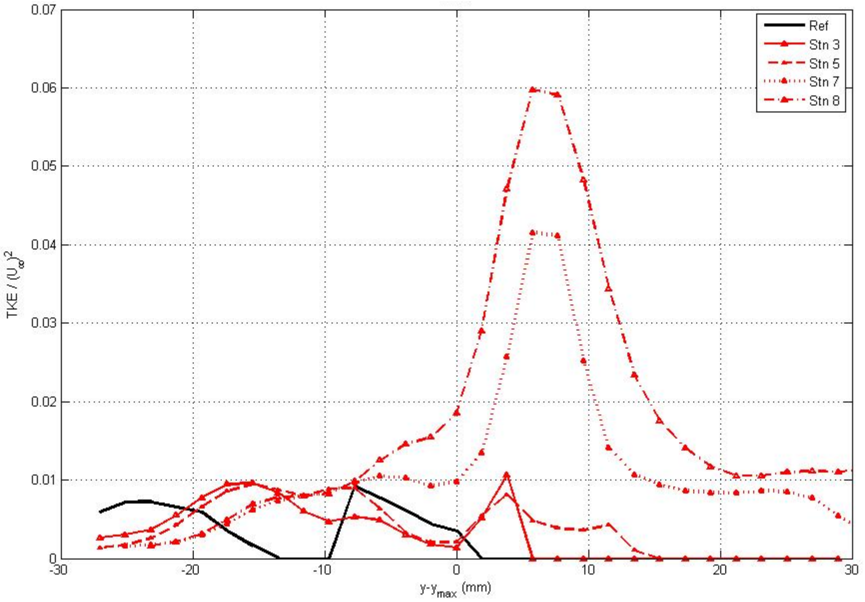

Figure 7.8: G0-O4 Jet TKE profiles at $\alpha = 0°$, TKE/U_∞^2

The mean spanwise vorticity contours of configuration G0-O4 were also revealing. While the streamlines in Figure 7.9 illustrated the deflection of the flow up, it was the vorticity contours that elucidated the mechanism behind this phenomenon.

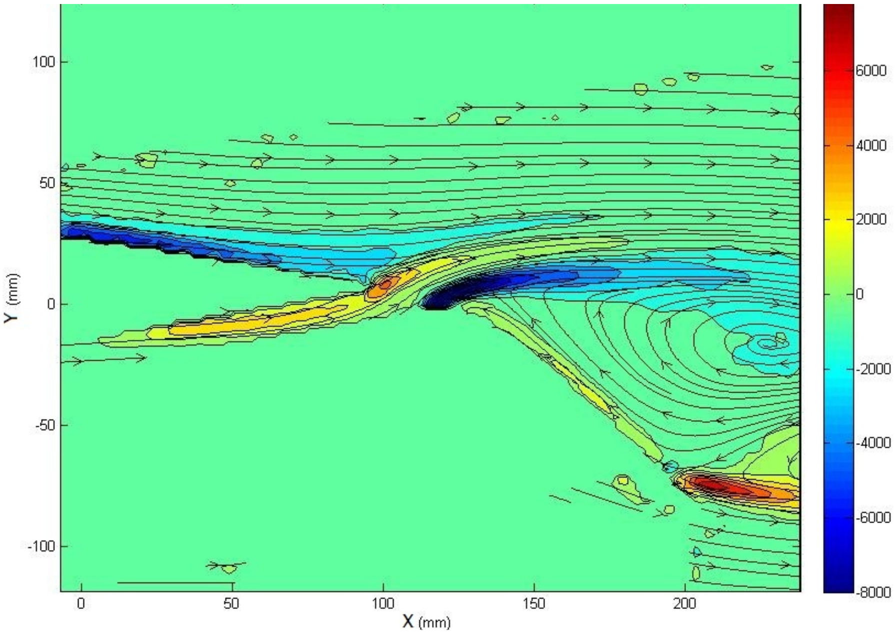

Figure 7.9: G0-O4 configuration mean spanwise vorticity contours (1/s) with streamlines at $\alpha = 0°$

The two counter-rotating vortices at the wing TE and the flap LE acted to direct the core flow of the jet beyond the slot opening. As long as these two vortices were positioned vertically with respect to each other as they were in configuration G4-O0, the resulting jet flow was nearly horizontal. However, if the vortex at the flap LE was offset horizontally as in configuration G0-O4, this resulted in an increase in the flow angling. Therefore, it was not simply the flow flowing over the flap and avoiding the flap like an obstacle that caused the sudden vertical displacement of the jet, but the action of the two counter-rotating vortices as well.

This jet angle, Θ_{max}, which was defined as the direction of $\overline{V}_{jetmax}$ with respect to the X-axis, was investigated further. The most significant difference between the G4-O0 and G0-O4 jets was the maximum magnitude of Θ_{max} and its streamwise location with respect to the wing TE. With a variation in flap gap, the maximum Θ_{max} decreased from $\Theta_{max} = 40°$ to $\Theta_{max} = 32°$ from configuration G0-O0 to G4-O0 respectively. With an increasing overlap however, Θ_{max} increased from the initial $\Theta_{max} = 40°$ to $\Theta_{max} = 42.5°$ from the G0-O0 to G0-O4 configuration respectively. These results are shown in Figures 7.10 and 7.11. The location of Θ_{max} also varied significantly between the configurations. It was found that with a variation in overlap, Θ_{max} traversed downstream the exact distance corresponding to the increase in the flap overlap, while the location of Θ_{max} remained stationary as a function of gap. Hence, the location of $\overline{V}_{jetmax}$ and Θ_{max} was found to be invariant with respect to the flap reference frame.

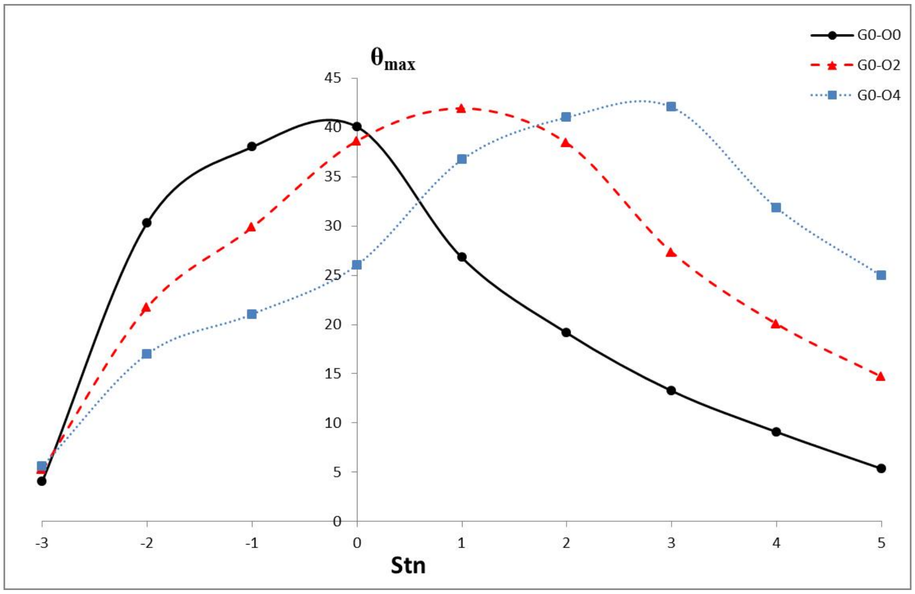

Figure 7.10: Maximum jet angle progression, Θ_{max} (deg), with increase in flap gap

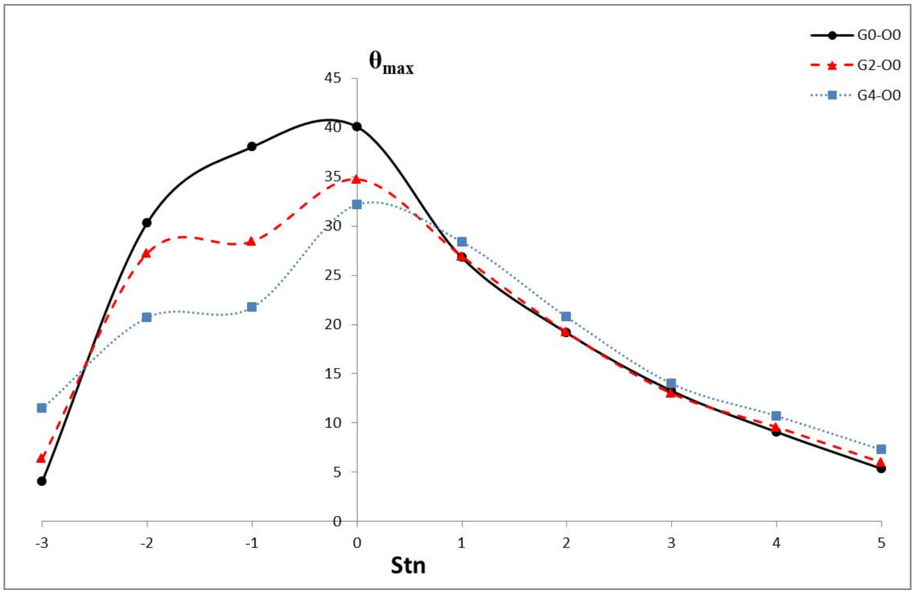

Figure 7.11: Maximum jet angle progression, Θ_{max} (deg), with increase in flap overlap

With an increased overlap, the increased Θ_{max} therefore had the effect of promoting BL separation at the wing TE, while the moderate increase in jet velocity did not provide a favourable pressure gradient of sufficient magnitude to keep the flow fully attached. With an increasing flap gap, not only did $\overline{V}_{jetmax}$ increase further by 5% thereby increasing the favourable pressure gradient magnitude, but Θ_{max} was reduced by 25%, and hence the wing TE BL remained attached.

The wake of the wing was finally analyzed using the global coordinate system at locations illustrated in Figure 7.12. When the wake progression of the main wing was analysed (Figures 7.13 and 7.14), the aforementioned effects were easily distinguished.

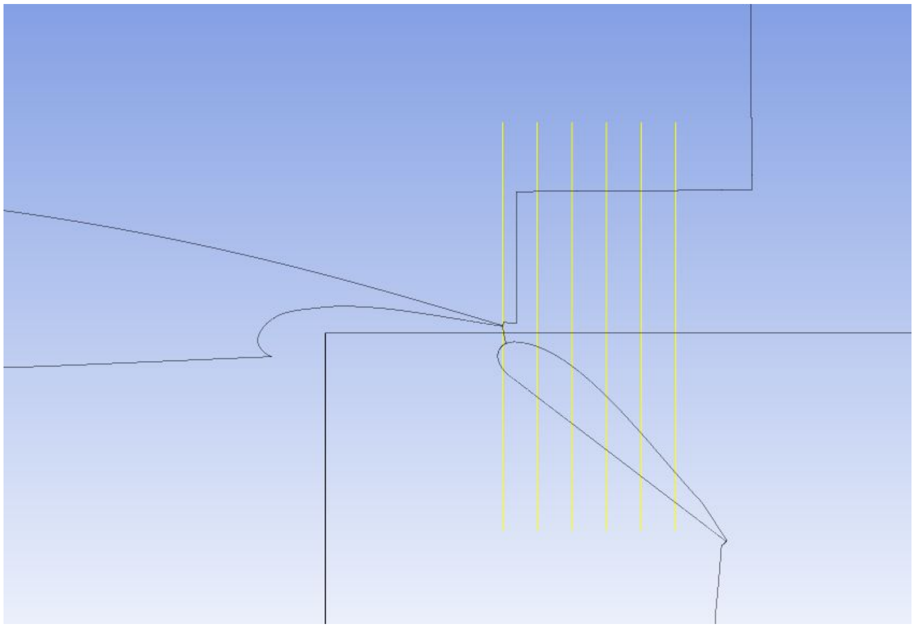

Figure 7.12: Yellow lines illustrate the locations used for wake analysis

With an increase in flap gap, the BL at the TE of the main wing displayed an improvement by developing a fuller velocity profile. In contrast, an increase in flap overlap resulted the deterioration of the BL towards separation at the wing TE due to the increased vertical velocity component of the slot flow which was evident in the increased slot flow angle. The slot flow adapted a jet-like character with an increased flap gap, the maximum jet velocity increased, and the flow retained its velocity profile further downstream. With an increased flap overlap, the slot flow also increased in

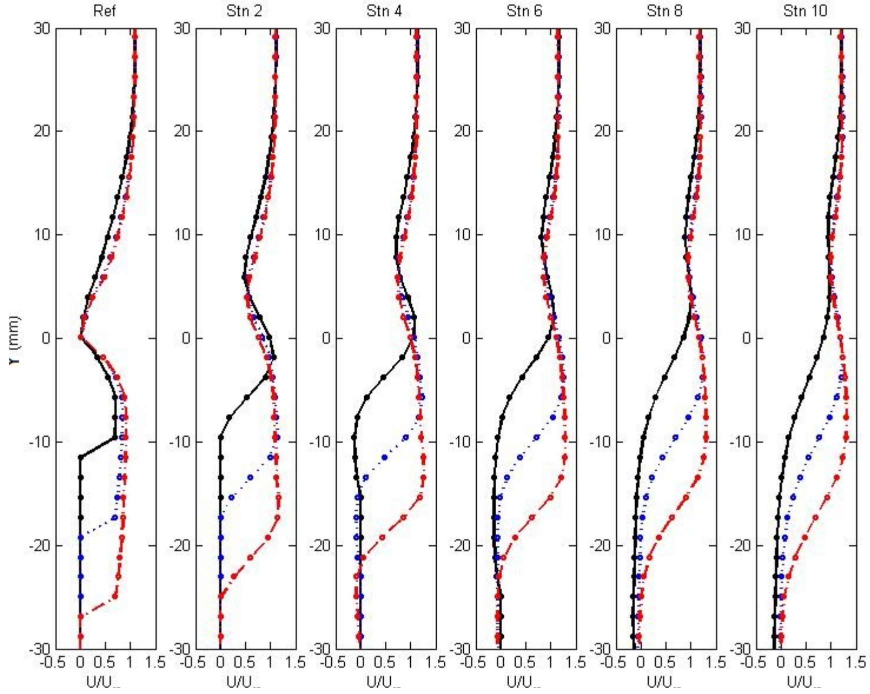

Figure 7.13: Wake velocity profiles, black = G0-O0, blue = G2-O0, red = G4-O0

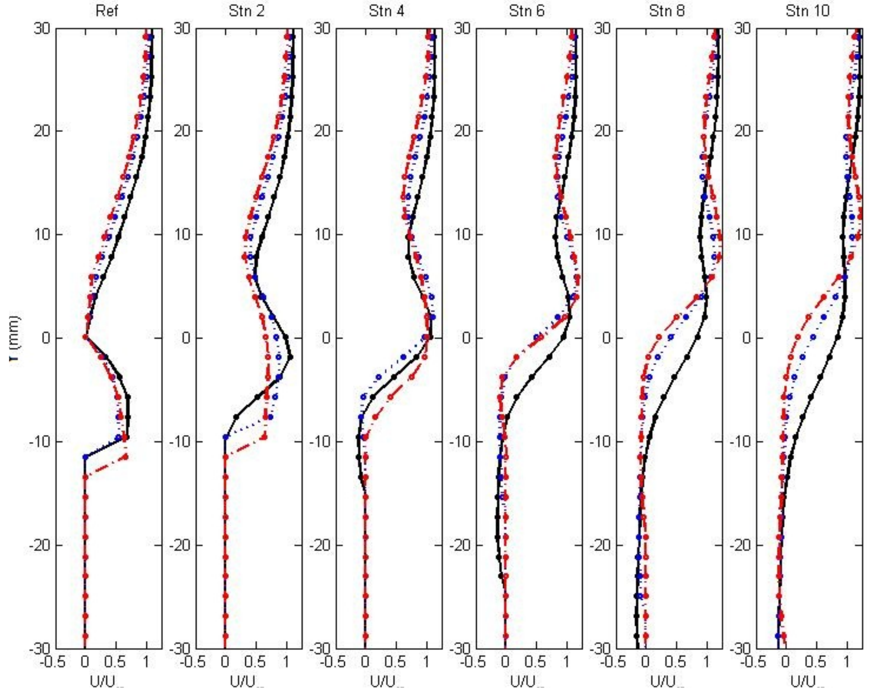

Figure 7.14: Wake velocity profiles, black = G0-O0, blue = G0-O2, red = G0-O4

magnitude, but the velocity profile was less defined further downstream. The significant increase in mixing with an increased overlap was explained by the aggressive confluence of the slot flow with the BL shed from the main wing due to the rapid vertical displacement of the slot flow. By the time the slot flow reached Station 6 in Figure 7.14, the slot flow had effectively obliterated any evidence of the BL shed from the wing TE located upstream. The difference in vertical translation of the slot flow in the overlap variation compared to the gap variation is clearly evident in Figures 7.13 and 7.14.

7.2 Pressure Data

In addition to the PIV measurements, pressure data was collected using a Scanivalve. It was anticipated that at least a partially attached flow would be recorded for the G0-O0 configuration, and the pressure distribution could thus be examined. Instead, it was found that the flow was massively separated for all configurations. The pressure data however was the first indication of an increase in the jet velocity with an increase in flap gap and overlap. The pressure measurements are shown as a function of flap gap and overlap in Figures 7.15 and 7.16 respectively.

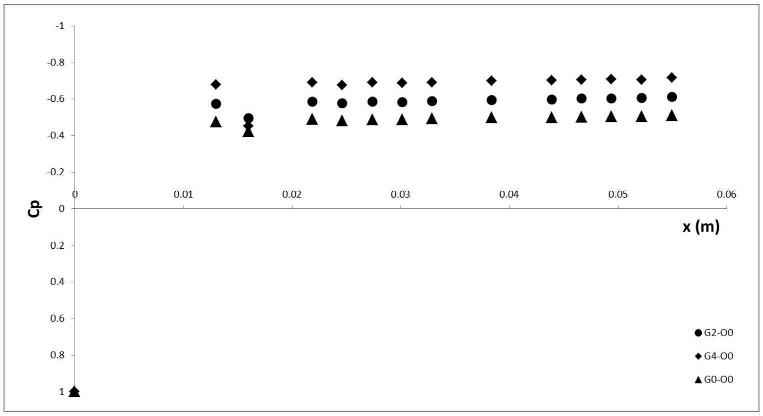

Figure 7.15: Gap variation effect on the C_p distribution along flap

Similar to the clean configuration analysis, the angle of attack variation of the landing configuration was also investigated. The BL over the main wing TE was

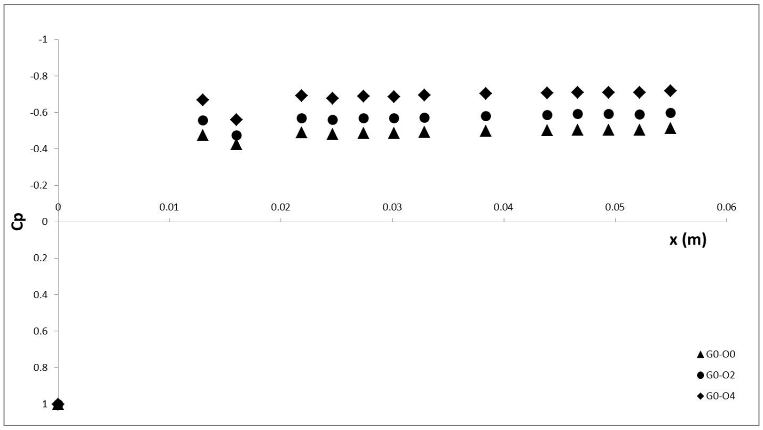

Figure 7.16: Overlap variation effect on the C_p distribution along flap

studied when subjected to an increasing angle of attack. The G0-O0 configuration first indicated BL separation at $\alpha = 10°$ near the wing TE ($x/c_w = 0.955$) with an $H \approx 3.9$. At $\alpha = 12°$, distinct BL separation was observed at $0.941c_w$. It should be noted that the wing chord of the landing configuration was still defined with the flap stowed. Therefore, the actual wing TE of the landing configuration was located at $0.955c_w$.

As observed with an increasing flap gap at $\alpha = 0°$, the wing BL of the G4-O0 configuration also displayed improvement at higher angles of attack. At $\alpha = 10°$, the BL of configuration G4-O0 remained essentially attached, with an $H \approx 3.0$ at the wing TE. At $\alpha = 12°$, the shape factor increased further, but BL separation was not evident.

With an increasing flap overlap however, the BL flow conditions quickly degraded with increasing angle of attack. Although only a small separation bubble was observed at $\alpha = 0°$ (as previously discussed), at $\alpha = 10°$ the wing TE BL separation location was recorded at $0.90c_w$. At $\alpha = 12°$, the separation location was no longer within the visible flow field ($x/c_w < 0.74$).

The BL velocity as well as TKE profiles of the configurations discussed can be found in Appendix A. While all the velocity and vorticity contours can be found in Appendix B and C respectively, Figures 7.17 , 7.18 and 7.19 illustrate the three configurations discussed above at $\alpha = 10°$.

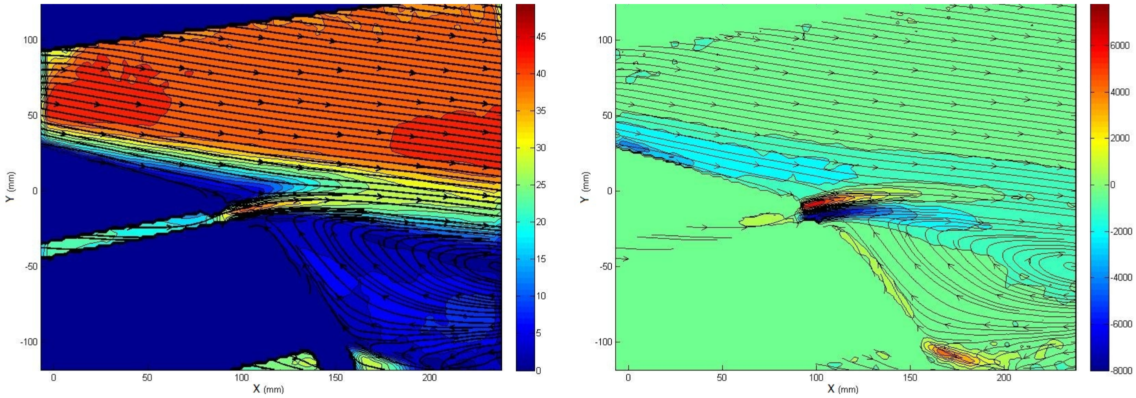

(a) (b)

Figure 7.17: G0-O0 configuration contours with streamlines at $\alpha = 10°$ (a) velocity, (b) mean spanwise vorticity

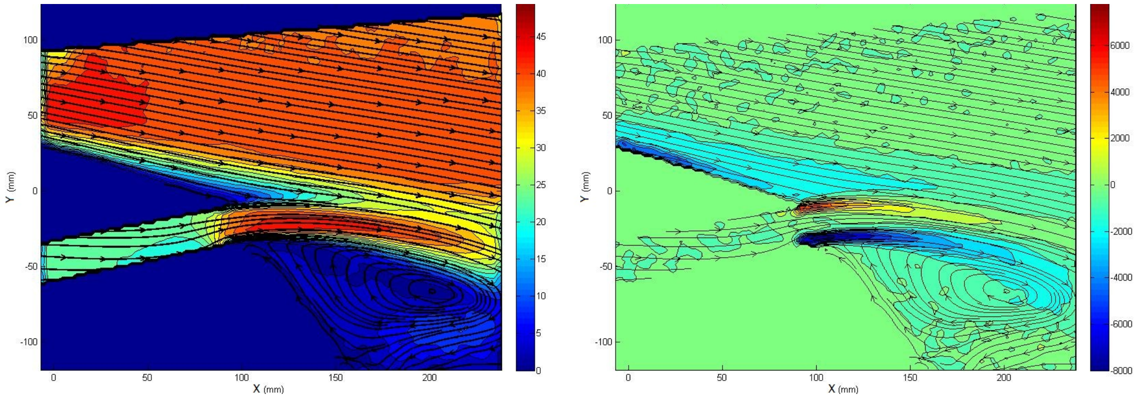

(a) (b)

Figure 7.18: G4-O0 configuration contours with streamlines at $\alpha = 10°$ (a) velocity, (b) mean spanwise vorticity

It was interesting to note that for configuration G4-O4, the detrimental effect of an increasing flap overlap on the wing BL was partially mitigated by the corresponding increase in flap gap, however, the effects were not linear, and the BL separation was still present at both $\alpha = 10°$ and $\alpha = 12°$. Flap pressure readings were not recorded for higher angles of attack.

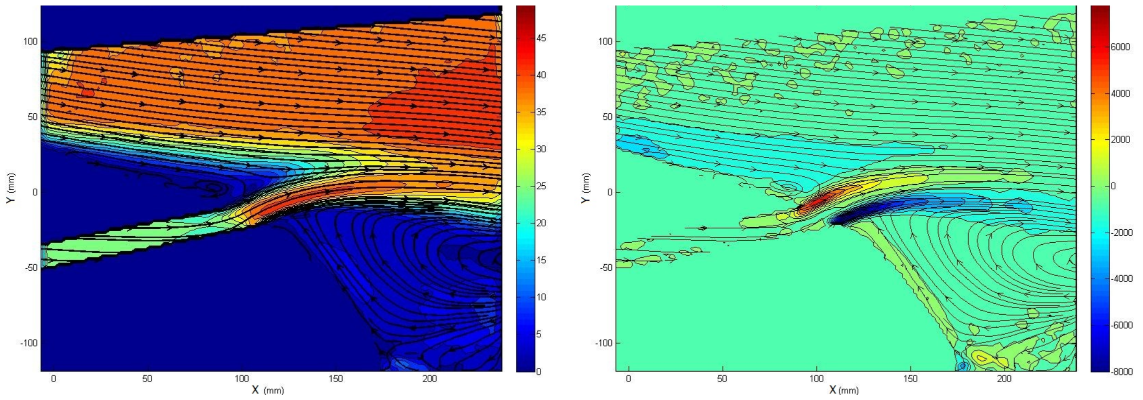

(a) (b)

Figure 7.19: G0-O4 configuration contours with streamlines at $\alpha = 10^\circ$ (a) velocity, (b) mean spanwise vorticity

Chapter 8

Conclusion

This work reports a numerical and experimental investigation on the effect of the variation of a Fowler flap gap and overlap on the aerodynamic performance of a CP-140 Aurora wing. The research was first conducted by computing 2D steady state solutions using RANS (Fluent 14.0), which was then followed by an experimental investigation employing a 2D PIV and pressure measurements. Two principal configurations were studied; the clean configuration consisting of the wing with the flap retracted and stowed, and the landing configuration with a flap deployed and deflected to 40°.

The clean configuration was investigated using both numerical and experimental methods over a range of angles of attack, α. The CFD solution was evaluated based on the ability of the CFD software to predict the correct separation location near the TE of the wing. It was found that all three turbulence models investigated (SA, SST, RSM) underpredicted flow separation. The first sign of flow separation was observed at $\alpha = 10^\circ$, at which point the simulations predicted separation location $\approx 0.05c_w$ further downstream in comparison to the experiment. At higher angles of attack however, this error grew rapidly; at $\alpha = 12^\circ$ the error increased to $0.07c_w$ and at $\alpha = 14^\circ$ the error grew to more than $0.15c_w$. The numerical solution of the landing configuration was found to be in disagreement with the experimental findings. Specifically, the magnitude of the flow emanating from the flap slot was over-predicted by the CFD by a factor of two. As a result, the CFD predicted flow over the flap remained attached, which was contradicted by experimental findings. In order to reconcile the CFD simulations with the experimental findings, a mesh was generated that permitted artificial control over the slot flow velocity magnitude and direction. Although the slot flow was estimated to have a uniform velocity profile due to relatively poor PIV resolution of the slot flow, this second set of simulations was in good agreement with the experimental data. Given an accurate slot flow velocity profile, further improvements in CFD to PIV agreement were possible, however the diffusive nature of the turbulence models employed in RANS simulations were also partially responsible for the CFD to PIV discrepancy. More importantly, since CFD simulations are often used with no knowledge of the flow, it was found that commercially available 2D steady state RANS CFD was incapable of accurately resolving the complex flow over a Fowler flap deployed and deflected to 40° without 'a priori' knowledge of boundary conditions.

The experimental investigation of the clean configuration validated the PIV experimental data as well as the CFD solutions. The mean spanwise vorticity contours confirmed that as long as the BL remained attached, the counter-clockwise wing TE vortex was of lower intensity. As the BL began to separate near the TE of the wing with increasing α, the magnitude of the wing TE vortex grew in magnitude.

The original intent behind the landing configuration investigation was to study the changes in flow over the flap. It was found however, that the flow over a flap deflected to 40° was massively separated for all flap gap and overlap configurations investigated. It has been reported in literature [109] [108] that at least a partially attached flow should result. This was explained by the choice of minimum flap gap and overlap investigated, G0-O0, which corresponded the maximum flap gap and overlap dimensions permitted by the manufacturer. As noted by Foster et al [28] and Wentz et al [106], if the flap gap and overlap were of sufficient size, the flow over the flap becomes increasingly separated. Clearly, configuration G0-O0 consisted of a flap gap and overlap of sufficient size to affect total flow separation over the deflected flap.

The focus of the investigation thus shifted to the BL on the TE of the main wing, which was immediately upstream of the slot flow. At $\alpha = 0°$, it was found that the increase in flap gap had a positive influence on the BL on the wing TE. By increasing the flap gap, the slot flow behaved more like a wall bounded jet, which induced a favourable pressure gradient, thereby improving the BL flow conditions upstream by inducing a fuller BL velocity profile.

Previously unknown details of the flow field became evident with the study of the slot flow. Given a minimum slot size, the slot flow behaved like a jet. An increase in flap gap had a beneficial effect on the upstream BL on the TE of the wing, which was reflected in a fuller BL velocity profile. An increase in flap overlap however, was found to have a negative effect on the upstream BL near the wing TE. This change in flow character was revealed through a close examination of the jet angle progression through the flow field. The trend of the jet flow was significantly different between the flap gap and overlap variations. With an increasing flap gap, the maximum angle of the jet decreased, thus almost becoming aligned with the upstream wing TE BL. With an increasing overlap, the maximum jet angle increased further, thus interfering with the development of the wing BL and hence promoting its separation. While no flow separation was found (at the TE of the main wing) at the manufacturer specified flap gap and overlap position, with an overlap increase of $0.04c_w$ beyond the manufacturer specified limits the wing TE BL developed a separation bubble.

The reason behind this increase in jet angle was found in the mean spanwise vorticity contours. As the flow passed through the slot, two counter-rotating vortices were generated by the wing TE and the flap LE. Hence, not only was the flow deflected up in order to avoid the physical presence of the flap, but the two counter-rotating vortices directed the jet flow through the slot and beyond. The relative position of those vortices remained vertical with a flap gap variation. As the flap was moved down with increasing gap, the flow angle decreased since the flap effectively moved out of the way of the flow. With an increasing flap overlap however, the two vortices were vertically offset, thus inducing a greater vertical velocity component to the jet flow thereby increasing the jet angle.

With a variation in angle of attack, similar trends were observed. The BL flow conditions at the wing TE improved with an increase in flap gap, while the flow conditions deteriorated towards separation with an increased overlap. It was interesting to note, that increasing the flap gap seemed to mitigate the detrimental effect of an increased overlap in configuration G4-O4.

8.1 Implications and Recommendations for Future Work

For the landing configuration, the implications of this research seemed to indicate that an increase in flap gap was not as detrimental to the flow field, as an increase in flap overlap. From an aircraft maintenance standpoint, the results indicated that although the ideal flap gap and overlap should be maintained to the manufacturer specifications for optimal aerodynamic performance, the variation in the flap overlap is more critical to the aerodynamic performance than the flap gap. This seems to be in contradiction to the work of Foster et al [28] as well as Wentz et al [106].

The present investigation focused on the increase in flap gap and overlap beyond the manufacturer limits. It is recommended that a similar study be conducted for a configuration consisting of smaller flap gap and overlap dimensions. Such an investigation may shed new light on the detailed flow behaviour of the complex flow field involving high lift devices.

The numerical component of this investigation did not include a 2D numerical simulation of the variation of the flap overlap with the artificially imposed jet boundary condition. This is seen as an excellent opportunity to further evaluate the accuracy of present day CFD RANS software.

Since this work investigated 2D flows exclusively, it is recommended that this study of high lift flows be extended into the 3D domain. 3D flow effects present a new range of flow features and numerical challenges which may elucidate this complex flow field further.

References

[1] C-12-140-000/tr-001 repair instructions cp140 aurora/cp140a arcturus structural volume 1.

[2] Lockheedd p-3 orion. urlhttp://ccxy.tripod.com/p3.html. Accessed: 2013-09-12.

[3] Ira H. Abbott and Albert E. Von Doenhoff. *Theory Of Wing Sections: Including A Summary Of Airfoil Data*. Dover Publications, 1959.

[4] Sgt. Anthony A. Adams. Personal Communication, February 2013.

[5] N. Alemdaroglu. Experimental investigation of flow around a multielement airfoil. *AGARD, High-Lift System Aerodynamics 19 p(SEE N 94-18415 04-01)*, 1993.

[6] M. Baragona, L.M. M. Boermans, M.J. L. van Tooren, H. Bijl, and Adriaan Beukers. Bubble bursting and stall hysteresis on single-slotted flap high-lift configuration. *AIAA journal*, 41(7):1230–1237, 2003.

[7] F. Bario, G. Charnay, and K.D. Papailiou. An experiment concerning the confluence of a wake and a boundary layer. *Journal of Fluids Engineering*, 104:18, 1982.

[8] Ali Benmeddour. Personal Communication, January 2013.

[9] A. Bertelrud, Sherylene Johnson, Carroll Lytle, and Carl Mills. A system for analysis of transition characteristics on a high-lift configuration at high reynolds numbers. In *Instrumentation in Aerospace Simulation Facilities, 1997. ICIASF'97 Record., International Congress on*, pages 141–152. IEEE, 1997.

[10] Kasim Biber. Stall hysteresis of an airfoil with slotted flap. *Journal of aircraft*, 42(6):1462–1470, 2005.

[11] Corey Bourassa, Flint O. Thomas, and Robert C. Nelson. A high-lift building block flow: Turbulent boundary layer relaminarization. *NASA Final Report*, 2001.

[12] Peter Bradshaw, Tuncer Cebeci, and James H Whitelaw. Engineering calculation methods for turbulent flow. *NASA STI/Recon Technical Report A*, 82:340, 1981.

[13] Bruno Chaouat. Reynolds stress transport modeling for high-lift airfoil flows. *AIAA journal*, 44(10):2390–2403, 2006.

[14] Scanivalve Corp. *ZOC 23B/32PxX2 Electronic Pressure Scanning Module Instruction and Service Manual.* Scanivalve Corp., 2005.

[15] L.F. Crabtree. *The Formation of Regions of Separated Flow on Wing Surfaces.* Aeronautical Research Council, 1959.

[16] Michael Cropper, George Postell, Mark Cording, Shane Dover, and Anthony Guillory. P-3b orion airborne laboratory experimenter handbook. Technical report, National Aeronautics and Space Administration, August 2010. 548-HDBK-0001.

[17] Russell M. Cummings, Scott A. Morton, and James R. Forsythe. Detached-eddy simulation of slat and flap aerodynamics for a high-lift wing. In *42nd Aerospace Sciences Meeting and Exhibit*, pages 1–14, 2004.

[18] Kyle C D. Knight, Eric M Braun, Christopher J Roy, Frank K Lu, and Joseph A Schetz. Interference drag modeling and experiments for a high-reynolds-number transonic wing. *Journal of Aircraft*, 49(6):1894–1903, 2012.

[19] Lars Davidson. Prediction of the flow around an airfoil using a reynolds stress transport model. *Journal of Fluids Engineering*, 117(1):50–57, 1995.

[20] TSI Inc. Fluid Mechanics Instrument Division. *IFA 300 Constant Temperature Anemometer System Instruction Manual.* TSI Inc., 2000.

[21] TSI Inc. Fluid Mechanics Instrument Division. *Air Velocity Transducer Model 8455/8465/8475 Operatin and Service Manual.* TSI Inc., 2011.

[22] Simha S Dodbele. Aiaa applied aerodynamics conference. In *Three Dimensional Aerodynamic Analysis of a High-Lift Transport Configuration.* AIAA, August 1993.

[23] Christian D. Edge and John N. Perkins. 13th aiaa applied aerodynamics conference. In *Three-Dimensional Aerodynamic Analysis of a Subsonic Transport High-Lift Configuration and Comparisons with Wind-Tunnel Test Results*, June 1995.

[24] Douvi C Eleni, Tsavalos I Athanasios, and Margaris P Dionissios. Evaluation of the turbulence models for the simulation of the flow over a national advisory committee for aeronautics (naca) 0012 airfoil. *Journal of Mechanical Engineering Research*, 4(3):100–111, 2012.

[25] H. Fellouah. *THERMAUS - Wind Tunnel Description.* Université de Sherbrooke, 2014.

[26] H. Fellouah, M. Ferchichi, and M.S. Guellouz. An experimental investigation on the effects of initial conditions on vortex shedding past a circular cylinder in the sub-critical regime. In *Proceedings of the 7th Intrenational Conference on Heat Transfer, Fluid Mechanics and Thermodynamics, Antalya, Turkey, July 2010*, 2010.

[27] Royal Canadian Air Force. Cp-140 aurora @ONLINE, August 2013.

[28] D.N. Foster, H.P.A.H. Irwin, and B.R Williams. *Two-Dimensional Flow around a Slotted Flap.* HM Stationery Office, 1970.

[29] M White Frank. *Viscous Fluid Flow.* McGraw-Hill, 3rd edition, 2006.

[30] Donald E. Gault and George B. McCullough. *Examples of Three Representative Types of Airfoil-section Stall at Low Speed.* National Advisory Committee for Aeronautics, 1951.

[31] Callum Gray. Personal Communication, November 2013.

[32] E Greff. In-flight measurement of static pressures and boundary-layer state with integrated sensors. *Journal of Aircraft*, 28(5):289–299, 1991.

[33] ANSYS FLUENT User's Guide. Release 14.0. ansys. *Inc., Canonsburg, PA*, 2010.

[34] Capt. Colin Harrison. Personal Communication, April 2013.

[35] H.P. Horton. *A semi-empirical theory for the growth and bursting of laminar separation bubbles.* HM Stationery Office, 1969.

[36] Saeed Jamei, Adi Maimun, Shuhaimi Mansor, Nor Azwadi, and Agoes Priyanto. Numerical investigation on aerodynamic characteristics of a compound wing-in-ground effect. *Journal of Aircraft*, 49(5):1297–1305, 2012.

[37] Donald W. Jasper, Shreekant Agrawal, and Brian A. Robinson. Navier-stokes calculations on multi-element airfoils using chimera-based solver. 1993.

[38] Adam Jirasek, Peter Eliasson, and Stefan Wallin. Computational study of the high-lift a-airfoil. *Journal of Aircraft*, 38(4):769–772, 2001.

[39] Kenneth M. Jones, Robert T. Biedron, and Mark Whitlock. 13th applied aerodynamics conference. In *Application of a Navier-Stokes Solver to the Analysis of Multielement Airfoils and Wing Using Multizonal Grid Techniques.* AIAA, 1995.

[40] Steven M Klausmeyer and John C Lin. *Comparative Results from a CFD Challenge over a 2D Three-Element High-Lift Airfoil.* National Aeronautics and Space Administration, 1997.

[41] G.K. Korbacher. Aerodynamics of powered high-lift systems. *Annual Review of Fluid Mechanics*, 6(1):319–358, 1974.

[42] Norbert Kroll, Cord-Christian Rossow, Klaus Becker, and Frank Thiele. The megaflow project. *Aerospace Science and Technology*, 4(4):223–237, 2000.

[43] LaVision. *DaVis 7.2 Software Manual.* LaVision GmbH, 2012.

[44] Xiaofeng Liu. A study of wake development and structure in constant pressure gradients. 2001.

[45] Nathan Logsdon and Gary Solbrekken. A procedure for numerically analyzing airfoils and wing sections. *University of Missouri*, pages 2–53, 2006.

[46] F.T. Lynch, R.C. Potter, and F.W. Spaid. Requirements for effective high lift cfd. In *ICAS, Congress, 2^{th}, Naples, Italy*, pages 1479–1482, 1996.

[47] Donovan L. Mathias, Karlin R. Roth, James C. Ross, Stuart E. Rogers, and Russell M. Cummings. Navier-stokes analysis of the flow about a flap edge. *Journal of Aircraft*, 35(6):833–838, 1998.

[48] Dimitri J. Mavriplis and S. Pirzadeh. Large-scale parallel unstructured mesh computations for 3d high-lift analysis. 1999.

[49] Robert J. McGhee and Gene J. Bingham. Low-speed aerodynamic characteristics of a 17-percent-thick supercritical airfoil section, including a comparison between wind-tunnel and flight data. 1972.

[50] Catherine B. McGinley, Luther N. Jenkins, Ralph D. Watson, and Arild Bertelrud. 3-d high-lift flow-physics experiment–transition measurements. *AIAA Paper*, 5148:2005, 2005.

[51] PT Meredith. Viscous phenomena affecting high-lift systems and suggestions for future cfd development. *AGARD, High-Lift System Aerodynamics 8 p(SEE N 94-18415 04-01)*, 1993.

[52] F. Moens, J. Perraud, A. Séraudie, and R. Houdeville. Transition measurement and prediction on a generic high-lift swept wing. *Proceedings of the Institution of Mechanical Engineers, Part G: Journal of Aerospace Engineering*, 220(6):589–603, 2006.

[53] Frédéric Moens, Jean Perraud, Andreas Krumbein, Thomas Toulorge, Pierluigi Iannelli, Peter Eliasson, and Ardeshir Hanifi. Transition prediction and impact on 3d high-lift wing configuration. In *AIAA 25th Applied Aerodynamics Conference*, pages 25–28, 2007.

[54] A. Moghadam and L.C. Squire. The mixing of three-dimensional turbulent wakes and boundary layers. *Aeronautical Journal*, 93(925):153–161, 1989.

[55] Anutosh Moitra. Automated cfd analysis of two-dimensional high-lift flows. *Journal of aircraft*, 39(4):662–667, 2002.

[56] Thomas Morel and T. Paul Torda. Calculation of free turbulent mixing by the interaction approach. *AIAA Journal*, 12(4):533–540, 1974.

[57] Mitsuhiro Murayama, Taro Imamura, Kazuomi Yamamoto, and Kunihiko Kobayashi. Comparison of reynolds-averaged navier-stokes simulations of multi-element high-lift configurations. *Journal of Aircraft*, 44(1):175–186, 2007.

[58] Mitsuhiro Murayama, Zhong Lei, Junichi Mukai, and Kazuomi Yamamoto. Cfd validation for high-lift devices: Three-element airfoil. *Transactions of the Japan Society for Aeronautical and Space Sciences*, 49(163):40–48, 2006.

[59] Mitsuhiro Murayama, Zhong Lei, Keizo Takenaka, and Kazuomi Yamamoto. Cfd validation for high-lift devices: Two-element airfoil. *Transactions of the Japan Society for Aeronautical and Space Sciences*, 49(163):31–39, 2006.

[60] Mitsuhiro Murayama and Kazuomi Yamamoto. Numerical simulation of high lift configurations using unstructured mesh method. *Proceedings of 24th ICAS*, 2004.

[61] Mitsuhiro Murayama, Kazuomi Yamamoto, and Kunihiko Kobayashi. Validation of computations around high lift configurations by structured and unstructured mesh. *Journal of Aircraft*, 43(2):395–406, 2006.

[62] The University of Kansas. Three-element wing @ONLINE, October 2013.

[63] E. Omar, T. Zierten, and A. Mahal. Two-dimensional wind-tunnel tests of a nasa supercritical airfoil with various high-lift systems. 1973.

[64] P.R. Owen and L. Klafner. *On the Laminar Boundary Layer Separation from the Leading Edge of a Thin Aerofoil.* Aeronautical Research Council, 1955.

[65] K. Paschal, L. Jenkins, and C. Yao. Unsteady slat-wake characteristics of a high-lift configuration. *AIAA paper*, 139:2000, 2000.

[66] Ugo Piomelli. Turbulence simulations. University Lecture, 2012.

[67] Ugo Piomelli, Meelan M. Choudhari, Victor Ovchinnikov, and Elias Balaras. Numerical simulation of wake/boundary layer interactions. In *AIAA 41th Aerospace Sciences Meeting and Exhibit*, pages 1–12, 2003.

[68] Robert C. Platt. *Aerodynamic Characteristics of a Wing with Fowler Flaps including Loads, Downwash, and Calculated Effect on Take-Off.* National Advisory Committee for Aeronautics, 1935.

[69] Robert C. Platt. *Aerodynamic Characteristics of Wings with Cambered External-Airfoil Flaps, Including Lateral Control with a Full Span Flap.* National Advisory Committee for Aeronautics, 1935.

[70] Alan Pope and William H. Rae. *Low Speed Wind Tunnel Testing.* Wiley, 1954.

[71] Daniel Reckzeh. Aerodynamic design of airbus high-lift wings in a multidisciplinary environment. In P Neittaanmäki, T Rossi, S Korotov, E Oñate, J Périaux, and D Knörzer, editors, *European Congress on Computatinoal Methods in Applied Sciences and Engineering.*

[72] Dasia A. Reyes, Sharat S. Girimaji, Mohagan J. Pandya, and Khaled S. Abdol-Hamid. Computations of high lift wing configuration on unstructured grids using k-ω models. *Journal of Aircraft*, 50(6):1–14, 2013.

[73] Stuart E Rogers, FR Menter, Paul A Durbin, and Nagi N Mansour. A comparison of turbulence models in computing multi-element airfoil flows. *AIAA paper*, 94:0291, 1994.

[74] Stuart E Rogers, Karlin Roth, Hoa V Cao, Jeffrey P Slotnick, Mark Whitlock, Steven M Nash, and M David Baker. Computation of viscous flow for a boeing 777 aircraft in landing configuration. *Journal of Aircraft*, 38(6):1060–1068, 2001.

[75] Cord-Christian Rossow, Norbert KrollL, and Dieter Schwamborn. Numerical aerodynamics at dlr. *Chinese Journal of Aeronautics*, 19(2):134–150, 2006.

[76] R. Rudnik, P. Eliasson, and J. Perraud. Evaluation of cfd methods for transport aircraft high lift systems. *Aeronautical Journal*, 109(1092):53–64, 2005.

[77] R. Rudnik and E. Germain. Reynolds number scaling effects on the european high-lift configurations. *Journal of Aircraft*, 46(4):1140–1151, 2009.

[78] R. Rudnik, S. Melber, A. Ronzheimer, and O. Brodersen. Three-dimensional navier-stokes simulations for transport aircraft high-lift configurations. *Journal of Aircraft*, 38(5):895–903, 2001.

[79] R. Rudnik, D. Reckzeh, and J. Quest. Hinva-high lift inflight validation-project overview and status. *AIAA Paper*, 106:27, 2012.

[80] Ralf Rudnik. European high lift programme ii. Technical Report AST3-CT04-502896.

[81] Ralf Rudnik. Stall behaviour of the eurolift high lift configurations. *AIAA paper*, 836:30, 2008.

[82] Christopher L Rumsey and Thomas B Gatski. Recent turbulence model advances applied to multielement airfoil computations. *Journal of Aircraft*, 38(5):904–910, 2001.

[83] Christopher L Rumsey, Thomas B Gatski, Susan X Ying, and Arild Bertelrud. Prediction of high-lift flows using turbulent closure models. *AIAA Journal*, 36:765–774, 1998.

[84] Christopher L. Rumsey, Elizabeth M. Lee-Rausch, and Ralph D. Watson. Three-dimensional effects in multi-element high lift computations. *Computers & fluids*, 32(5):631–657, 2003.

[85] Christopher L Rumsey and Susan X Ying. Prediction of high lift: Review of present cfd capability. *Progress in Aerospace Sciences*, 38(2):145–180, 2002.

[86] C Sarraf, R Jaouen, H Djeridi, and JY Billard. Investigation of thickness effects on 2d naca symmetric foils. In *Oceans 2005-Europe*, volume 2, pages 1298–1303. IEEE, 2005.

[87] Herrmann Schlichting and Klaus Gersten. *Boundary-layer theory*. Springer, 2000.

[88] A. Séraudie, J. Perraud, and F. Moens. Transition measurement and analysis on a swept wing in high lift configuration. *Aerospace Science and Technology*, 7(8):569–576, 2003.

[89] A.M.O. Smith. High-lift aerodynamics. *Journal of Aircraft*, 12(6):501–530, 1975.

[90] Frank W. Spaid. High reynolds number, multielement airfoil flowfield measurements. *Journal of Aircraft*, 37(3):499–507, 2000.

[91] Philippe R Spalart. Detached-eddy simulation. *Annual Review of Fluid Mechanics*, 41:181–202, 2009.

[92] L.C. Squire. Interactions between wakes and boundary-layers. *Progress in Aerospace Sciences*, 26(3):261–288, 1989.

[93] L.C. Squire and D. Agoropoulos. Interactions between turbulent wakes and boundary layers. *AIAA journal*, 26(10):1194–1200, 1988.

[94] L.C. Squire and De Ming Zhou. The interaction of a wake with a turbulent boundary layer. *Aeronautical Journal*, 89(882):72–81, 1985.

[95] W.A. Stevens, S.H. Goradia, and J.A. Braden. Mathematical model for two-dimensional multi-component airfoils in viscous flow. 1971.

[96] K. Takeda, G.B. Ashcroft, X. Zhang, and P.A. Nelson. Unsteady aerodynamics of slat cove flow in a high-lift device configuration. *AIAA paper*, 706:2001, 2001.

[97] J.J. Thibert. The garteur high lift research programme. In *AGARD CONFERENCE PROCEEDINGS AGARD CP*, pages 16–16. AGARD, 1993.

[98] J.J. Thibert, J. Reneaux, F. Moens, and J. Preist. Onera activities on high-lift devices for transport aircraft. *Aeronautical Journal*, 99(989):395–411, 1995.

[99] Peter Thiede. Eurolift-advanced high lift aerodynamics for transport aircraft. *Air & Space Europe*, 3(3):105–108, 2001.

[100] Flint O. Thomas, R.C. Nelson, and X. Liu. Experimental investigation of the confluent boundary layer of a high-lift system. *AIAA Journal*, 38(6):978–988, 2000.

[101] C.P. Van Dam, S.M. Los, S.J. Miley, V.E. Roback, L.P. Yip, A. Bertelrud, and P.M.H.W. Vijgen. In-flight boundary-layer state measurements on a high-lift system: Main element and flap. *Journal of aircraft*, 34(6):748–756, 1997.

[102] C.P. Van Dam, S.M. Los, S.J. Miley, V.E. Roback, L.P. Yip, A. Bertelrud, and P.M.H.W. Vijgen. In-flight boundary-layer state measurements on a high-lift system: Slat. *Journal of aircraft*, 34(6):748–756, 1997.

[103] J.W. vn der Burg, H. Freiherr Von Geyr, R. Heinrich, P. Eliasson, T. Delille, and J. Krier. Geometrical installation and deformation effects in high-lift flows. *AIAA Journal*, 47(1):60–70, 2009.

[104] Fred E. Weick and Robert C. Platt. *Wind-Tunnel Tests of the Fowler Variable-Area Wing*. National Advisory Committee for Aeronautics, 1932.

[105] Fred E. Weick and Robert C. Platt. *Wind-Tunnel Tests on Model Wing With Fowler Flap and Specially Developed Leading-Edge Slot*. National Advisory Committee for Aeronautics, 1933.

[106] W.H. Wentz and C. Ostowari. Additional flow field studies of the ga(w)-1 airfoil with 30-percent chord fowler flap inscluding slot-gap variations and cove shape modifications. 1983.

[107] W.H. Wentz and H.C. Seetharam. Development of a fowler flpa system for a high performance general aviation airfoil. 1974.

[108] W.H. Wentz and H.C. Seetharam. A low speed two-dimensional study of flow separation on the ga(w)-1 airfoil with 30% chord fowler flap. 1977.

[109] William H Wentz. Wind tunnel tests of the ga (w)-2 airfoil with 20% aileron, 25% slotted flap, 30% fowler flap and 10% slot-lip spoiler. 1976.

[110] Carl J. Wenzinger and Walter B. Anderson. *Pressure Distribution Over Airfoils with Fowler Flaps*. National Advisory Committee for Aeronautics, 1938.

[111] Carl J. Wenzinger and Thomas A. Harris. *Wind-Tunnel Investigation of an NACA23012 Airfoil with Various Arrangements of Slotted Flaps*. National Advisory Committee for Aeronautics, 1939.

[112] Jochen Wild, Joel Brezillon, Olivier Amoignon, Jürgen Quest, Frederic Moens, and Domenico Quagliarella. Advanced high-lift design by numerical methods and wind tunnel verification within the european project eurolift ii. *Journal of Aircraft*, 46:157–167, 2009.

[113] Susan X. Ying, Frank W. Spaid, Catherine B. McGinley, and Christopher L. Rumsey. Investigation of confluent boundary layers in high-lift flows. *Journal of Aircraft*, 36(3):550–562, 1999.

[114] Long P. Yip, Paul M.H.W. Vijgen, Jay D. Hardin, and C.P. Vandam. In-flight pressure distributions and skin-friction measurements on a subsonic transport high-lift wing section. 1993.

[115] L.P. Yip, C.P. van Dam, J.H. Whitehead, J.D. Hardin, S.J. Miley, R.C. Potter, A. Bertelrud, D.C. Edge, and P.E. Willard. The nasa b737-100 high-lift flight research programme: Measurement and computations. *Aeronautical Journal*, 99(989):372–386, 1995.

[116] A.D. Young. *The Induced Drag of Flapped Elliptic Wings with Cut-out and with Flaps that Extend the Local Chord*. Aeronautical Research Council, 1951.

[117] Alec David Young. *The Aerodynamic Characteristics of Flaps.* 1947.

[118] Marian Zabloudil, Zdeněk Pátek, and Petr Vrchota. 27^th international congress of the aeronautical sciences. In *Wind Tunnel Investigation of Flowfield on the Fowler Flap and in the Cove Using PIV Method*, September 2010.

Appendix A

Landing configuration velocity and TKE profiles

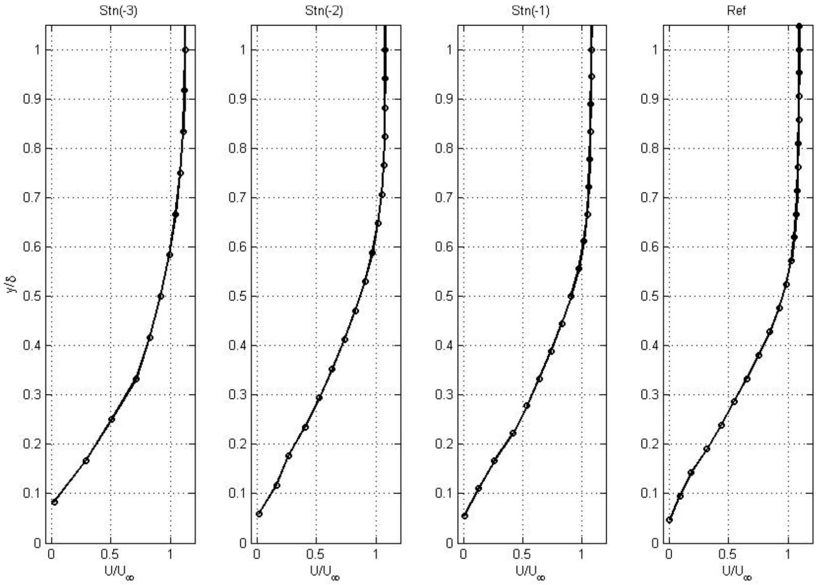

Figure A.1: Velocity profiles of configuration G0-O0 at $\alpha = 0^{\circ}$

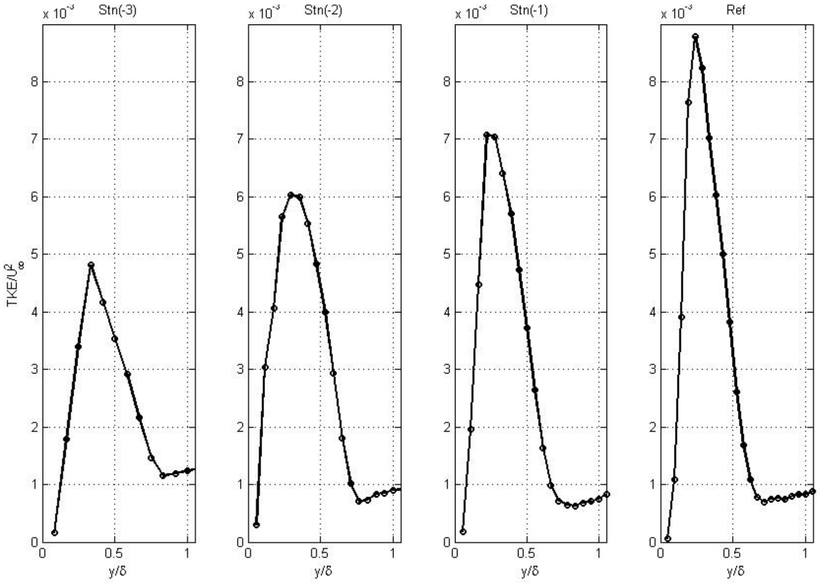

Figure A.2: TKE profiles of configuration G0-O0 at $\alpha = 0^{\circ}$

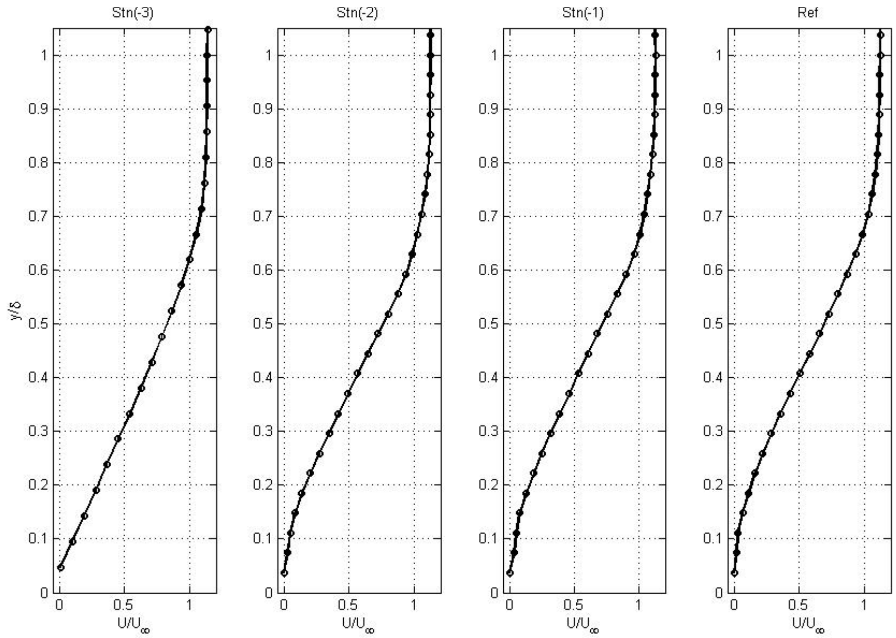

Figure A.3: Velocity profiles of configuration G0-O0 at $\alpha = 10^\circ$

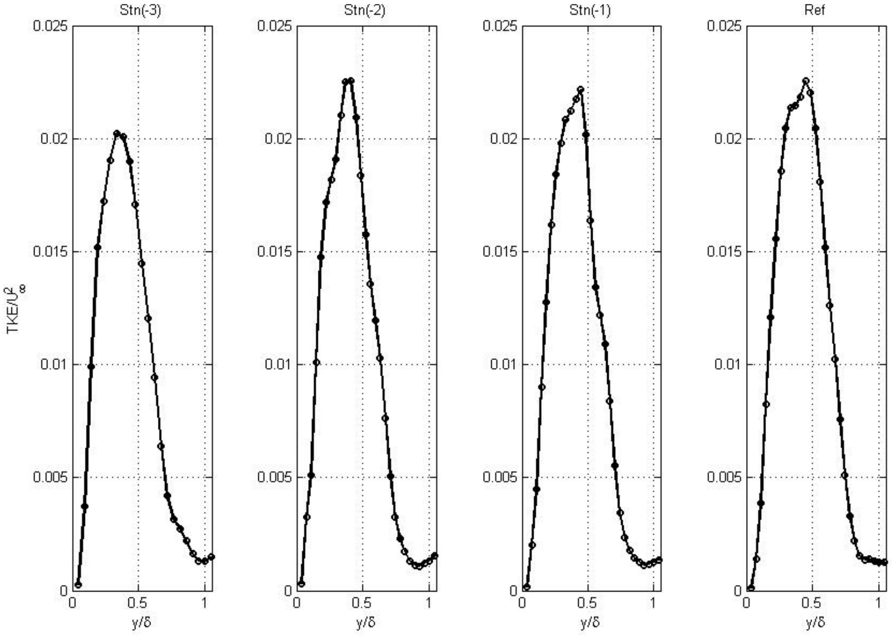

Figure A.4: TKE profiles of configuration G0-O0 at $\alpha = 10^\circ$

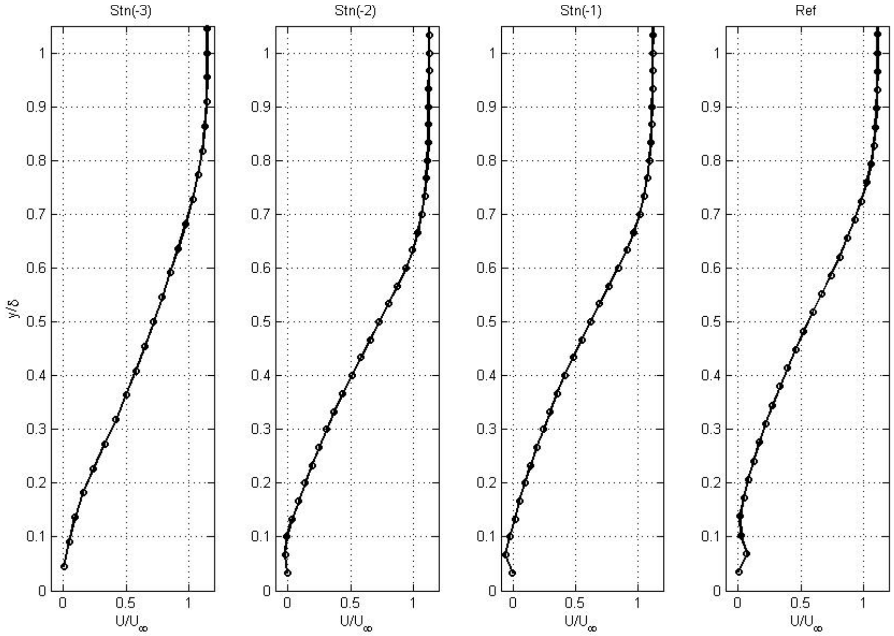

Figure A.5: Velocity profiles of configuration G0-O0 at $\alpha = 12^{\circ}$

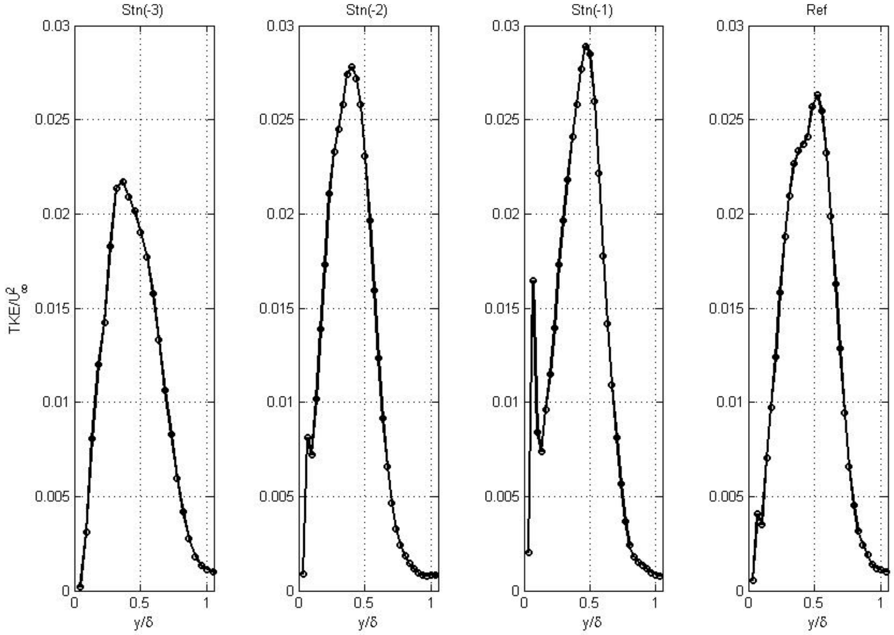

Figure A.6: TKE profiles of configuration G0-O0 at $\alpha = 12^{\circ}$

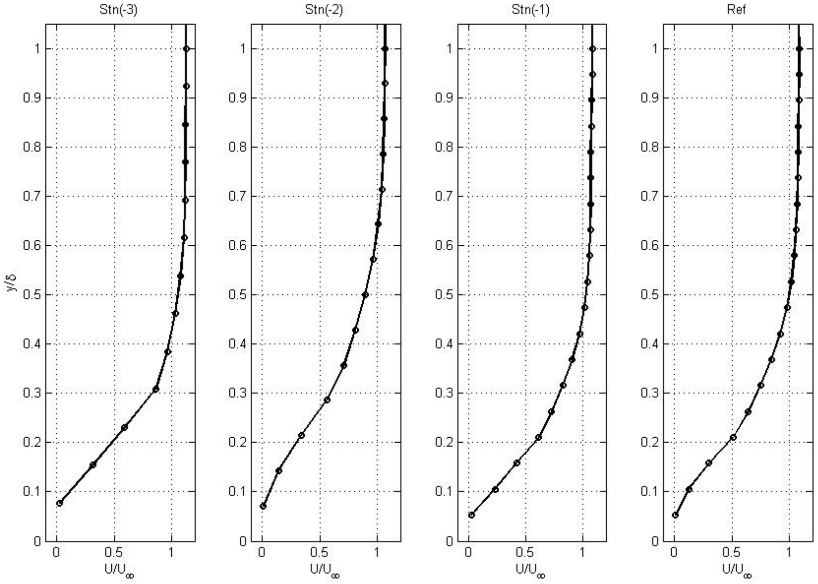

Figure A.7: Velocity profiles of configuration G4-O0 at $\alpha = 0^\circ$

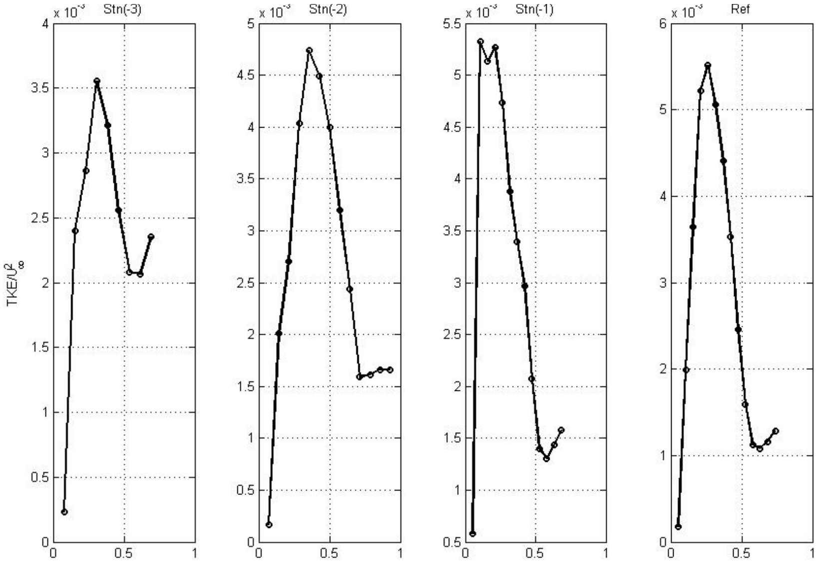

Figure A.8: TKE profiles of configuration G4-O0 at $\alpha = 0^\circ$

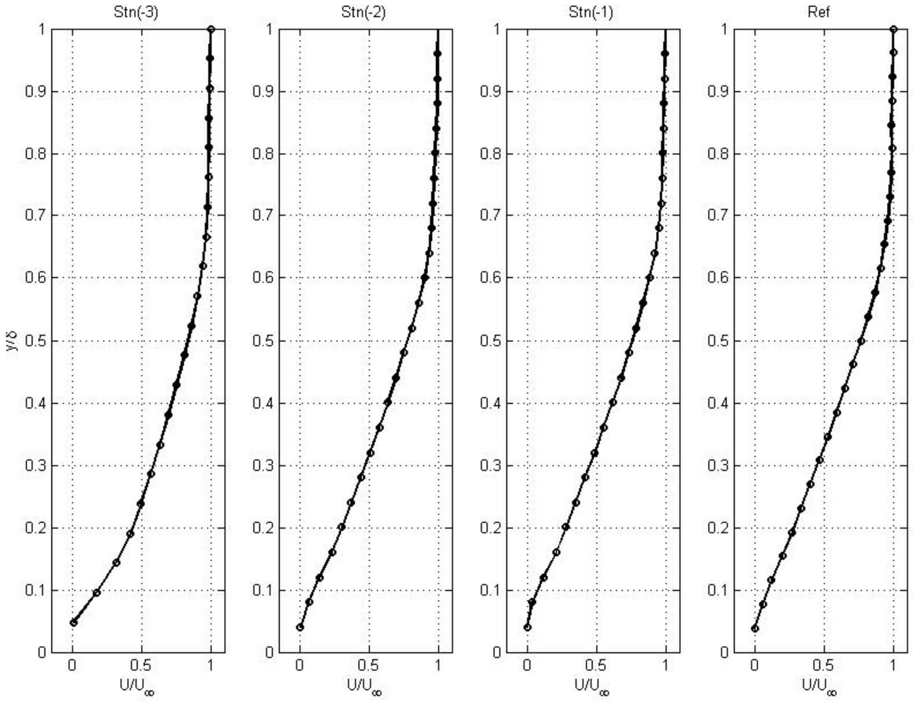

Figure A.9: Velocity profiles of configuration G4-O0 at $\alpha = 10^\circ$

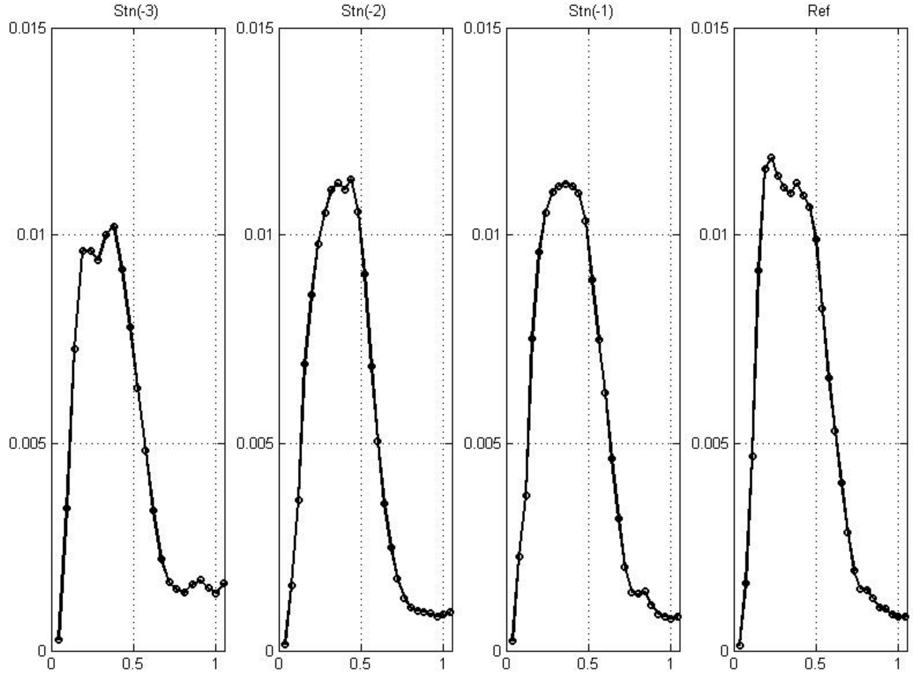

Figure A.10: TKE profiles of configuration G4-O0 at $\alpha = 10^\circ$

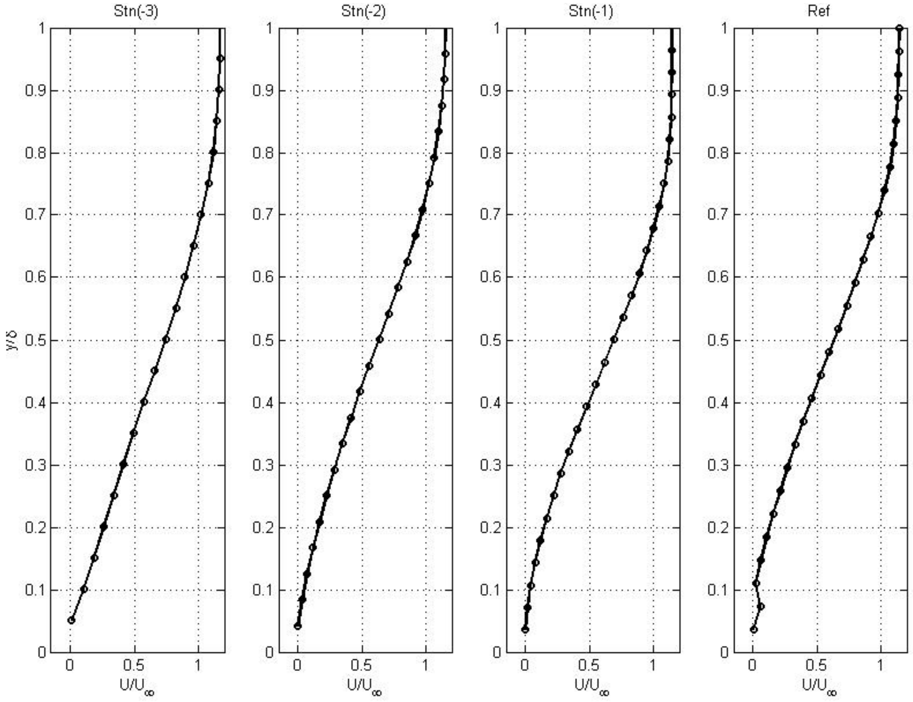

Figure A.11: Velocity profiles of configuration G4-O0 at $\alpha = 12^\circ$

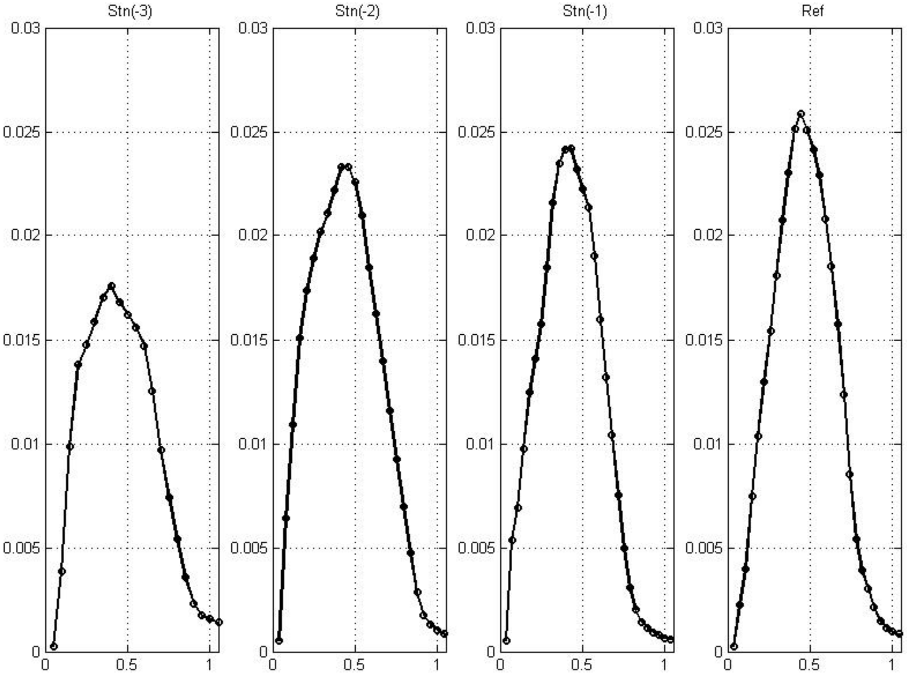

Figure A.12: TKE profiles of configuration G4-O0 at $\alpha = 12^\circ$

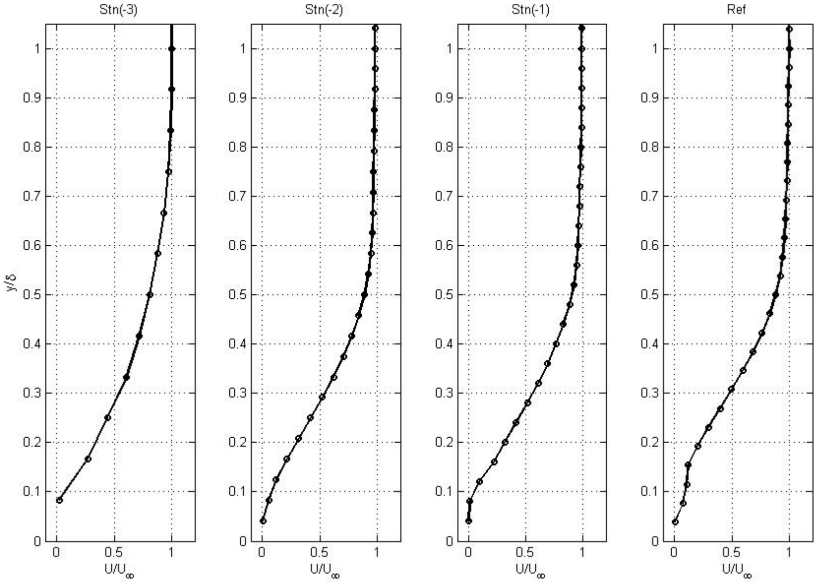

Figure A.13: Velocity profiles of configuration G0-O4 at $\alpha = 0°$

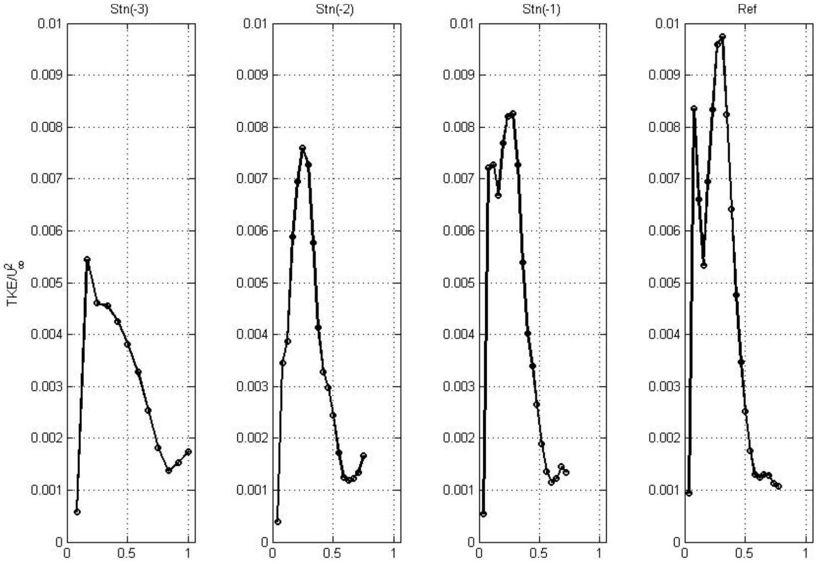

Figure A.14: TKE profiles of configuration G0-O4 at $\alpha = 0°$

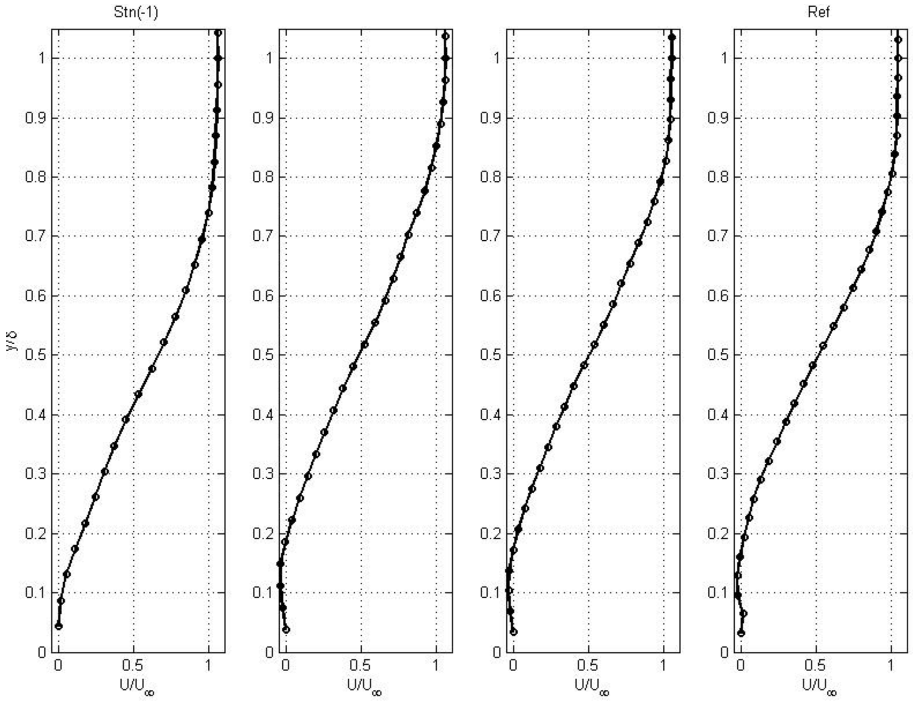

Figure A.15: Velocity profiles of configuration G0-O4 at $\alpha = 10^\circ$

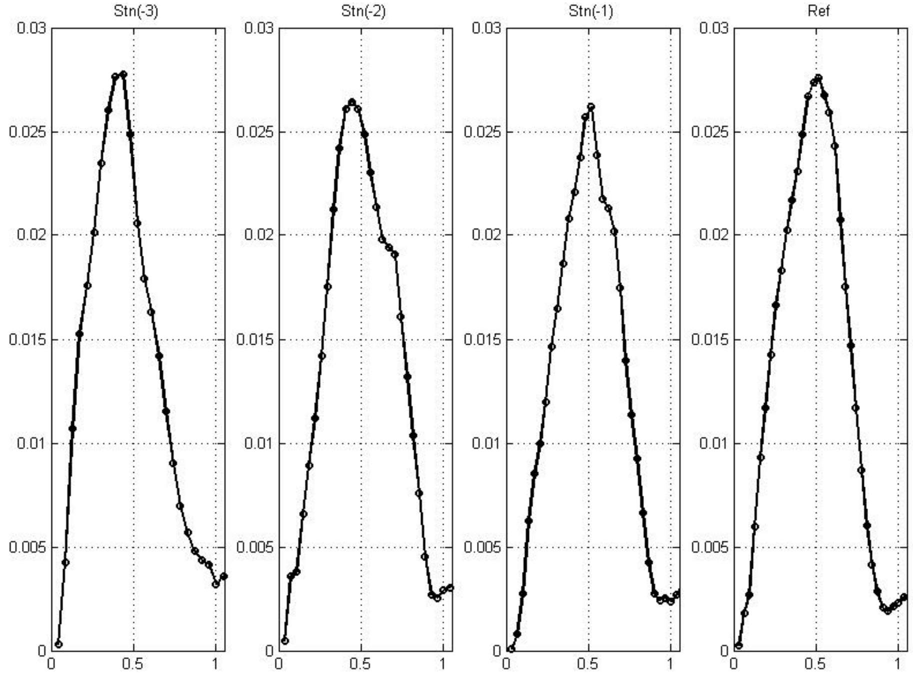

Figure A.16: TKE profiles of configuration G0-O4 at $\alpha = 10^\circ$

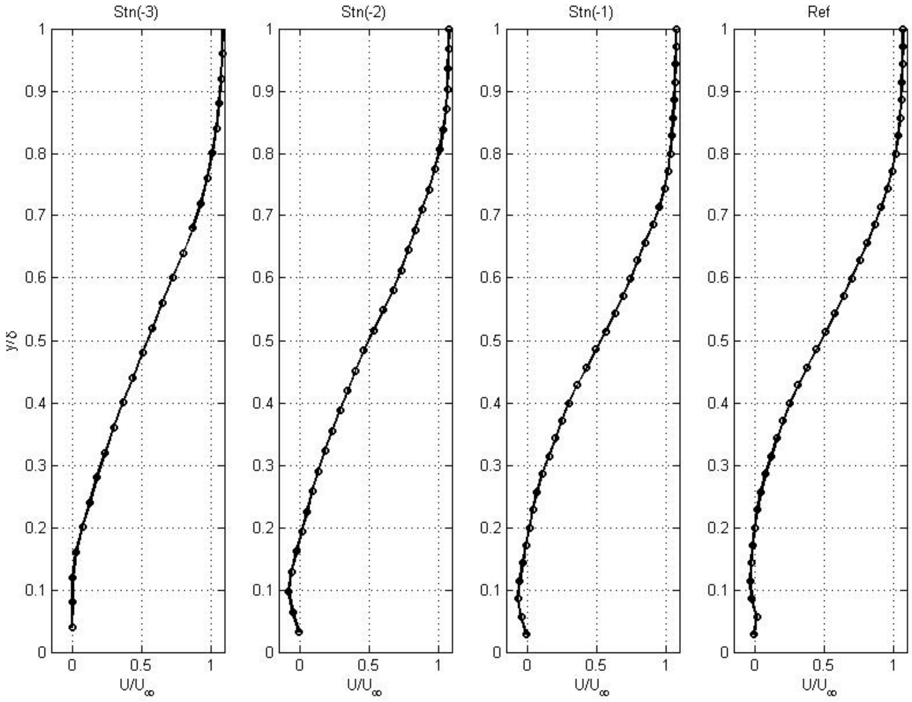

Figure A.17: Velocity profiles of configuration G0-O4 at $\alpha = 12^\circ$

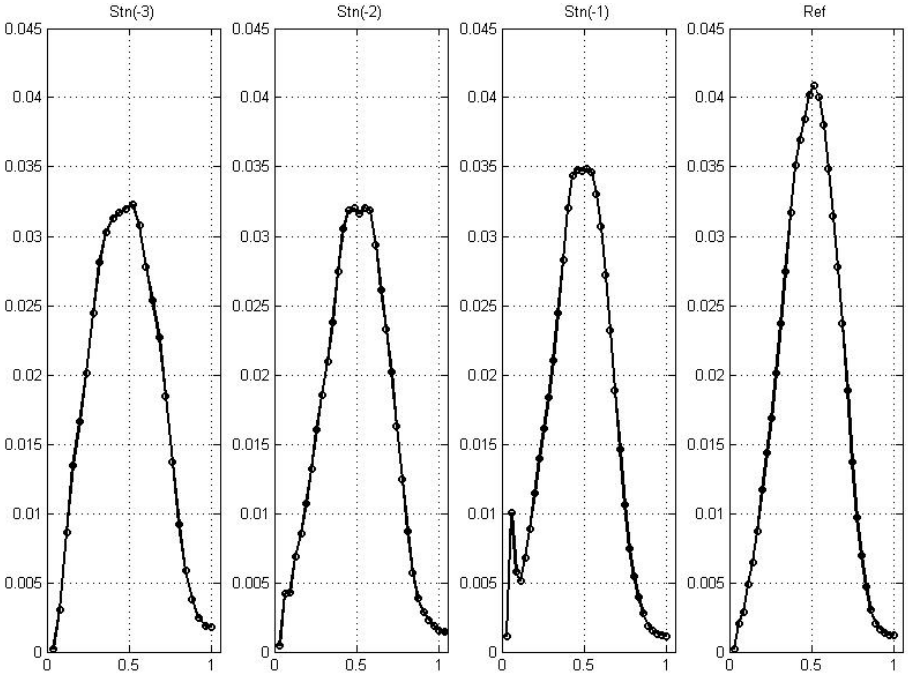

Figure A.18: TKE profiles of configuration G0-O4 at $\alpha = 12^\circ$

Appendix B

Landing configuration velocity contours and streamlines

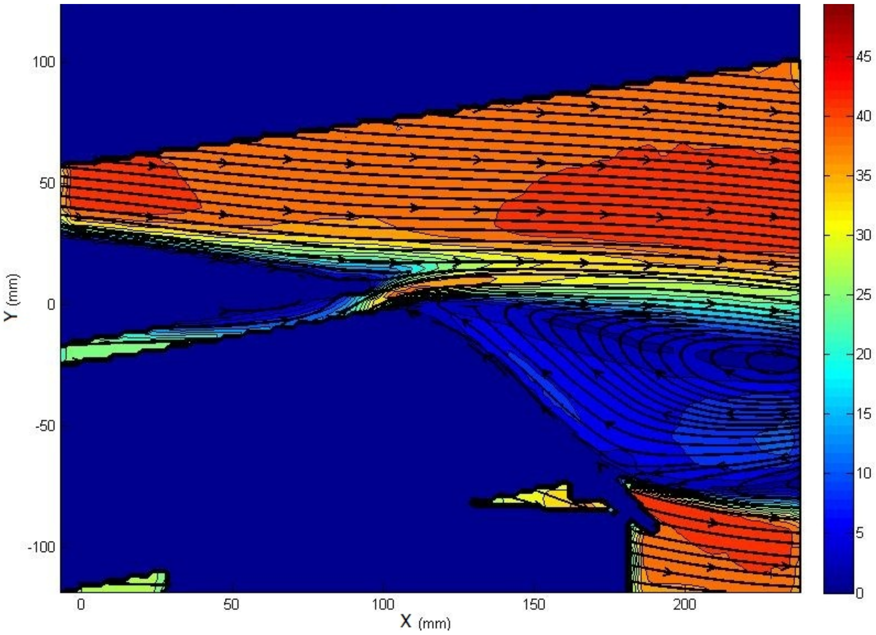

Figure B.1: Velocity contours and streamlines of configuration G0-O0 at $\alpha = 0^\circ$

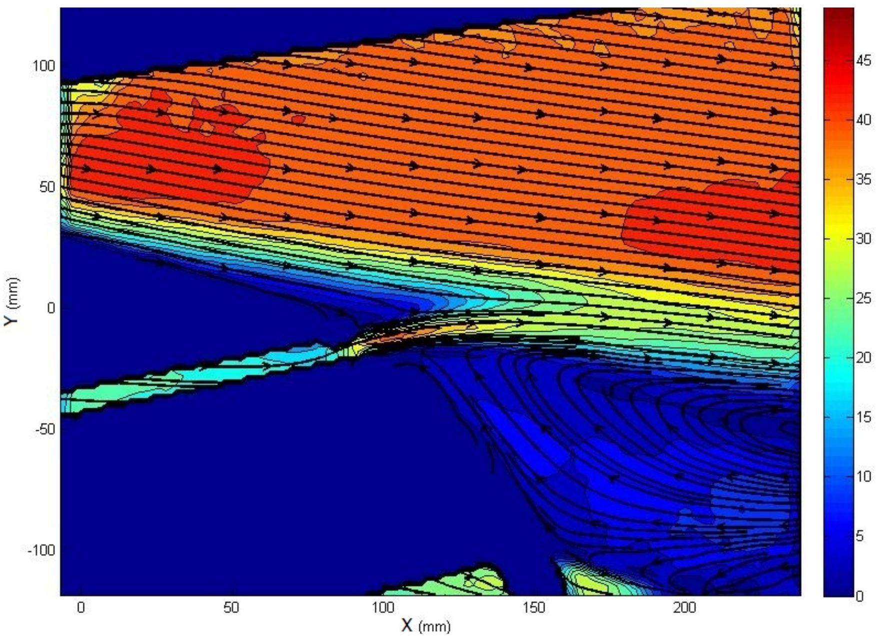

Figure B.2: Velocity contours and streamlines of configuration G0-O0 at $\alpha = 10^{\circ}$

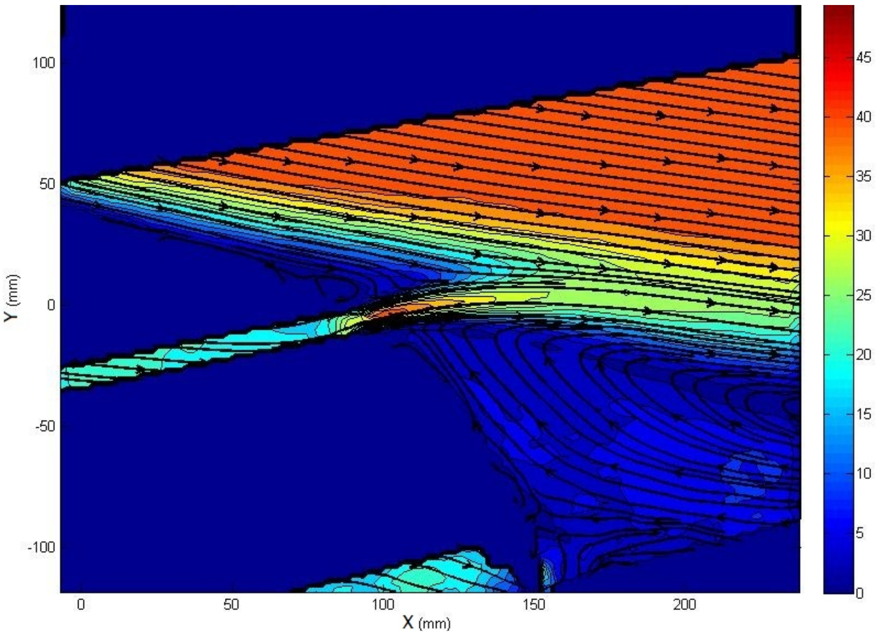

Figure B.3: Velocity contours and streamlines of configuration G0-O0 at $\alpha = 12^{\circ}$

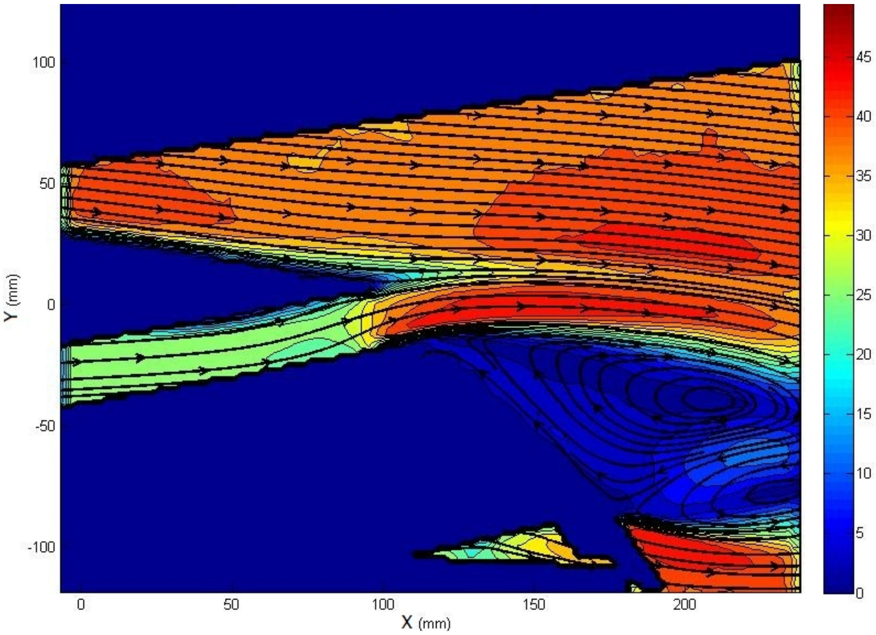

Figure B.4: Velocity contours and streamlines of configuration G4-O0 at $\alpha = 0^\circ$

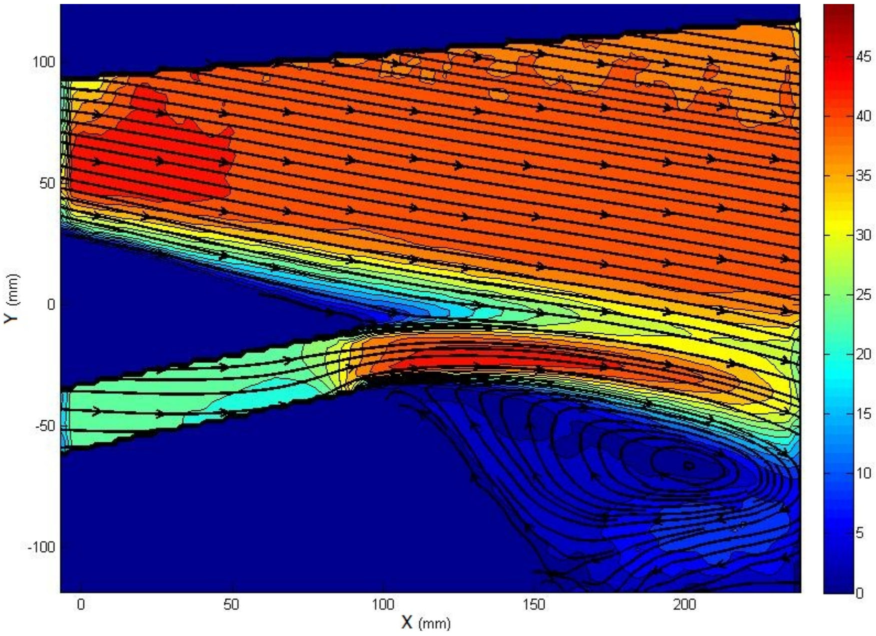

Figure B.5: Velocity contours and streamlines of configuration G4-O0 at $\alpha = 10^\circ$

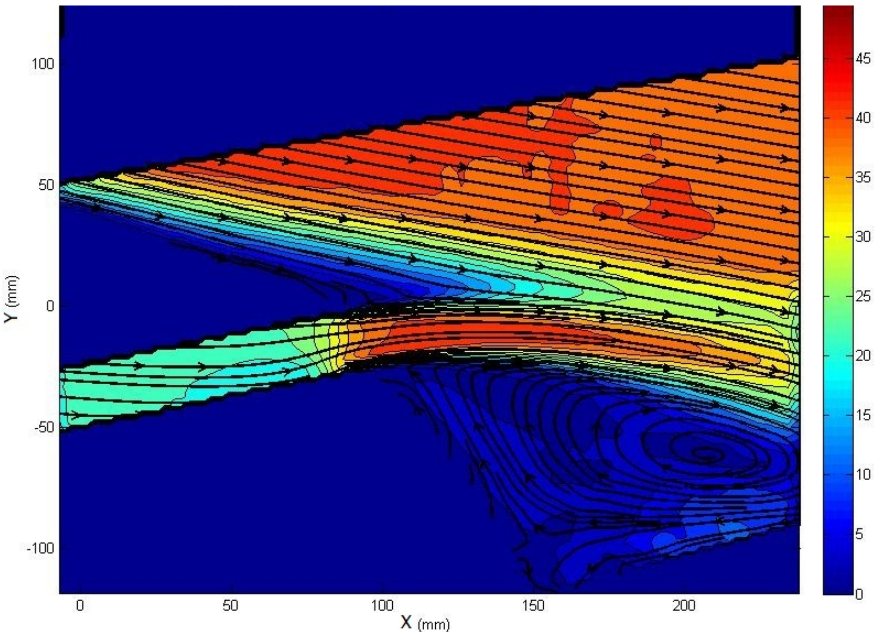

Figure B.6: Velocity contours and streamlines of configuration G4-O0 at $\alpha = 12^\circ$

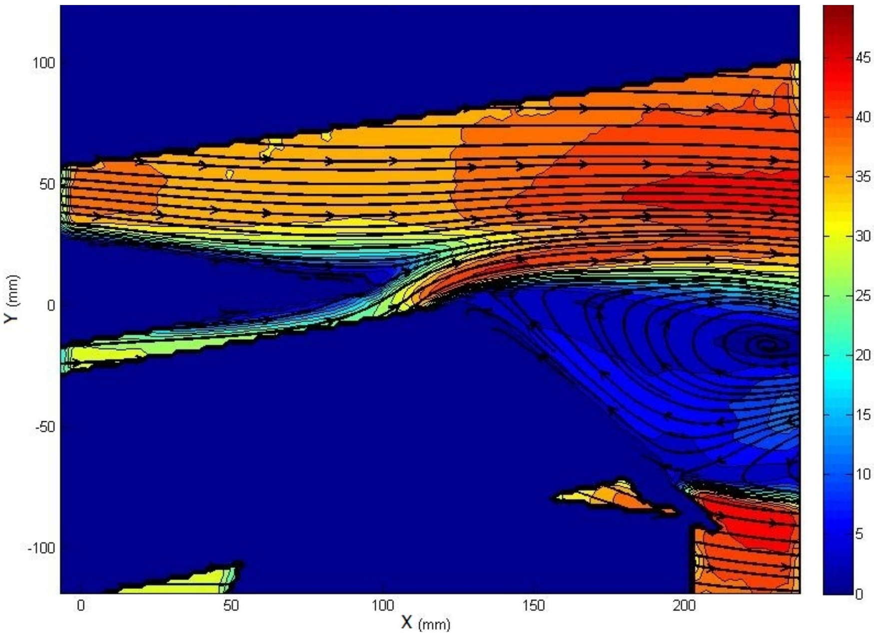

Figure B.7: Velocity contours and streamlines of configuration G0-O4 at $\alpha = 0^\circ$

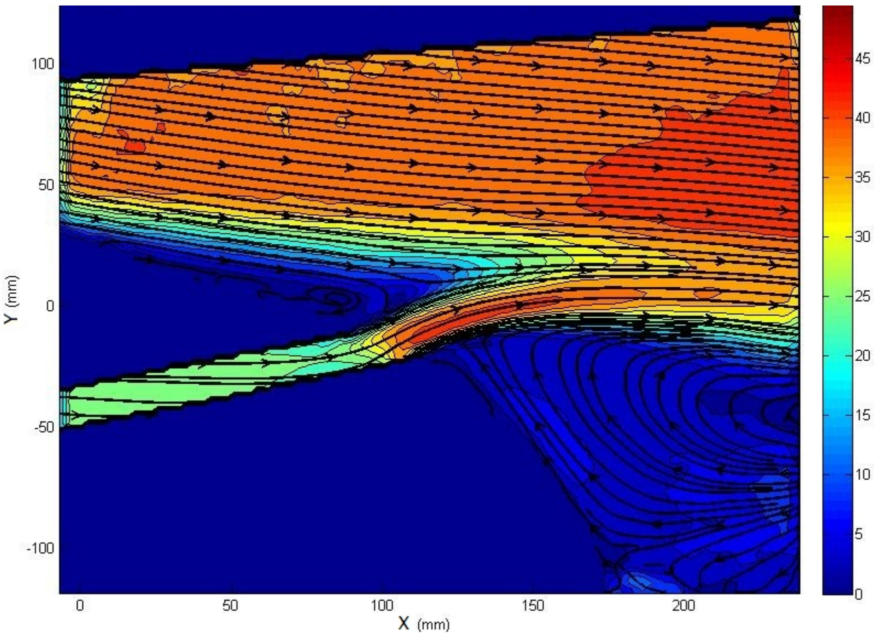

Figure B.8: Velocity contours and streamlines of configuration G0-O4 at $\alpha = 10^{\circ}$

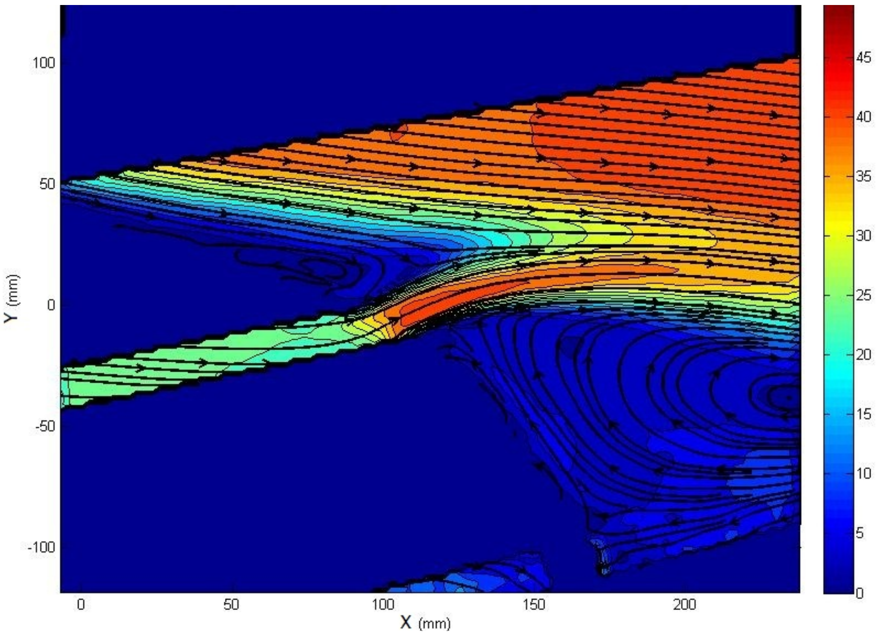

Figure B.9: Velocity contours and streamlines of configuration G0-O4 at $\alpha = 12^{\circ}$

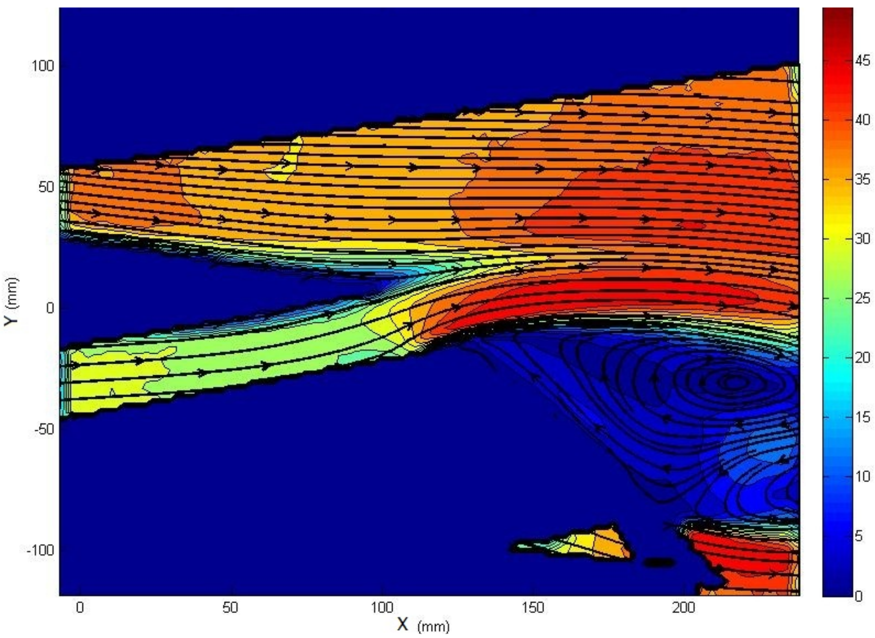

Figure B.10: Velocity contours and streamlines of configuration G4-O4 at $\alpha = 0^\circ$

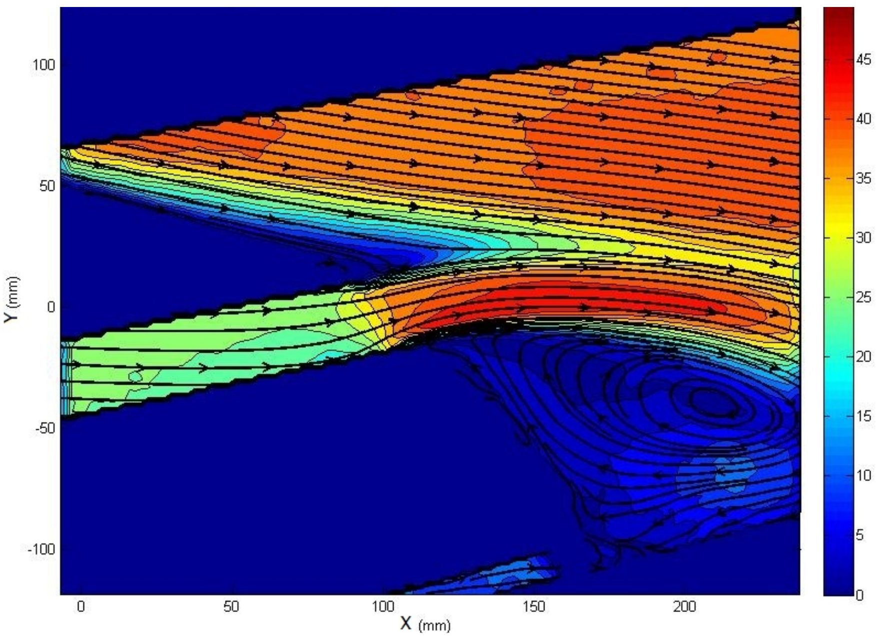

Figure B.11: Velocity contours and streamlines of configuration G4-O4 at $\alpha = 10^\circ$

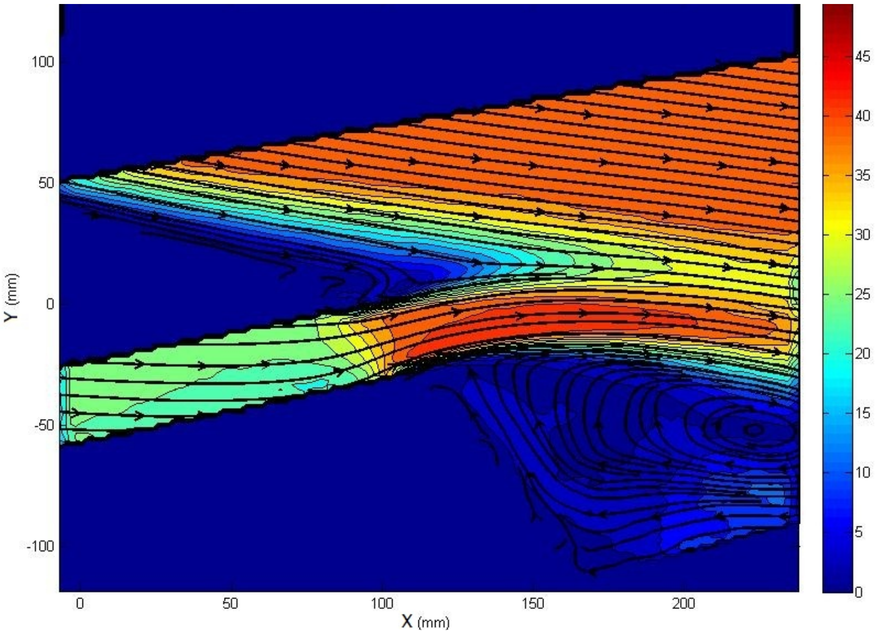

Figure B.12: Velocity contours and streamlines of configuration G4-O4 at $\alpha = 12^\circ$

Appendix C

Landing configuration vorticity contours and streamlines

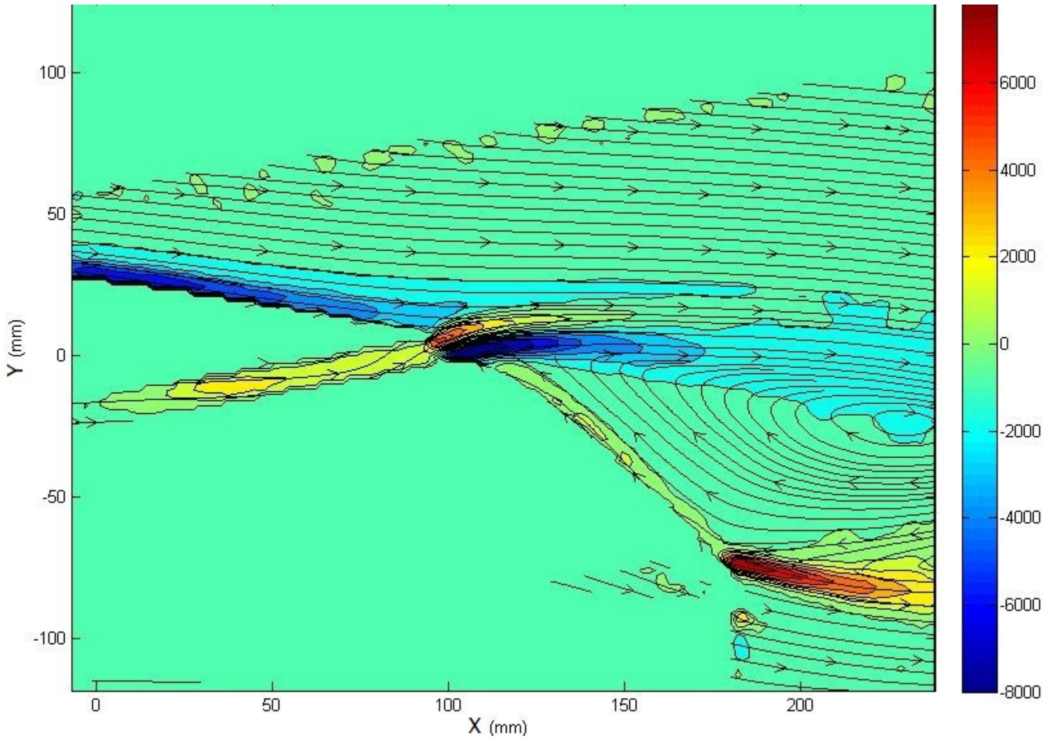

Figure C.1: Mean spanwise vorticity contours and streamlines of configuration G0-O0 at $\alpha = 0^\circ$

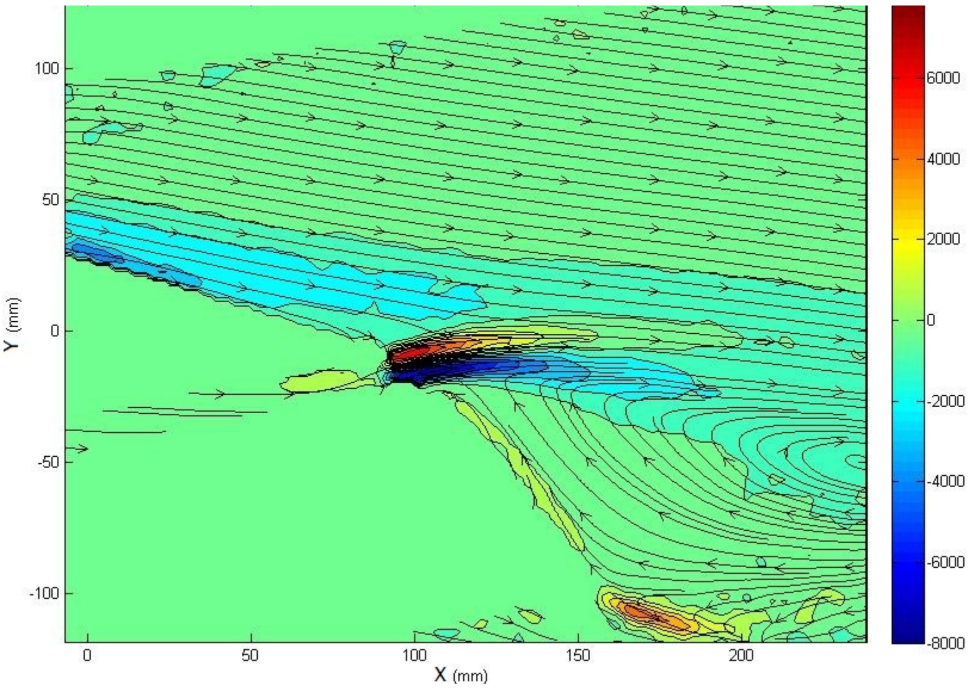

Figure C.2: Mean spanwise vorticity contours and streamlines of configuration G0-O0 at $\alpha = 10^{\circ}$

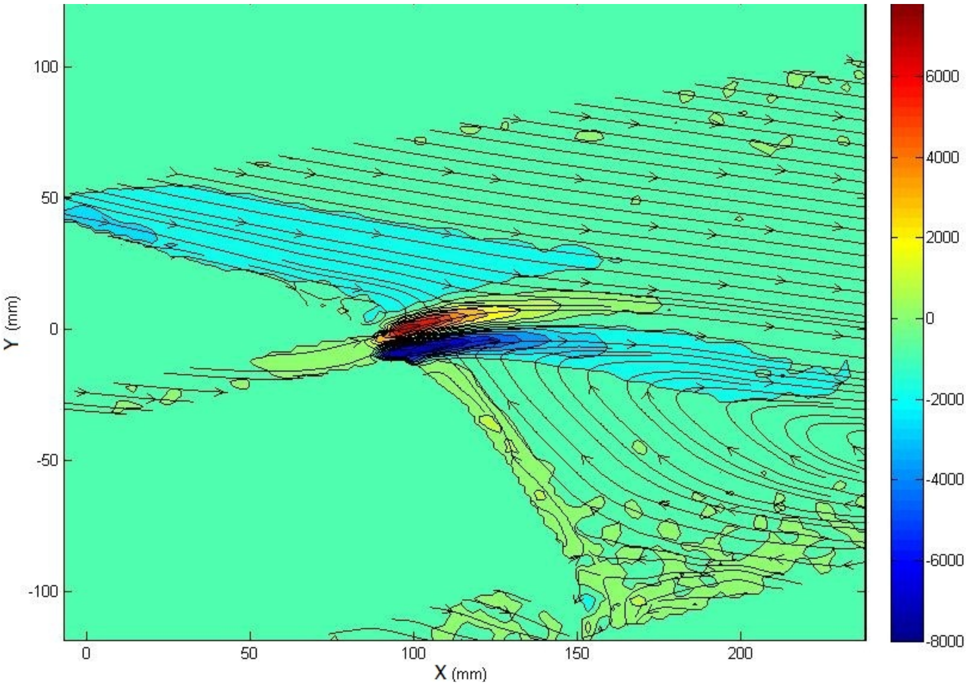

Figure C.3: Mean spanwise vorticity contours and streamlines of configuration G0-O0 at $\alpha = 12^{\circ}$

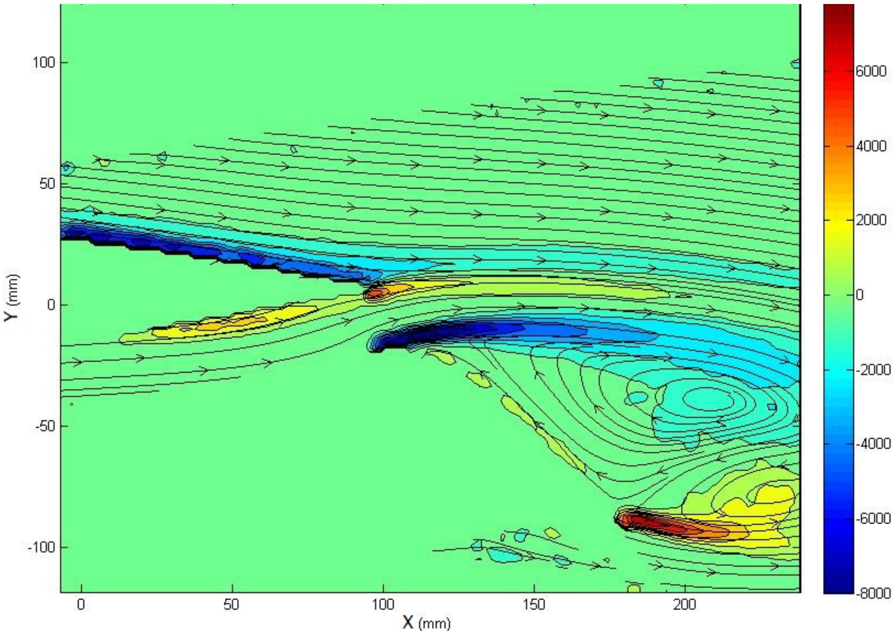

Figure C.4: Mean spanwise vorticity contours and streamlines of configuration G4-O0 at $\alpha = 0^{\circ}$

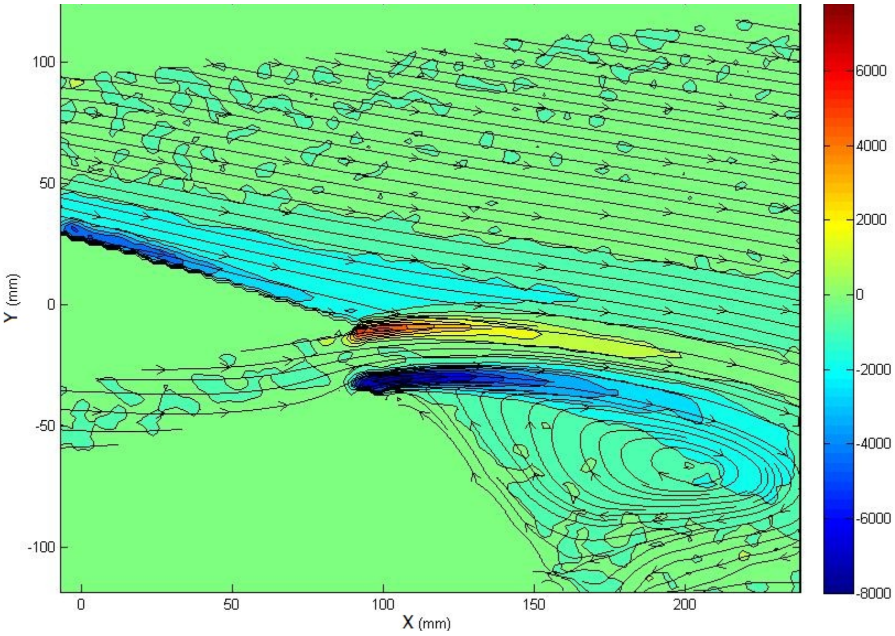

Figure C.5: Mean spanwise vorticity contours and streamlines of configuration G4-O0 at $\alpha = 10^{\circ}$

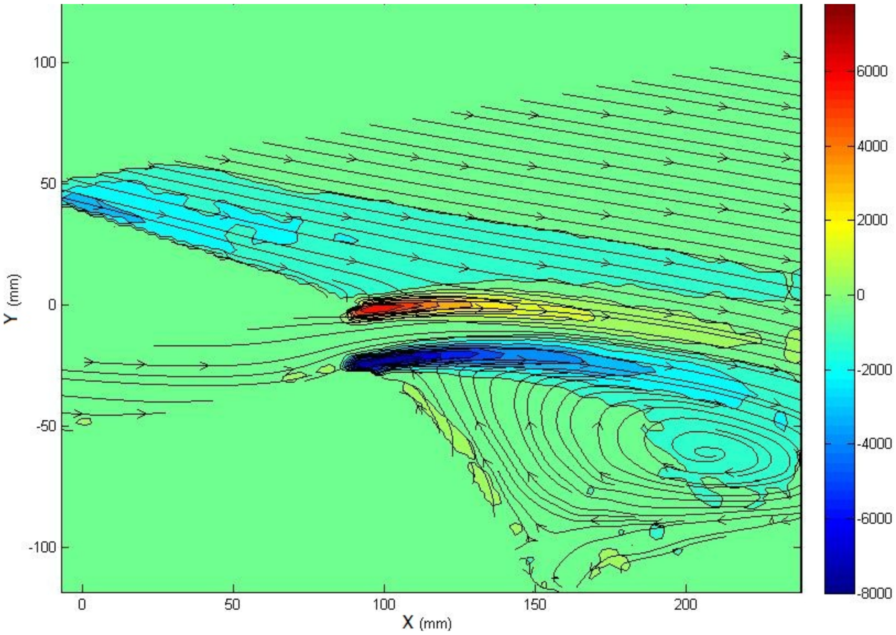

Figure C.6: Mean spanwise vorticity contours and streamlines of configuration G4-O0 at $\alpha = 12^\circ$

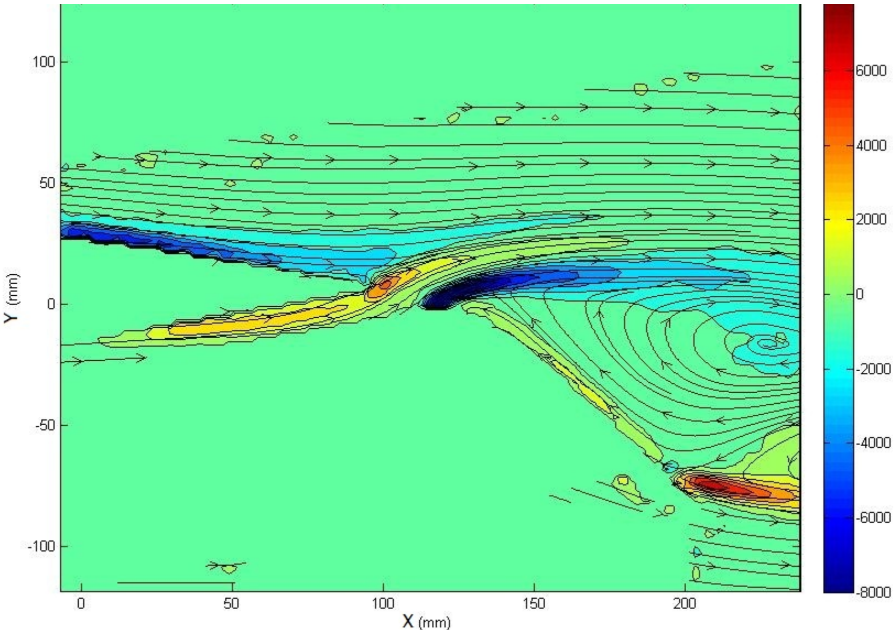

Figure C.7: Mean spanwise vorticity contours and streamlines of configuration G0-O4 at $\alpha = 0^\circ$

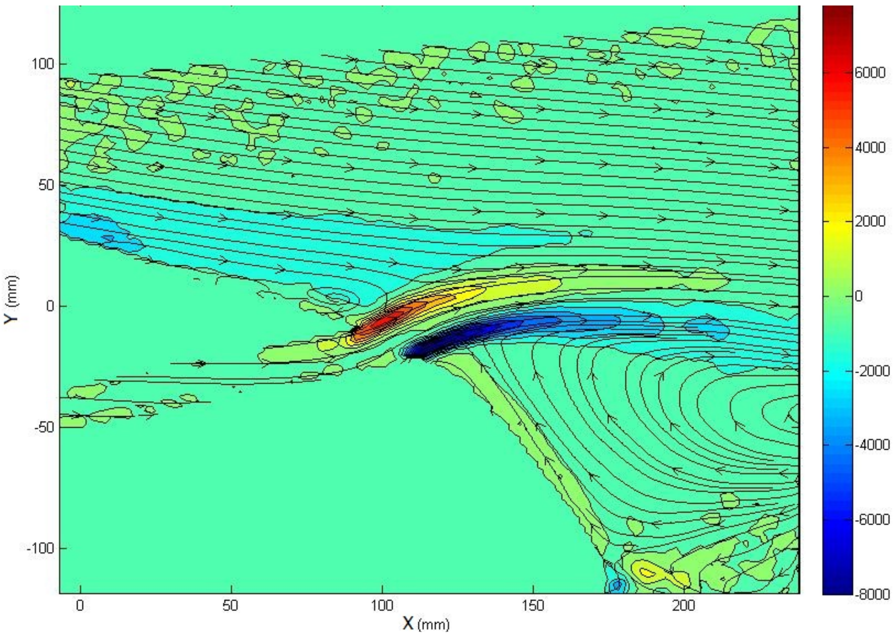

Figure C.8: Mean spanwise vorticity contours and streamlines of configuration G0-O4 at $\alpha = 10^\circ$

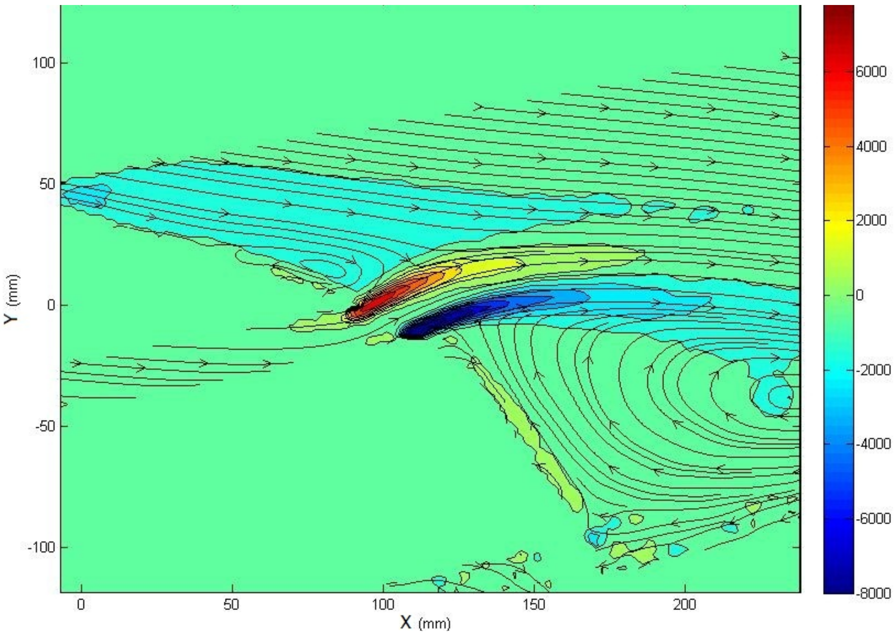

Figure C.9: Mean spanwise vorticity contours and streamlines of configuration G0-O4 at $\alpha = 12^\circ$

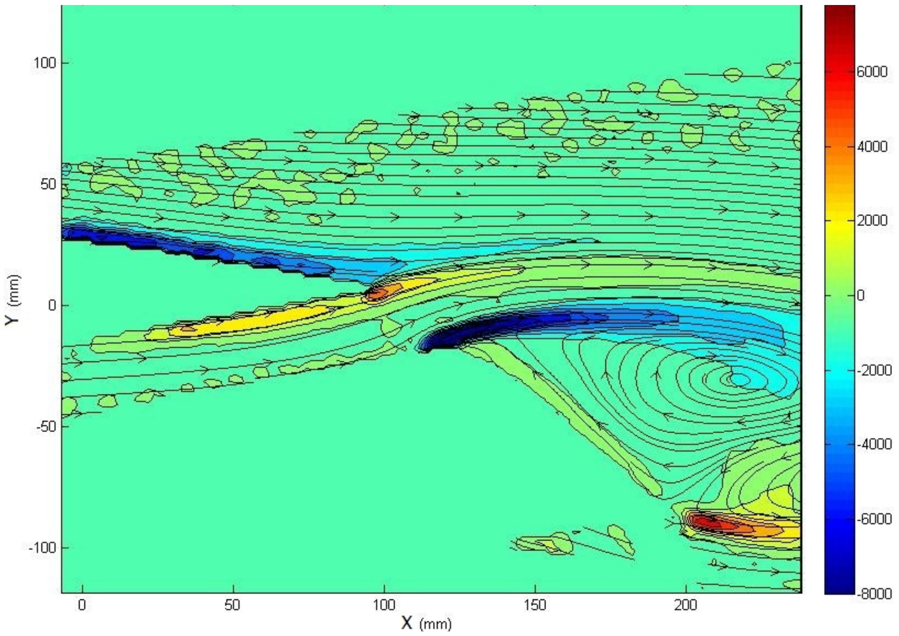

Figure C.10: Mean spanwise vorticity contours and streamlines of configuration G4-O4 at $\alpha = 0°$

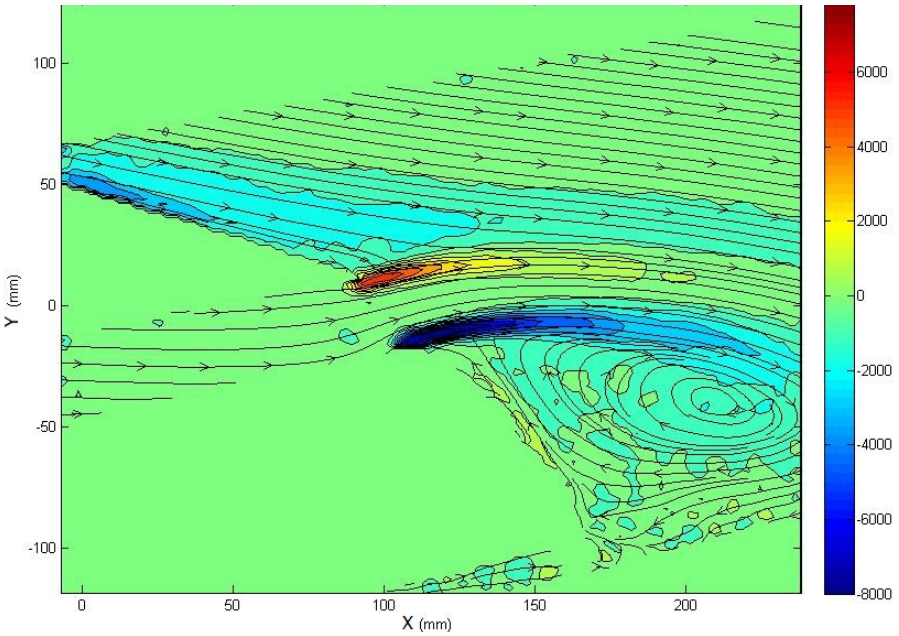

Figure C.11: Mean spanwise vorticity contours and streamlines of configuration G4-O4 at $\alpha = 10°$

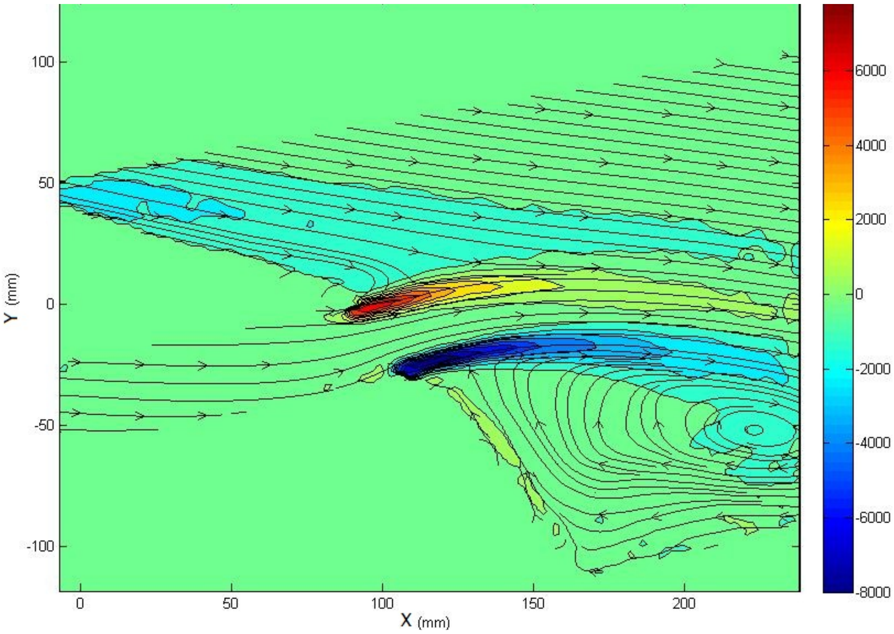

Figure C.12: Mean spanwise vorticity contours and streamlines of configuration G4-O4 at $\alpha = 12^\circ$